Novel Methods and Applications of NMR and MRI: Low-Power RF Excitation and Hyperpolarized Xenon-129

Von der Fakultät für Mathematik, Informatik und Naturwissenschaften der RWTH Aachen University zur Erlangung des akademischen Grades einer Doktorin der Naturwissenschaften genehmigte Dissertation vorgelegt von

Dipl.-Phys.

Nadia Amor

aus Geldern

Berichter: Universitätsprofessor Dr. Dr. h.c. Bernhard Blümich
Universitätsprofessor Dr. Thomas Schmitz-Rode

Tag der mündlichen Prüfung: 13. Februar 2012

Berichte aus der Physik

Nadia Amor

Novel Methods and Applications of NMR and MRI: Low-Power RF Excitation and Hyperpolarized Xenon-129

Shaker Verlag
Aachen 2012

Bibliographic information published by the Deutsche Nationalbibliothek
The Deutsche Nationalbibliothek lists this publication in the Deutsche Nationalbibliografie; detailed bibliographic data are available in the Internet at http://dnb.d-nb.de.

Zugl.: D 82 (Diss. RWTH Aachen University, 2012)

Printed in Germany.

ISBN 978-3-8440-0897-5
ISSN 0945-0963

Shaker Verlag GmbH • P.O. BOX 101818 • D-52018 Aachen
Phone: 0049/2407/9596-0 • Telefax: 0049/2407/9596-9
Internet: www.shaker.de • e-mail: info@shaker.de

Abstract

Since their discovery in the middle of the last century, Nuclear Magnetic Resonance (NMR) and Magnetic Resonance Imaging (MRI) have become an important and very versatile tool in industry, medicine, and basic research. The aim of this work is to explore possible improvements and new applications of NMR methods. First, a recently introduced excitation NMR pulse sequence, termed *Frank sequence excitation*, which allows for significant reduction of rf-excitation power, is systematically analyzed and compared to conventional NMR in detail. Furthermore, its feasibility for MRI is investigated and advantages as well as drawbacks in comparison to standard MRI are discussed. The second part focuses on new biomedical applications of *hyperpolarized (HP)* ^{129}Xe which not only offers a signal enhancement of several orders of magnitude but also provides new contrast mechanisms. A setup for continuous dissolution of HP ^{129}Xe gas into blood and other fluids is optimized and analyzed quantitatively by NMR and MRI. On the basis of these results, blood-dissolved HP ^{129}Xe is used to investigate blood-gas dynamics, as well as the rheological behavior of blood.

Contents

Abbreviations, Symbols, and Constants **ix**

Introduction **1**

I. Fundamentals **5**

1. Nuclear Magnetic Resonance (NMR) **9**
1.1. Spin Interactions 9
1.1.1. External Interactions 10
1.1.2. Internal Interactions 13
1.2. Classical Model: Polarization and Relaxation 15
1.3. NMR Signal and FT NMR 18
1.3.1. Sensitivity and Signal Enhancement 21
1.3.2. Spin Echo 22
1.3.3. 2D NMR Spectroscopy 23

2. Magnetic Resonance Imaging (MRI) **27**
2.1. Introduction to k-Space Formalism 27
2.2. Frequency and Phase Encoding 28
2.3. Slice Selection 32
2.4. Imaging Sequences 33

3. NMR Spectrometer **37**

II. Frank-Sequence Excitation **41**

4. Introduction to Frank-Sequence NMR **43**

5. Theory of Low-Power NMR and MRI **47**
5.1. Frank Sequences 47
5.2. SPREAD Slice Selection 49

6. Experimentals **51**
6.1. Simulations 51
6.2. Experimental Setup 51
6.3. NMR Methods 52

7. Analysis of Frank-Sequence NMR **55**
7.1. Frequency Sweep Character 55
7.2. Steady State Condition 60
7.3. Excitation Profile 62
7.3.1. Finite Pulse Length Effects 62
7.3.2. Linear Excitation Limit 64
7.4. Sensitivity 67
7.5. System Response for N$\rightarrow \infty$ and $N \rightarrow 1$ Pulses 70

8. MRI with Frank Sequences **73**
8.1. 2D MRI 73
8.2. Slice Selection 76
8.3. Slice-Selective 2D MRI 76

9. Conclusions and Outlook **79**

III. Hyperpolarized ^{129}Xe **81**

10. Introduction to HP ^{129}Xe NMR and MRI **83**

11. Theoretical Background **87**
11.1. Hyperpolarized Gases 87
11.1.1. Optical Pumping 88
11.1.2. Spin Exchange 91
11.1.3. Relaxation Mechanisms 93
11.2. ^{129}Xe Properties 95
11.2.1. General Properties of Xenon 95
11.2.2. Solubility of Xenon 97

11.2.3. Chemical Shift of ^{129}Xe 97
11.3. Blood Fundamentals 99
11.3.1. Fundamentals of Blood-Gas Exchange 99
11.3.2. Blood Rheology 106

12. Experimentals **111**
12.1. Experimental Setup 111
12.1.1. The Hyperpolarizer 111
12.1.2. The Xenonizer 115
12.1.3. Setups for Blood Flow Investigations 119
12.1.4. Blood Preparation and Analysis 124
12.2. NMR Methods 126

13. Analysis of the Xenonizer Setup **127**
13.1. Optimization of the Dissolution Process 129
13.2. MRI of the Xenonizer Setup 130
13.3. Dissolution Efficiencies of Different Fibers 133
13.4. Effects on Blood Parameters 135

14. Biomedical Applications **139**
14.1. Blood-Gas Exchange Dynamics 139
14.1.1. Online Monitoring of Blood Deoxygenation 139
14.1.2. Xenon Gas Exchange Dynamics in the Xenonizer 148
14.2. Analysis of Blood Flow Behavior 150
14.2.1. Capillary Blood Flow 151
14.2.2. Blood Flow in the Couette System 156

15. Conclusions and Outlook **161**

Conclusions **165**
Frank-Sequence Excitation 167
Hyperpolarized ^{129}Xe NMR and MRI 168

Appendices **171**

A. Frank-Sequence NMR **173**

B. Hyperpolarized Xenon-129 NMR **177**
B.1. Temperature Dependence 177
B.2. Effect of Gradient Switching on Hyperpolarization 178
B.3. Analysis of RBC Peak Shape 179
B.4. EXSY Spectra for Various Mixing Times 179

Bibliography **185**

Abbreviations, Symbols, and Constants

Abbreviations

a.u.	arbitrary units
ADC	Analog-to-Digital Converter
CW	Continuous Wave
CSA	Chemical Shift Anisotropy
CSI	Chemical Shift Imaging
EXSY	EXchange SpectroscopY
FBP	Filtered BackProjection
FFT	Fast Fourier Transformation
FID	Free Induction Decay
FLASH	Fast Low Angle SHot (pulse sequence)
fMRI	functional Magnetic Resonance Imaging
FOF	Field Of Flow
FOV	Field Of View
FT	Fourier Transform(-ation)
FWHM	Full Width at Half Maximum
GE	Gradient Echo
Hb	Hemoglobin
Hct	Hematocrit
HP	HyperPolarized
HP	Hard Pulse (as opposed to Frank sequence)
ID	Inner Diameter
IFT	Inverse Fourier Transform(-ation)

MCH	Mean Corpuscular Hemoglobin
MCV	Mean Corpuscular Volume
MRI	Magnetic Resonance Imaging
NMR	Nuclear Magnetic Resonance
OD	Outer Diameter
O_2Hb	Oxygenated Hemoglobin
OP	Optical Pumping
PEEK	PolyEtherEtherKetone
PDMS	PolyDiMethylSiloxane
PMMA	PolyMethylMethAcrylate
PMP	PolyMethylPentene
ppm	parts per million
PP	PolyPropylene
PSF	Point Spread Function
Px	Pixel
RBC	Red Blood Cell
RHb	deoxygenated Hemoglobin (*Reduced* Hemoglobin)
rf	radio frequency
sd	spin destruction
SE	Spin Echo
SEM	Scanning Electron Microscopy
SEOP	Spin-Exchange Optical Pumping
SNR	Signal-to-Noise Ratio
SPREAD	Selective Pulses with REduced Amplitude Distribution
sr	spin rotation
sx	spin exchange
SWIFT	Sweep Imaging With Fourier Transformation
TPPI	Time-Proportional Phase Incrementation
vdW	van der Waals
w/v	weight-to-volume ratio

Important Symbols

α	flip angle
γ	gyromagnetic ratio
$\dot{\gamma}$	shear rate
δ	chemical shift
Δt_{p}	rf pulse length
$\Delta\omega$	spectral line width (typically full width at half maximum)
η	dynamic viscosity
λ	coherence decay rate constant
μ	nuclear magnetic moment
ν_{Ny}	Nyquist frequency
ν_{s}	sampling frequency
$\rho_{(\mathrm{eff})}$	(effective) spin density
σ / $\hat{\sigma}$	chemical shift constant/tensor
τ_{mix}	mixing time
ϕ_i	phase of pulse i
$\lvert\Psi(t)\rangle$	wave function
ω_0	Larmor frequency
Ω_0	$= \omega - \omega_0$, offset frequency, i.e., difference between Larmor frequency and reference frequency
ω_{ref}	reference frequency
A_{m}	active hollow-fiber membrane area
B_0	main magnetic field strength
B_1	strength of rf field
B_{eff}	effective magnetic field strength
c_i^j	concentration of compound i in medium j
$D^{(\mathrm{eff})}$	(effective) diffusion coefficient
DW	dwell time
E	energy
f_{w}	counter for steps on the frequency grid of Frank sequence
G	gradient strength
$G_{\mathrm{read/ph/slice}}$	read/phase/slice gradient

$G_{x/y/z}$	gradient in x-/y-/z-direction
$\mathcal{H}$	Hamiltonian (with subscripts $\mathrm{Z, rf, DD, cs}, J, \mathrm{Q}$ for Zeeman, radio frequency, dipole-dipole coupling, chemical shift, J-coupling, and quadrupolar coupling, respectively)
I	spin quantum number
k	chemical exchange rate
k_B	Boltzmann constant
k_{O_2}	(diffusive) oxygen mass transport coefficient
$\vec{k}$	reciprocal space vector
L_i^j	Ostwald solubility of gas i in medium j
m	number of rf pulses within one Frank excitation package, and number of Frank packages per sequence
m_I	magnetic spin quantum number
$M_{(0)}$	(initial) magnetization
M_n	n-th spectral moment
n	Hill parameter, oxygen affinity of hemoglobin
N	Noise
N	number of rf pulses in Frank sequence
$N_\pm$	population number in Zeeman state $m_I = \pm 1/2$
NS	Number of Scans
p	$:= \frac{\Delta t_\mathrm{p}}{\Delta t}$, ratio of Frank pulse length and pulse spacing
P	polarization
pO_2	partial pressure of oxygen
Re	Reynolds number
S	NMR signal
$S(\omega)$	frequency spectrum
$S_\mathrm{i}(\omega)$	spectral density function
sO_2	oxygen saturation level
$[t]$	time unit of pulse spacing Δt and length Δt_p in Frank excitation
T	temperature
T_1 / T_2	longitudinal / transverse relaxation time
t_w	counter for steps on the time grid of Frank sequence
TE	Echo Time

TR	Repetition Time
v	velocity
V_i	volume of compound i
$x(t)\,/\,X(f)$	Frank excitation function in time/frequency domain

Constants[1]

amagat	particle density of a real gas at standard conditions ($p_0 = 1013\,\mathrm{mbar}$ and $T = 273\,\mathrm{K}$) corresponds to $2.69 \cdot 10^{-19}\,\mathrm{cm}^{-3}$
e	elementary charge, $1.602176487(40) \cdot 10^{-19}\,\mathrm{C}$
$\gamma(^1H)$	gyromagnetic ratio of ^{1}H, $26.7519 \cdot 10^7\,\mathrm{rad\,s^{-1}\,T^{-1}}$
$\gamma(^{129}Xe)$	gyromagnetic ratio of ^{129}Xe, $-7.452103 \cdot 10^7\,\mathrm{rad\,s^{-1}\,T^{-1}}$
h	Planck quantum, $6.62606896(33) \cdot 10^{-34}\,\mathrm{J\,s}$
$\hbar$	$=\mathrm{h}/2\pi$, reduced Planck quantum, $1.054571628(53) \cdot 10^{-34}\,\mathrm{J\,s}$
k_B	Boltzmann constant, $1.3806504(24) \cdot 10^{-23}\,\mathrm{J\,K^{-1}}$
m_e	rest mass of electrons, $9.10938 \cdot 10^{-31}\,\mathrm{kg}$
m_p	rest mass of protons, $1.673 \cdot 10^{-27}\,\mathrm{kg} = 1836 \cdot m_\mathrm{e}$
μ_K	nuclear magneton, $5.05078324(13) \cdot 10^{-27}\,\mathrm{J\,T^{-1}}$
μ_0	magnetic field constant, $4\pi \cdot 10^{-7}\,\mathrm{V\,s\,A^{-1}\,m^{-1}} = 12.566370614 \cdot 10^{-7}\,\mathrm{N\,A^{-2}}$
N_A	Avogadro number, $6.02214179(30) \cdot 10^{23}\,\mathrm{mol^{-1}}$

[1] Constants are obtained from [NIST 07].

R	gas constant, $8.314472(15)\,\mathrm{J\,mol^{-1}\,K^{-1}}$

Introduction

The exploration of the physical phenomenon of *Nuclear Magnetic Resonance (NMR)* started in 1933 with the discovery of the nuclear spin by Otto Stern and first experiments by Isidor I. Rabi, who received the Nobel Prize in 1943 and 1944, respectively [Frisch 33; Breit 31]. The principle of NMR is based on radio-frequent excitation of nuclear magnetic moments that precess in an outer magnetic field with a characteristic resonance frequency. Already in 1945, Felix Bloch and Edward Purcell detected the first NMR signals and were awarded the Nobel Prize in physics in 1952 [Bloch 46a; Purcell 46]. These findings led to a rapid progress in NMR spectroscopy: in 1951, James T. Arnold and Fu C. Yu showed that the nuclear resonance frequency is characteristic of its chemical surrounding and thereby discovered the chemical shift [Arnold 51; Proctor 50]. Another great step was made by Richard Ernst in 1966, who introduced Fourier-NMR and was also awarded a Nobel Prize in 1991. Today, manifold applications are known in chemical structure and dynamics analysis, in material science, geophysics, and in portable NMR. In 2002, Kurt Wüthrich received a Nobel Prize for his contribution in protein NMR [Wüthrich 03].

The most prevalent and best-known field nowadays is *Magnetic Resonance Imaging (MRI)*. The basic idea was presented in the 1970s by Paul C. Lauterbur und Sir Peter Mansfield and was later acknowledged with the Nobel Prize in medicine in 2003 [Lauterbur 73; Mansfield 73]: a spatially varying magnetic field enables space encoding of the magnetic field strength dependent nuclear resonance frequencies. Approximately ten years later, in 1983, the first commercial clinical tomograph was available. Since then, a great variety of techniques has been developed to examine different body tissues with appropriate contrast mechanisms. Especially functional MRI (fMRI) has turned out to be an outstanding tool in modern brain research.

Since the beginning of MRI, the strength of the main magnetic field has steadily increased by several orders of magnitude, from a few millitesla in permanent magnets to over 9 T in modern super-conducting tomographs, because of the inherently higher signal-to-noise ratio [Krug 09; Marques 10]. Along with it, advances have been made regarding homogeneity and temporal stability of the fields. While 1.5 T to 3 T tomographs are clinical standard since the 1990s, the use of ultra high fields of 7 T up to 11 T is restricted mainly to research applications. However, the rf power and energy absorbed in the body tissue, quantified by the SAR (specific absorption rate), scales with the square of the main magnetic field. Therefore, conventional rf-pulse excitation perpetually exceeds legal SAR limitations [DIN 08]. This problem could be solved by novel rf-excitation pulse sequences, one of which is investigated in the present work [Idiyatullin 06; Blümich 09].

Another drawback of classical ^{1}H NMR and MRI is the low sensitivity: the signal measured is proportional to the population difference, the *polarization*, of two so-called Zeeman-levels into which the energy levels split in an outer magnetic field. Even in fields of several tesla and at low temperatures, the Boltzmann distribution only yields polarizations of the order of 10^{-6}. As a result, different *hyperpolarization* techniques have been developed. In this work, hyperpolarized (HP) ^{129}Xe is employed as a new means of NMR and MRI contrast. With optical methods, the polarization and consequently the NMR signal of this noble gas can be enhanced by up to five orders of magnitude [Kastler 50; Bouchiat 60; Happer 84; Appelt 98]. Since its discovery, HP ^{129}Xe has been employed in many different fields of research. While first mainly the HP ^{129}Xe gas has been used, its solubility has widened the range of possible applications even further [Goodson 02; Oros 04]. Especially in bio-medicine, HP ^{129}Xe has been proven a versatile sensor tool for molecular spectroscopy and imaging [Cherubini 03].

Thus, the aims of this thesis can be summarized as:

1. Investigation of a novel excitation scheme to reduce rf power and its implementation for MRI (Part II),

2. Application of gaseous and dissolved hyperpolarized ^{129}Xe for analysis of biomedical systems (Part III).

For easier understanding, the first part covers fundamental aspects of NMR and MRI and the basic setup used throughout this work. More detailed introductions to low-power NMR and HP ^{129}Xe, as well as the specific experimental materials and methods can be found in the respective parts along with the achieved results, their discussion, and individual conclusions and outlooks.

Part I.

Fundamentals

In this part, fundamental theory of nuclear magnetic resonance (NMR) spectroscopy and imaging (MRI) is explained in Chapters 1 and 2, respectively, to provide a scientific background for the work presented. In Chapter 3, the basic setup of a high-field NMR spectrometer is explained. The presentation of content and format in the following three chapters follows standard NMR literature [Levitt 05; Callaghan 93; Abragam 61; Blümich 92]. Further details on specific subjects can be found in the according literature.

Chapter 1.

Nuclear Magnetic Resonance (NMR)

Nuclear magnetic resonance (NMR) is based on the physical degree of freedom of the nucleus, the *nuclear spin*, which quantum-mechanically describes the intrinsic angular momentum of elementary particles. Like the macroscopic angular momentum, the spin is described by a vector $\vec{I} = (I_x, I_y, I_z)$. The nuclear spin is observable through the alignment of the resulting *nuclear magnetic moment* in an external magnetic field $\vec{B}_0$ and is characterized by the largest observable component of the angular momentum $I \cdot \hbar$, the so-called *spin quantum number* I. Depending on the type of particle, I is of integer or half-integer value leading to the classification of particles as bosons and fermions, respectively.

1.1. Spin Interactions

The time evolution of a spin state $|\Psi(t)\rangle$ under the effect of a Hamiltonian $\mathcal{H}$ is described quantum-mechanically by the time-dependent Schrödinger equation,

$$\frac{d}{dt}|\Psi(t)\rangle = -i\hbar\,\mathcal{H}(t)|\Psi(t)\rangle, \tag{1.1}$$

wherein $\hbar$ is *Planck's constant* devided by 2π. The interactions of a nucleus in a static magnetic field can be expressed by the spin Hamiltonian:

$$\mathcal{H} = \mathcal{H}_\mathrm{Z} + \mathcal{H}_\mathrm{rf} + \mathcal{H}_\mathrm{DD} + \mathcal{H}_\mathrm{cs} + \mathcal{H}_J + \mathcal{H}_\mathrm{Q}. \tag{1.2}$$

While the Zeeman interaction $\mathcal{H}_\mathrm{Z}$ and the radio-frequency (rf) interaction $\mathcal{H}_\mathrm{rf}$ are externally induced, the internal interactions can be divided into the direct dipolar coupling $\mathcal{H}_\mathrm{DD}$, the chemical shift interaction $\mathcal{H}_\mathrm{cs}$, the indirect spin-spin coupling, also known as J-coupling $\mathcal{H}_J$, and the quadruploar coupling $\mathcal{H}_\mathrm{Q}$. Schematically, these terms and their

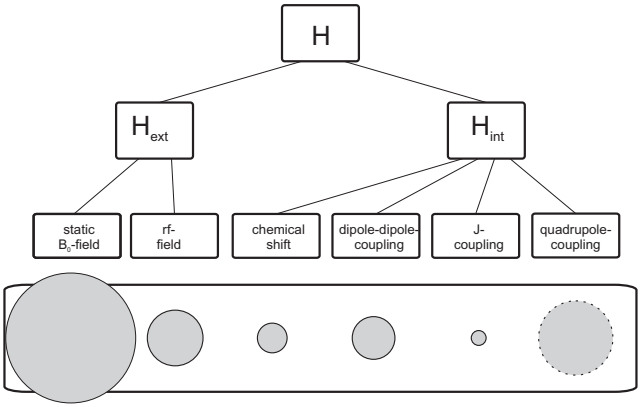

Figure 1.1.: Graphical illustration of the spin Hamiltonian [Levitt 05]. The size of the circles schematically corresponds to the typical significance of the according term in high magnetic fields. Quadrupolar coupling vanishes for spins 1/2.

relative relevance is depicted in Fig. 1.1. A classical interpretation of these individual terms is provided in the following.

1.1.1. External Interactions

With every nuclear spin $\vec{I}$, a so-called *nuclear magnetic dipole moment* can be associated,

$$\vec{\mu} = \gamma\hbar \cdot \vec{I}, \tag{1.3}$$

where the proportionality factor γ is known as the *gyromagnetic ratio*. It is usually expressed in units of the *nuclear magneton*,

$$\vec{\mu}_{\mathrm{K}} = \frac{e}{2m_{\mathrm{p}}}\hbar, \tag{1.4}$$

with the rest mass m_{p} of the proton and the elementary charge e. The magnetic dipole moment $\vec{\mu}$ interacts with an external magnetic field $\vec{B}_0$. The magnetic energy of the nucleus is given by

$$E_{\mathrm{mag}} = -\vec{\mu} \cdot \vec{B}_0, \tag{1.5}$$

which depends on the relative orientation of $\vec{\mu}$ and $\vec{B}_0$ and vanishes, when both vectors are perpendicular. For macroscopic objects, Eq. (1.5) can be generalized:

$$E_{\text{mag}} = -\int d^3x\, \vec{\mu} \cdot \vec{B}_0. \tag{1.6}$$

If the magnetic moment points into the same direction as the spin, a positive gyromagnetic ratio results, $\gamma > 0$. For anti-parallel vectors $\gamma < 0$ is obtained.

The *nuclear magnetic spin quantum number* $m_I = (-I, ..., I-1, I)$ reflects the $(2I+1)$ quantum-mechanically allowed orientations of the nuclear spin in the magnetic field $\vec{B}_0$. These different states in the presence of the $\vec{B}_0$ field lead to an energy splitting of the otherwise degenerated ground state into the so-called *nuclear Zeeman levels*. For those isotopes relevant in this work, ^{1}H and ^{129}Xe with $I = 1/2$ and $m_I = \pm 1/2$ two energy levels $E_\pm$ separated by an energy difference ΔE are observed. Without loss of generality, the direction of the outer magnetic field can be chosen along the z-axis. As depicted in Fig. 1.2, the following relation applies:

$$\langle \mathcal{H}_Z \rangle = \Delta E = |E_+ - E_-| = -\vec{\mu} \cdot \vec{B}_0 = |\gamma|\, \hbar\, B_0. \tag{1.7}$$

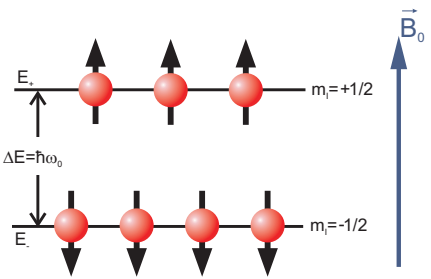

Figure 1.2.: Population of the two energy levels with applied B_0 field.

For a macroscopic sample in equilibrium and in absence of a magnetic field, the distribution of magnetic moments is completely isotropic. In the presence of a magnetic field, the magnetic moments *precess* around the field under a constant angle (Fig. 1.3). The precession frequency is referred to as the *Larmor frequency* and results from Bohr's correspondence principle $E = \hbar\omega$. Thus, it only depends on the magnetic field strength B_0 and the gyromagnetic ratio γ:

$$\omega_0 = \gamma B_0. \tag{1.8}$$

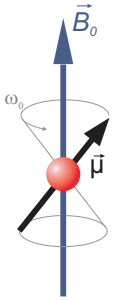

Figure 1.3.: Classical picture of the precession of the magnetic moment around the axis of the magnetic field.

An additional radio-frequency (rf) field $\vec{B}_{\mathrm{rf}}$ is generated along the x-axis, the amplitude of which oscillates at the spectrometer frequency ω,

$$\vec{B}_{\mathrm{rf}}(t) = B_{\mathrm{rf}} \cos(\omega t)\hat{e}_x, \tag{1.9}$$

where the maximum amplitude is denoted as B_{rf}. For further considerations, the oscillation is described by a sum of two rotating components:

$$\vec{B}_{\mathrm{rf}}(t) = \vec{B}_{\mathrm{rf}}^{\mathrm{res}}(t) + \vec{B}_{\mathrm{rf}}^{\mathrm{n.res}}(t). \tag{1.10}$$

The component of the rf field that rotates with the spins is called *resonant*, the counter-rotating *non-resonant*, accordingly:

$$\vec{B}_{\mathrm{rf}}^{\mathrm{res}}(t) = \frac{1}{2} B_{\mathrm{rf}}[\cos(\omega t)\hat{e}_x + \sin(\omega t)\hat{e}_y] \tag{1.11}$$

$$\vec{B}_{\mathrm{rf}}^{\mathrm{n.res}}(t) = \frac{1}{2} B_{\mathrm{rf}}[\cos(\omega t)\hat{e}_x - \sin(\omega t)\hat{e}_y]. \tag{1.12}$$

The non-resonant component has negligible effect on the spins and therefore usually is omitted. Only in rare cases, a small Bloch-Siegert shift of the resonance frequency is observed. Since hereby one half of the rf power is lost, a factor of $1/2$ is introduced, which oftentimes is avoided by setting $B_1 := 2B_{\mathrm{rf}}$. The rf fraction of the spin Hamiltonian thus can be re-written as

$$\mathcal{H}_{\mathrm{rf}} \approx -\gamma\, \hbar\, B_1[\cos(\omega t)I_x + \sin(\omega t)I_y]. \tag{1.13}$$

1.1.2. Internal Interactions

Apart from the above discussed externally induced electro-magnetic effects, also the electrons and nuclei of a sample object have to be considered as sources of local magnetic fields. Since the spin interactions are dominated by the interaction with the external magnetic field $\vec{B}_0$, simplifications of the internal Hamiltonians within the limits of the *secular approximation* are possible. Furthermore, in gases and in fluids as investigated in this work, molecular motion and fluctuations of the internal interactions are fast on the time scale of the Larmor frequency. Therefore, *motional averaging* of these terms leads to further simplification.

The $\vec{B}_0$-field induces currents in the electron clouds of atoms and molecules, which in turn induce local magnetic fields. Thus, two different nuclei even within the same molecule will be influenced by magnetic fields that differ according to their electronic environment. These fields are the sum of externally applied and locally induced fields and result with Eq. (1.8) in a change of the spin resonance frequency (Fig. 1.4). This effect is termed

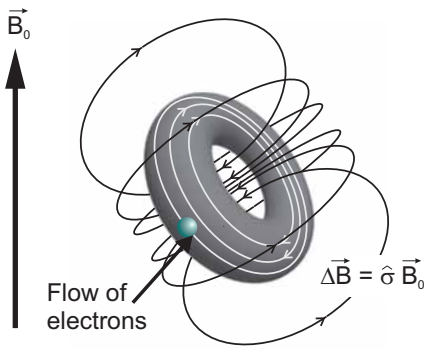

Figure 1.4.: Mechanism of chemical shift [Levitt 05].

chemical shift and forms an essential basis for NMR spectroscopy. Even though typically the induced field is only 10^{-4} times as strong as the external field B_0 [Levitt 05], it is still large enough to cause a measurable shift of the spin precession frequency. The induced field is directly proportional to the applied field $\vec{B}_0$:

$$\vec{B} = \vec{B}_0(1 - \hat{\sigma}), \tag{1.14}$$

where $\hat{\sigma}$ is the *chemical shielding tensor*, which gives rise to the chemical shift. The

Hamiltonian of the chemical shift can be described by:

$$\mathcal{H}_{\mathrm{cs}} = \gamma\, \hbar\, \vec{I} \cdot \hat{\sigma} \cdot \vec{B}_0. \tag{1.15}$$

In order to quantify the chemical shift δ independent of the magnetic field, the measured frequency ω is expressed in relation to the frequency ω_{ref} of a reference substance:

$$\delta/ppm = \frac{\omega - \omega_{\mathrm{ref}}}{\omega_{ref}} \cdot 10^6. \tag{1.16}$$

The abbreviation "ppm" herein stands for "parts per million". In cases of anisotropic shielding of the nucleus by the shell electrons, a so-called *Chemical Shift Anisotropy (CSA)* can be observed.

Another effect is caused by the interaction of the magnetic field associated with the nuclear magnetic moment with the magnetic field of the surrounding magnetic moments. Since two nuclear spins couple directly without the influence of electrons, this interaction is known as *direct dipole-dipole coupling*. The energy of two spins j and k with distance r_{jk} is:

$$E_{jk}^{\mathrm{DD}} = \left\langle \mathcal{H}_{jk}^{\mathrm{DD}} \right\rangle \tag{1.17}$$

$$= \left\langle \frac{\mu_0}{4\pi} \frac{\hbar\, \gamma_j \gamma_k}{r_{jk}^3} [3(\vec{I}_j \cdot \hat{e}_{jk})(\vec{I}_k \cdot \hat{e}_{jk}) - \vec{I}_j \cdot \vec{I}_k] \right\rangle \tag{1.18}$$

$$= \frac{\mu_0}{4\pi} \left[\frac{\vec{\mu}_j \cdot \vec{\mu}_k}{r_{jk}^3} - \frac{3(\vec{\mu}_j \cdot \vec{r}_{jk})(\vec{\mu}_k \cdot \vec{r}_{jk})}{r_{jk}^5} \right]. \tag{1.19}$$

For isotropic gases and liquids, the dipole-dipole interaction decreases rapidly with r_{jk}^3 and generally is negligible.

As soon as the shell electrons also couple to the nuclear magnetic moment, *indirect spin-spin coupling*, also called *indirect scalar coupling* or short *J-coupling*, has to be taken into account. The participation of the electrons changes the direction of the interaction. In an isotropic fluid, this may lead to an anisotropic component that remains after motional averaging. The Hamiltonian of the J-coupling reads:

$$\mathcal{H}_{jk}^{J} = \vec{I}_j \cdot \hat{J}_{jk} \cdot \vec{I}_k. \tag{1.20}$$

The *J-coupling tensor* $\hat{J}_{jk}$ describes the dependence on the molecular orientation. The chemical shift contains information on the local electronic environment of the nuclear spin

and the J-coupling provides further insight into the chemical bonds.

The term $\mathcal{H}_\mathrm{Q}$ describing the coupling of the magnetic quadrupole to surrounding electric fields is only non-zero for spins with $I > 1/2$. Therefore, it can be neglected here for ^{1}H and ^{129}Xe.

1.2. Classical Model: Polarization and Relaxation

For a theoretical description of the experimental observations in NMR, it is convenient to refer to the classical formalism introduced in 1946 by Felix Bloch and to look at the macroscopic distribution of nuclei [Bloch 46a]. The total magnetic moment $\vec{M}$ is the sum of all n individual nuclear moments in a group of identical, independent spin-1/2 nuclei with gyromagnetic ratio γ,

$$\vec{M} = \sum_{i=1}^{N} \vec{\mu}_i. \tag{1.21}$$

This magnetization can classically be quantified with the help of the *polarization* P,

$$P = \frac{|N_- - N_+|}{N_- + N_+}. \tag{1.22}$$

The population numbers $N_\pm$ give the number of spins in the respective Zeeman state $m_I = \pm 1/2$, the ratio of which is expressed by the Boltzmann distribution,

$$\frac{N_-}{N_+} = \frac{\mathrm{e}^{-E_-/k_\mathrm{B}T}}{\mathrm{e}^{-E_+/k_\mathrm{B}T}} = \mathrm{e}^{-\Delta E/k_\mathrm{B}T}, \tag{1.23}$$

where k_B is the Boltzmann constant and T the temperature. With this population ratio Eq. (1.22) can be rewritten as

$$P = \tanh\left(\frac{\Delta E}{2k_\mathrm{B}T}\right) = \tanh\left(\frac{|\gamma|\,\hbar\,B_0}{2k_\mathrm{B}T}\right). \tag{1.24}$$

The net magnetization M of a sample thus is in first order of the *high temperature approximation*, $|\gamma|\,\hbar\,B_0 \ll k_\mathrm{B}T$, that generally holds valid,

$$M = |\vec{M}| = \gamma\hbar NP \approx \frac{\hbar^2\gamma^2 N B_0}{2k_\mathrm{B}T}. \tag{1.25}$$

In a magnetic field $\vec{B}$, the macroscopic magnetic moment $\vec{M}$ experiences a torque $\vec{M}\times\vec{B}$. By equating this torque with the temporal change of the angular momentum, $\vec{M}/\gamma$, the

equation of motion is obtained:

$$\frac{d\vec{M}}{dt} = \gamma \vec{M} \times \vec{B}. \tag{1.26}$$

The solution of this equation corresponds to a precession of the magnetization around the field with a frequency ω_0. In order to include the effect of irradiating an rf pulse, Eq. (1.26) can be rewritten:

$$\frac{d}{dt}\begin{pmatrix} M_x \\ M_y \\ M_z \end{pmatrix} = \begin{pmatrix} 0 & -\Omega_0 & \omega \sin\phi_{\text{rec}} \\ \Omega_0 & 0 & -\omega\cos\phi_{\text{rec}} \\ -\omega\sin\phi_{\text{rec}} & \omega\cos\phi_{\text{rec}} & 0 \end{pmatrix} \begin{pmatrix} M_x \\ M_y \\ M_z \end{pmatrix}. \tag{1.27}$$

Here, ϕ_{rec} is the phase of the receiver and $\Omega_0 = \omega - \omega_0$ the difference between Larmor frequency ω_0 and the rf frequency ω. The final solution of the differential equation with the initial condition $\vec{M}(t) = M_0\,\hat{e}_z$ then is:

$$\begin{pmatrix} M_x \\ M_y \\ M_z \end{pmatrix} = M_0 \begin{pmatrix} \sin(\omega t)\sin(\Omega_0 t) \\ \sin(\omega t)\cos(\Omega_0 t) \\ \cos(\omega t) \end{pmatrix}. \tag{1.28}$$

It implies that the magnetization precesses around the longitudinal $\vec{B}_0$ field with Ω_0 and simultaneously with ω around the rf field. When choosing a reference frame rotating with ω_0, Eq. (1.28) simplifies to a precession around $\vec{B}_1$. The rf field $\vec{B}_1$ typically takes values of approximately 10^{-4} T, so that the precession frequency around $\vec{B}_1$ for ^{1}H is 10 kHz [Callaghan 93].

Whenever $\omega \neq \omega_0$, the longitudinal component of the effective field in the rotating frame is non-zero,

$$\vec{B}_{\text{eff}} = \vec{B}_0 - \vec{B}_1 = \vec{B}_0 - \vec{\omega}/\gamma, \tag{1.29}$$

and the magnetization rotates around $\vec{B}_{\text{eff}}$. Under the influence of a short rf pulse of length t, the magnetization thus rotates by a *flip angle* $\alpha = \omega t$. Since the direction of the rf pulse in the *laboratory frame* depends on the time of irradiation, it usually is chosen with reference to the receiver phase ϕ_{acq}, which assigns the rotating frame. The direction of the rf field in the *rotating frame* can be varied deliberately by varying the pulse phase ϕ_i. In most experiments, the pulse phase in subsequent scans is varied by angles predefined in a *phase cycling* scheme in order to average out inaccuracies of the rf pulses and to choose certain coherence pathways.

By turning the magnetization away from the longitudinal magnetic field $\vec{B}_0$, a state of

non-equilibrium is obtained. Hence, the system returns to equilibrium by the process of *longitudinal relaxation*, by which energy is exchanged with the surroundings. For solids, this is constituted by the molecular lattice, which has given rise to the name *spin-lattice relaxation*. Phenomenologically, this process can be expressed by means of the following differential equation,

$$\frac{dM_z(t)}{dt} = -\frac{M_z - M_0}{T_1}. \tag{1.30}$$

Assuming for $t = 0$ $M_z(0) = 0$, for example after a 90° rf pulse, the solution,

$$M_z(t) = M_0 + (M_z(0) - M_0) \cdot \mathrm{e}^{-\frac{t}{T_1}}, \tag{1.31}$$

is an exponential with time constant T_1, the so-called *longitudinal relaxation time*.

Another effect is the *transverse* or *spin-spin relaxation* characterized by the *transverse relaxation time* T_2. As implied by the nomenclature, it is caused by the interaction of the spins that loose phase coherence in thermal equilibrium. Figure 1.5 schematically illustrates this process. Since indirect as well as direct interactions with the environment

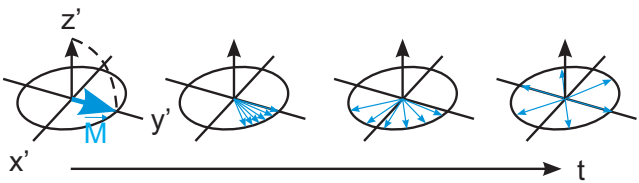

Figure 1.5.: Schematic demonstration of loss of spin coherence due to spin-spin relaxation.

can contribute, $T_2 \leq T_1$ always holds valid in the frame of Redfield relaxation theory[1]. The condition of weak relaxation interactions, also known as BBP (Bloemberg, Purcell, Pound) condition [Bloembergen 48], generally is valid:

$$\frac{dM_{x,y}(t)}{dt} = -\frac{M_{x,y}}{T_2}, \tag{1.32}$$

with solutions

$$M_{x,y}(t) = M_{x,y}(0) \cdot \mathrm{e}^{-\frac{t}{T_2}}. \tag{1.33}$$

[1]Theoretically, both relaxation rates can be expressed by the spectral densities at frequencies of zero-, single-, and double-quantum coherences. While $1/T_1$ is only influenced by the last two coherences corresponding to a true energy exchange, an additional summand of zero-quantum coherence is added to the transverse relaxation rate.

With Eq. (1.28), equations of motion can be given for the magnetization that include all these effects, the so-called *Bloch equations*:

$$\frac{d}{dt}\begin{pmatrix} M_x \\ M_y \\ M_z \end{pmatrix} = \begin{pmatrix} 0 & -\Omega_0 & \omega\sin\phi \\ \Omega_0 & 0 & -\omega\cos\phi \\ -\omega\sin\phi & \omega\cos\phi & 0 \end{pmatrix}\begin{pmatrix} M_x \\ M_y \\ M_z \end{pmatrix} - \begin{pmatrix} \frac{M_x}{T_2} \\ \frac{M_y}{T_2} \\ \frac{M_z-1}{T_1} \end{pmatrix}. \tag{1.34}$$

In real experiments, the transverse relaxation time is additionally influenced by local effects,

$$\frac{1}{T_2^*} = \frac{1}{T_2} + \frac{1}{T_2'} + |\gamma \cdot \nabla B \cdot d|\,, \tag{1.35}$$

where T_2^* includes signal attenuation by local susceptibility differences ($1/T_2'$) and external magnetic field inhomogeneities over a distance d (∇B).

1.3. NMR Signal and Fourier-Transform NMR Spectroscopy

Even though the precessing transverse magnetization after an rf pulse is very small, its well-defined frequency allows systematic detection. The rotating magnetic moment induces a potential difference in a nearby coil according to the Maxwell equations, which is converted to a current via a resistor and then measured by a sensitive rf receiver. Thereby, the axis of the rf coil needs to be aligned perpendicular to the main magnetic field $\vec{B}_0$ in order to allow measurement of the transverse magnetization. The induced voltage oscillating at the Larmor frequency is termed *NMR signal* or *Free-Induction Decay (FID)* [Bloch 46b] and is sketched in Fig. 1.6.

The solutions of Eq. (1.34) in the rotating frame describe the signal after an rf pulse with flip angle α,

$$M_x(t) = M_0 \sin(\alpha)\sin(\Omega_0 t)\mathrm{e}^{-t/T_2^*} \tag{1.36}$$

$$M_y(t) = -M_0 \sin(\alpha)\cos(\Omega_0 t)\mathrm{e}^{-t/T_2^*}\,, \tag{1.37}$$

which can be combined to the total complex signal $s(t) = M_x(t) + iM_y(t)$. Following the method of *Fourier transform (FT) spectroscopy* [Ernst 66; Ernst 92], the *frequency*

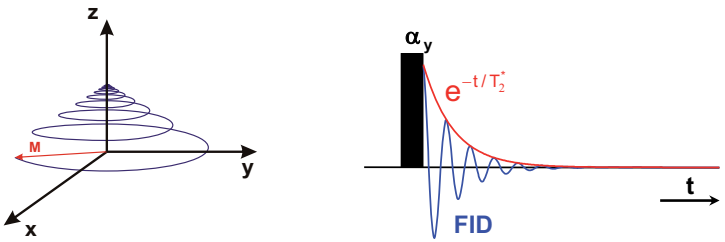

(a) Magnetization vector $\vec{M}$ (b) FID

Figure 1.6.: (a) Temporal evolution of the magnetization vector after a $\alpha = 90°$ rf pulse. (b) Scheme of the resulting FID signal.

spectrum $S(\omega)$ can be calculated as the real part of the Fourier transform of the time signal $s(t)$ as illustrated in Fig. 1.7. The peak shape is described by a Lorentzian with the maximum at the Larmor frequency ω_0:

$$S(\omega) = \mathrm{Re}\left\{\int_{-\infty}^{+\infty} dt\, s(t)\mathrm{e}^{-i\omega t}\right\} = \frac{\lambda}{\lambda^2 + (\omega - \omega_0)^2}. \tag{1.38}$$

The parameter $\lambda = 1/T_2^*$ is called *coherence decay rate constant* and denotes the full

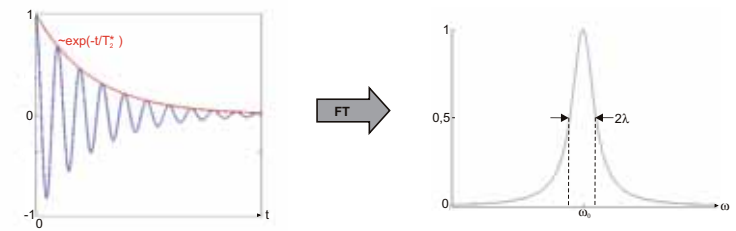

Figure 1.7.: Left: FID, right: resulting NMR spectrum.

width at half maximum (FWHM) $\Delta\omega$ of the signal peak,

$$\Delta\omega = 2\lambda = \frac{2}{T_2^*}. \tag{1.39}$$

A problem associated with FT NMR is caused by conversion of the analog into a digital signal by the NMR receiver (cf. Chapter 3) and the subsequent Fourier transformation.

The analog signal is sampled by the ADC (analog-to-digital converter) with a frequency $\nu_s = 1/\tau_s$ periodically in time steps τ_s. The *Nyquist theorem*, named after Harry Nyquist who stated it in 1928,

$$\nu < \frac{1}{2}\nu_s = \nu_{Ny} \tag{1.40}$$

says that the sampling frequency ν_s has to be at least twice as high as the largest frequency ν in the spectrum [Nyquist 28]. This has led to the introduction of the *Nyquist frequency* $\nu_{Ny} = 1/2\,\nu_s$, above which frequencies cannot be measured unambiguously, anymore. This issue is demonstrated again in Fig. 1.8 in the time domain, as well as in Fig. 1.9 in the frequency domain. Since frequencies outside the frequency band $(-\nu_s/2, \nu_s/2)$ reappear

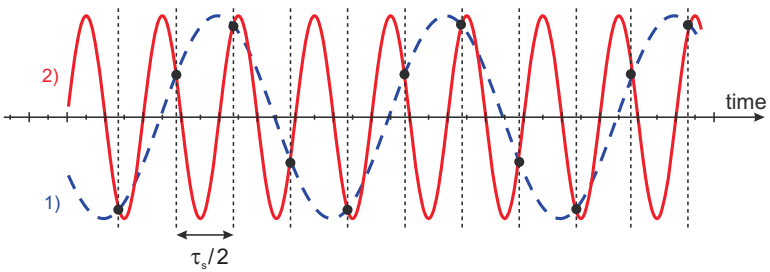

Figure 1.8.: Origin of the alias effect: With the sampling frequency ν_s, only the blue dashed sine function (1) can reliably be reproduced. Since the frequency of the red curve (2) $\nu_2 > \nu_s/2$, it is mis-interpreted as ν_1 as well.

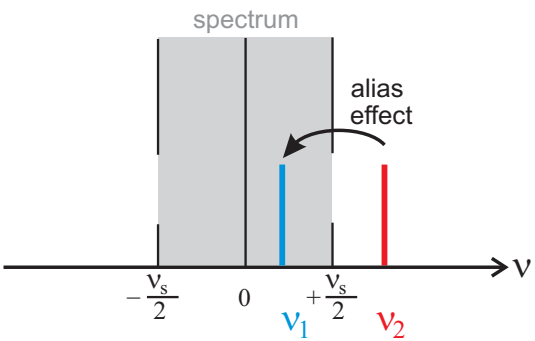

Figure 1.9.: Effect of aliasing: The frequency $\nu_2 > \nu_{Ny} = \nu_s/2$ is back-folded onto ν_1 by discrete Fourier transformation.

in this interval, this effect is also called *back-folding* or *aliasing*. In order to prevent a resulting overlap of noise signals $\nu > \nu_s/2$ onto the spectrum of interest, low-pass filters are employed, suppressing all frequencies above the Nyquist frequency ν_{Ny}.

1.3.1. Sensitivity and Signal Enhancement

The sensitivity of an NMR experiment is governed by the total magnetization M and the induction voltage in the rf coil. The induced current in the coil is proportional to the gyromagnetic ratio γ and, according to Faraday's law, proportional to the square of the Larmor frequency $\omega_0^2 = (\gamma B_0)^2$,

$$S \propto \gamma^3 B_0^2. \tag{1.41}$$

The root mean square of the random noise N in the spectrum increases with $\sqrt{\omega_0}$ [Levitt 05], so that the following expression results for the signal-to-noise ratio (SNR):

$$SNR \propto \gamma^{\frac{5}{2}} B_0^{\frac{3}{2}} NS^{\frac{1}{2}}, \tag{1.42}$$

where NS is the number of scans. The possibility of adding several scans before performing the Fourier transformation and thereby increasing the SNR even allows for detection of very small signals. This method is called *signal averaging*.

In order to further enhance the sensitivity or resolution of the spectrum, the time-dependent signal (Fig. 1.6),

$$s(t) = s^e(t) \exp\{i\,\Omega_0\,t\}, \tag{1.43}$$

with the signal envelope $s^e(t)$ which determines the spectral peak shape can be multiplied by a weighting function $h(t)$. This is equivalent to convolution filtering in the frequency domain. It can be shown [Ernst 87], that $h(t) = s^e(t)$ has to be chosen for optimal SNR which is also known as a *matched filter*. Thereby, the decaying signal is hardly influenced, while noise is efficiently suppressed. Since the Fourier transform of an exponential is a Lorentzian, slightly higher line widths are obtained in the NMR spectrum. An alternative filter is a Gaussian function which is invariant under FT and is particularly well-suited for distinction of narrow-spaced signals because it yields a smaller spectral width at the base. Since the original Lorentz shape of the signal peak is modified to a Gaussian spectral line by this filter, it is also known as *Lorentz-Gauss transformation*.

Especially in the field of imaging, so-called *zero-filling* is widely used.The data set of the decaying signal is artificially padded by zeros in order to improve FT properties. Typically, data is zero-filled to twice up to four times the original data matrix size.

1.3.2. Spin Echo

Besides the FID, one of the simplest but most important NMR experiments is the *spin echo (SE)*, which has first been published by Erwin Hahn in 1950 and, in its basic form, is thus also known as the *Hahn echo* [Hahn 50]. In Fig. 1.10, the pulse sequence with resulting signals (top) as well as the behavior of the magnetization in the rotating frame (bottom) are demonstrated. By applying a 90°_x pulse, the magnetization is flipped from the $z-$ onto

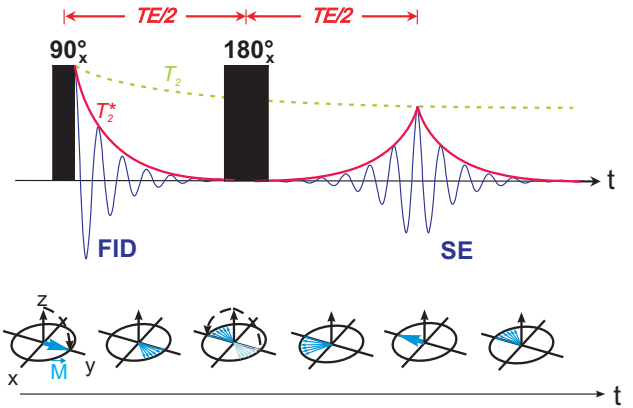

Figure 1.10.: Spin echo pulse sequence with resulting signal (top), as well as behavior of the magnetization in the rotating frame (bottom)

the $-y$-axis. The index x of the flip angle denotes the direction of rf irradiation. The spins start to dephase due to the transverse relaxation effect - the above discussed FID signal develops. If now after a time period $TE/2$ a 180°_x pulse is applied, the magnetization is *refocused* due to the same effects that led to the dephasing in the beginning. Figuratively, the time evolution is reversed by the 180°_x pulse, so that the spins return to their initial, coherent state. Thus, the first almost completely decayed FID signal reappears after a time TE, the so-called *echo time*, as the spin echo. Due to T_2 relaxation, only a maximum magnetization of M_{SE} is reached,

$$M_{\mathrm{SE}} = M_0 \cdot \mathrm{e}^{\frac{TE}{T_2}}. \tag{1.44}$$

1.3.3. 2D NMR Spectroscopy

In order to measure complex dynamic process, a new approach has first been introduced by Jeener et al. in 1979, and in 1991, R. Ernst was awarded the Nobel Prize for its realization: by acquiring two-dimensional NMR spectra, correlations can now directly be measured [Jeener 79; Perrin 90]. Various pulse schemes have been developed since then revealing different dynamic characteristics. In this work, exchange between sites that are characterized by different chemical shifts is of interest. The according pulse scheme for this *EXSY (EXchange SpectroscopY)* experiment is depicted in Fig. 1.11.

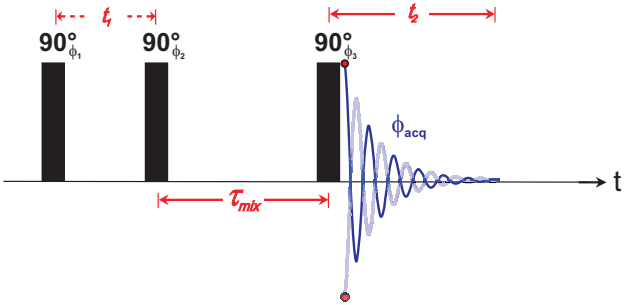

Figure 1.11.: 2D exchange spectroscopy (EXSY) pulse scheme. The time t_1 is varied in order to introduce the second dimension, which results in a phase shift of the signal during t_2.

Consider a spin-1/2 system with symmetric exchange between two chemical states A and B at a rate k. The first 90° pulse flips all longitudinal magnetization onto the x-y plane. Magnetization in state A evolves under ω_A during the time interval t_1, which is increased stepwise with each cycle introducing the second dimension of the 2D experiment. Within the following time period τ_{mix}, the *mixing time*, magnetization is stored in the longitudinal direction and can exchange between the different sites of the sample. If magnetization exchanges from state A to B, it will be recorded with ω_B during t_2 and thus will give rise to an *exchange peak* at position (ω_A, ω_B). If the exchange process is symmetric, it will be reflected by symmetric exchange peaks in the 2D spectrum. If there is no exchange or the mixing time is short on the scale of the exchange time $1/k$, it will give rise to diagonal peaks only. Thus, the cross-peak amplitudes provide quantitative information on the exchange rate. A schematic drawing of spectra with different ratios of mixing time τ_{mix} and exchange rate k is shown in Fig. 1.12.

In this model, it is assumed that encoding times t_1 and t_2 are short on the time scales

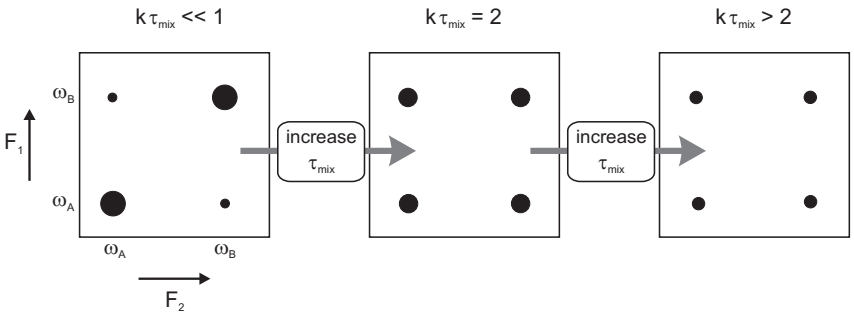

Figure 1.12.: 2D EXSY spectra for varying ratios of mixing time τ_{mix} and exchange rate k for symmetrical two-site exchange.

of the mixing times τ_{mix}, so that exchange during encoding can be neglected. If the spin-lattice relaxation times of both states A and B are the same, $T_1^A = T_1^B = T_1$, the amplitudes of diagonal and cross peaks are given by [Levitt 05]:

$$a_{\mathrm{diag}}(\tau_{\mathrm{mix}}) = \cosh(k\,\tau_{\mathrm{mix}}) \exp\left\{-(k + T_1^{-1})\tau_{\mathrm{mix}}\right\}, \tag{1.45}$$

$$a_{\mathrm{cross}}(\tau_{\mathrm{mix}}) = \sinh(k\,\tau_{\mathrm{mix}}) \exp\left\{-(k + T_1^{-1})\tau_{\mathrm{mix}}\right\}. \tag{1.46}$$

Since a series of 90° pulses also excites unwanted signals like spin and stimulated echoes, a proper phase cycle has to be chosen to follow the desired coherence pathway, i.e. unwanted signal contributions are canceled while desired contributions are coherently averaged. One choice for EXSY experiments is *TPPI (Time-Proportional Phase Incrementation)*, an eight-step phase cycle shown in Tab. 1.1 [Marion 83].

Table 1.1.: Eight-step phase cycle appropriate for 2D EXSY experiments following the TPPI scheme.

Cycle counter	ϕ_1	ϕ_2	ϕ_3	ϕ_{acq}
1	x	x	x	x
2	-x	x	x	-x
3	x	x	-x	-x
4	-x	x	-x	x
5	x	x	y	y
6	-x	x	y	-y
7	x	x	-y	-y
8	-x	x	-y	y

Chapter 2.

Magnetic Resonance Imaging (MRI)

Magnetic resonance imaging (MRI) has developed into a standard method for medical diagnostics during the last decades, but is also of increasing importance for material research and engineering processes. Its fundamental principle is based on ideas of Paul C. Lauterbur und Sir Peter Mansfield [Lauterbur 73; Mansfield 73], for which they were awarded the Nobel Prize for medicine in 2003: For the necessary spatial encoding of the NMR signal, they superimposed a magnetic field wtih a gradient $\vec{G} = \vec{\nabla} B_z$ onto the main magnetic field $\vec{B}_0$. Thereby, the measured parameter, the Larmor frequency $\omega_0 = \gamma B$, becomes spatially dependent,

$$\omega_0(\vec{r}) = \gamma(B_0 + \vec{G} \cdot \vec{r}). \tag{2.1}$$

In the following, first a formalism is introduced that visualizes the spatial encoding and the various MRI methods, before basic MRI experiments are presented.

2.1. Introduction to k-Space Formalism

The acquisition of a NMR signal in the presence of a magnetic gradient field is also called *k-space sampling* and can be described with the help of the formalism introduced in 1983 by Stig Ljunggren und Donald B. Twieg [Ljunggren 83; Twieg 83]. They were able to show that the signal $s(t)$ of freely precessing spins under the influence of a constant gradient G is the Fourier transform of the effective spin density ρ_{eff}. The term *effective* spin density refers here to the real spin density $\rho(\vec{r})$ corrected by the effects of T_1 relaxation, flow, diffusion, etc. The dynamic analogon is q-space sampling, which encodes the nuclear spins relative to their velocities. It is used, e.g. for analysis of the spectrum of molecular motion as well as for investigations of porous systems. For representation in k-space, first the signal ds generated by a number of nuclear spins within a volume dV, $\rho_{\text{eff}}(\vec{r})\, dV$, is

written as

$$ds(\vec{G},t) = \rho_{\text{eff}}(\vec{r})\, dV \cdot \mathrm{e}^{-i[\gamma(B_0+\vec{G}\cdot\vec{r})t]}. \tag{2.2}$$

Here, T_2^* relaxation effects can be neglected, as long as the gradient is strong enough, i.e., the dephasing of transverse magnetization is dominated by the gradient. Because this condition is valid for all imaging experiments in this work and furthermore, the B_0-term drops for resonant rf irradiation, after integration the relation reads:

$$s(t) = \int d^3r\, \rho(\vec{r}) \cdot \mathrm{e}^{i\gamma\vec{G}\cdot\vec{r}t}. \tag{2.3}$$

This equation corresponds to a Fourier transformation. In order to point this out, Mansfield used the concept of the reciprocal spatial vector $\vec{k}$,

$$\vec{k}(t) = \frac{\gamma\, \vec{G}\, t}{2\pi}, \tag{2.4}$$

in order to reformulate Eq. (2.3):

$$s(\vec{k}) = \int d^3r\, \rho(\vec{r}) \cdot \mathrm{e}^{2\pi i\, \vec{k}(t)\cdot\vec{r}}, \tag{2.5}$$

$$\rho(\vec{r}) = \int d^3k\, s(\vec{k}) \cdot \mathrm{e}^{-2\pi i\, \vec{k}(t)\cdot\vec{r}}. \tag{2.6}$$

Thus, the NMR signal $s(\vec{k})$ and the spin density $\rho(\vec{r})$ are conjugate variables in an ideal experiment.

2.2. Frequency and Phase Encoding

In practice, k-space sampling is performed by measurement of the NMR signal in step-wise time intervals, i.e. $s(\vec{k})$ is measured in the time domain resulting via FT in a frequency dependent $\rho(\vec{r})$. If $\rho(\vec{r})$ is regarded as a three-dimensional spectrum of $s(\vec{k})$, an equivalence of space and frequency and reciprocal space and time is noticed. When carrying out the integration over the z direction in Eq. (2.6), the spectral data obviously can be regarded as a projection of the spin density onto the z axis (Fig. 2.1). This idea of measuring spatially dependent frequencies is known as *frequency encoding*.

In experiments with constant *read* gradient $\vec{G}_{\text{read}}$, a single line in k-space is scanned. For two-dimensional imaging, the second spatial dimension is measured by means of *phase encoding*: another gradient is pulsed before the read-out leading again to spatially varying

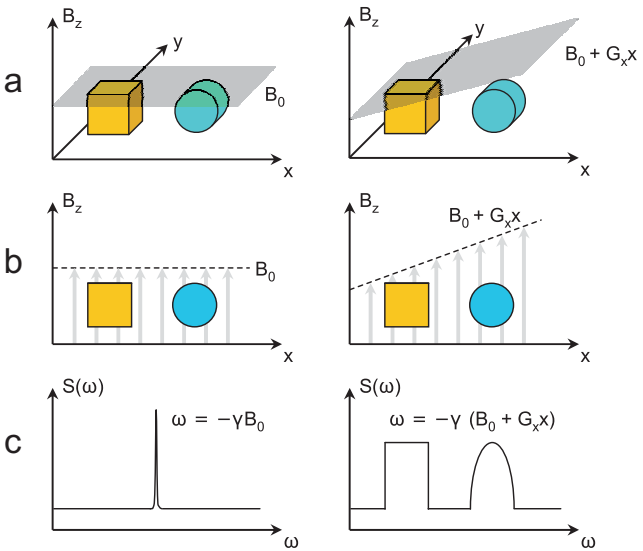

Figure 2.1.: Scheme of space encoding by a magnetic gradient field (right) in comparison with the situation in a constant field (left), here shown with the example of a cube and a cylinder: (a) spatial dimension, (b) projection of spatial dimension onto x-z plane, (c) resulting spectrum.

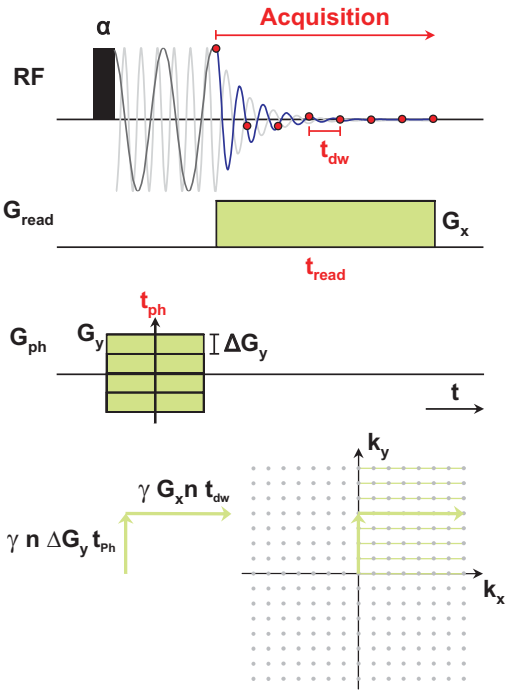

Figure 2.2.: Pulse sequence for acquisition of image information by means of frequency and phase encoding. The frequency and phase of the transverse magnetization is altered by pulsed gradients for space encoding. The scheme presented here results in linear k-space sampling.

frequencies. At the end of the phase gradient switching time, t_{ph}, this results in space-dependent phases. By incrementing the phase gradient strength, all lines in k-space are scanned. In Fig. 2.2, the according pulse scheme is depicted.

Better visualization of how image information is contained in k-space is provided by Fig. 2.3. While signal intensities are encoded in the center yielding the image *contrast*, information on definition of edges, i.e., *sharpness* of the image, is encoded in the peripheral areas. While sometimes inhomogeneous k-space sampling leads to effects that are unwanted and need to be improved by specially designed filters, they are deliberately made use of in other applications.

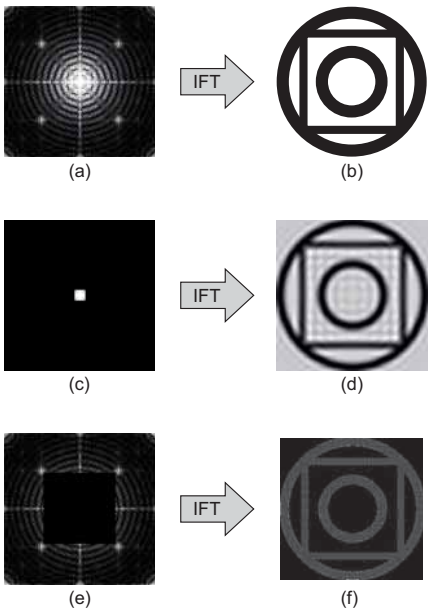

Figure 2.3.: Influence of different areas of k-space on image quality. (a) complete k-space and (b) original image; (c) k-space center yielding an image (d), which has high contrast but is blurred; (e) periphery resulting in (f) enhanced edges.

Because position vector $\vec{r}$ and k-space vector $\vec{k}$ are conjugate variables, the Nyquist theorem can be used to derive two basic image parameters: the *Field Of View (FOV)* depending on the step size Δk in k-space and the *resolution* Δr depending on the maximum

k-value, $k^{\max}$,

$$\mathrm{FOV} \propto \frac{1}{\Delta k} \tag{2.7}$$

$$\Delta r \propto |k^{\max}|\,. \tag{2.8}$$

For frequency encoding in read direction, this means:

$$\mathrm{FOV}_{\mathrm{read}} = \frac{2\pi}{\gamma\, G_{\mathrm{read}}\, DW}, \tag{2.9}$$

where G_{read} is the gradient strength and DW is the dwell time, i.e., the time between the acquisition of two data points. The experimental NMR signal is the convolution of true spatial information with the *Point Spread Function (PSF)* of the signal acquisition, which reflects how a single point would be reproduced by the measuring procedure. Since this information is already contained in the NMR spectrum in absence of the encoding gradients, Δr_{read} is defined in terms of the line width $\Delta\omega$ as

$$\Delta r_{\mathrm{read}} = \frac{\Delta\omega}{\gamma\, G_{\mathrm{read}}}. \tag{2.10}$$

Analogously, both expressions are obtained for phase encoding based on the correspondence of time and phase:

$$\mathrm{FOV}_{\mathrm{ph}} = \frac{2\pi}{\gamma\, \Delta G_{\mathrm{ph}}\, t_{\mathrm{ph}}}, \tag{2.11}$$

with the step size ΔG_{ph} and duration t_{ph} of the phase gradient. The resolution in phase direction Δr_{ph} is determined by the FOV per pixel, the total number of which is given by the n gradient steps,

$$\Delta r_{\mathrm{ph}} = \frac{\mathrm{FOV}_{\mathrm{ph}}}{n} = \frac{2\pi}{\gamma\ |G_{\max}|\, t_{\mathrm{ph}}}. \tag{2.12}$$

The maximum resolution in phase encoding usually is either limited by total acquisition time or by the maximum gradient strength of the system, $G_{\max} \geq n\Delta G_{\mathrm{ph}}$.

2.3. Slice Selection

For detailed MRI analysis of a sample, 2D projections acquired by the frequency- and phase encoding scheme described before sometimes are not sufficient. Even though the concept of phase encoding can be directly extended to a three-dimensional MRI scheme, it is very time consuming and therefore often unfeasible.

As an alternative, a single slice of the object can be imaged. The easiest and most common approach is demonstrated in Fig. 2.4. A slice gradient in the direction perpendicular

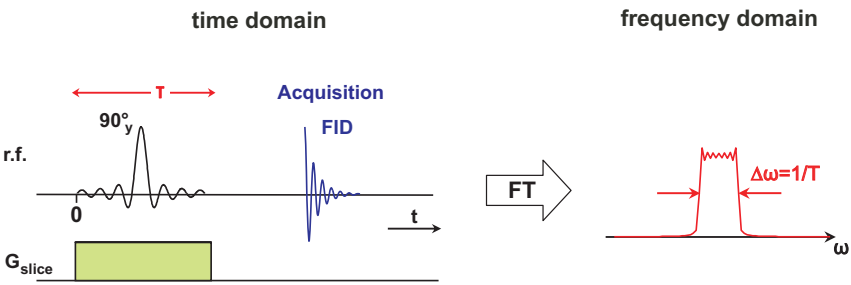

Figure 2.4.: Illustration of a simple pulse program for slice selection by direct generation of transverse magnetization with a sinc-shaped rf pulse, which is applied simultaneously with a slice selection gradient pulse. Fourier transformation yields the desired profile, which experiences distortions due to the truncation of the sinc-pulse.

to the desired slice plane yields the required spatially dependent frequency distribution. By replacing the rectangular *hard* rf pulse by a sinc[1]-shaped *soft* pulse, a well-defined rectangular frequency window can be excited. In first approximation, the slice thickness defined by the spectral width $\Delta\omega$ is inversely proportional to the rf pulse length Δt_p

$$\Delta\omega \propto \frac{1}{\Delta t_\mathrm{p}}. \tag{2.13}$$

The exact relation between the pulse length and the slice thickness depends on the practical implementation of the theoretically infinite sinc-pulse, especially on the number of side-lobes that are included. Conversion factors are usually obtained numerically. Because the slice gradient in combination with the long soft pulse causes considerable dephasing of the transverse magnetization, a refocusing gradient is sometimes applied after slice selection.

2.4. Imaging Sequences

As MRI is one of the key aspects of this work, the basic imaging sequences employed will be described in the following. A basic imaging experiment simply combines the idea of the spin echo (SE) with frequency and phase encoding gradients. In Fig. 2.5, this method

[1] $\mathrm{sinc}(x) = \sin(x)/x$

is demonstrated graphically. While the first read gradient is turned on, magnetization dephases. The 180° pulse inverts the direction of dephasing. During the rephasing read gradient the magnetization is refocused. With proper timing and gradient strengths, the echo maximum coincides with the center of the acquisition window for optimal SNR.

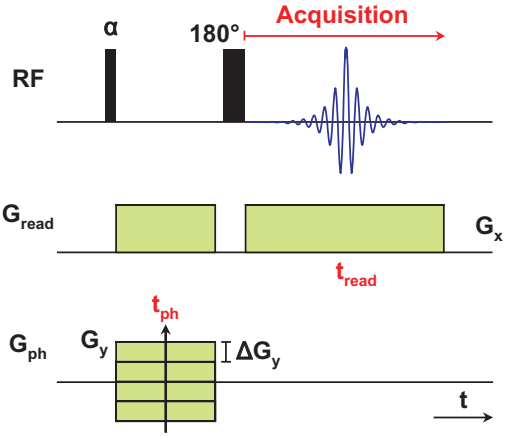

Figure 2.5.: Scheme of a basic spin-echo imaging sequence.

An essential requirement for all SE sequences is an exact calibration of the 180° flip angle, however. Whenever this prerequisite is not fulfilled or if the number of rf pulses has to be reduced, *gradient echo (GE)* imaging can serve as a good alternative. Instead of the 180°, an inversion of the direction of the first dephasing read gradient yields proper refocusing conditions. A more advanced version of this basic GE, the so-called *FLASH (Fast Low Angle SHot)* sequence has been introduced in 1986 by Axel Haase and Jens Frahm [Haase 86]. It allows for significant reduction of measurement time by employing very small flip angles α. This allows for very short repetition times TR because every rf pulse only uses a small fraction of net longitudinal magnetization. The signal intensity after the n-th pulse is given by:

$$S(n) \propto \cos\theta^{n-1} \sin\theta \, e^{\frac{-(n-1)TR}{T_1}}. \tag{2.14}$$

A non-echo based MRI technique is called *Filtered BackProjection (FBP)*. Directly after rf excitation, the read-out gradient is turned on and signal is acquired. This yields one-dimensional profiles. By varying the direction of the profile acquisition, 2D spatial

information is gained (Fig. 2.6a). The original image is reconstructed by an inverse *Radon transformation*, employing further algorithms for interpolation between acquired radial data onto a Cartesian grid [Radon 17; Kak 88; Bracewell 95]. Since the density of signal points in the center of k-space is higher than for frequency components in the outer regions, appropriate filters have to be employed. In this work, the filter used is based on the *Ram-Lak* or *ramp filter* the frequency response of which is $|f|$, multiplied by a *Hamming window* (Matlab R2008a, The MathWorks, Inc.). The final frequency response is demonstrated in Fig. 2.6b. Even though radial imaging implies more complex post-processing, it has

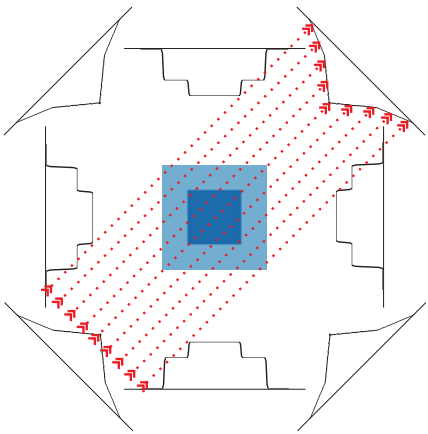

(a) Scheme of FBP

(b) Hamming filter

Figure 2.6.: Filtered Backprojection (FBP). (a) Scheme of acquisition scheme. (b) Frequency response of Hamming filter.

the advantage for medical MRI of highly reduced acoustic noise because the gradients are only stepped in very small increments to yield small changes in acquisition angles.

Chapter 3.

NMR Spectrometer

The NMR spectrometer basically has to meet three requirements: (i) polarization of the nuclear spin system by means of a magnetic field, (ii) excitation of the resulting magnetization via rf pulses, and (iii) detection of the weak alternating currents induced by the precession of transverse magnetization. A scheme of the necessary setup is shown in Fig. (3.1).

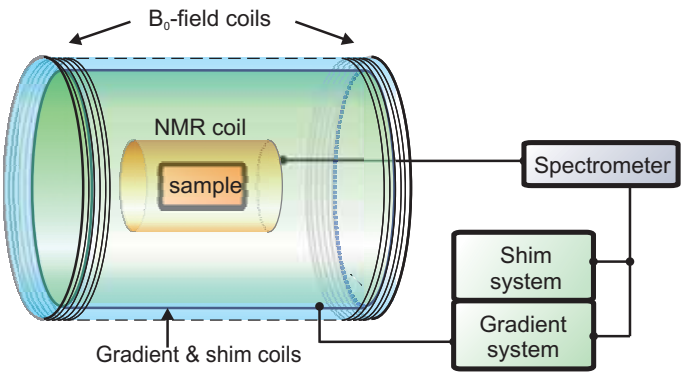

Figure 3.1.: Scheme of the spectrometer system.

For high-field NMR, the first function generally is fulfilled by a superconducting magnet. This magnet generating the main magnetic field B_0 is additionally equipped with a gradient and shim system consisting of additional coils to provide magnetic field gradients, e.g. for imaging purposes, and to compensate magnetic field inhomogeneities, respectively. The rf fields are generated within a transmitter unit and irradiated onto the sample by an rf coil by means of an electronic resonance circuit, the frequency of which is *tuned* to the desired resonance frequency by variable capacitors (Fig. 3.2). Furthermore, the

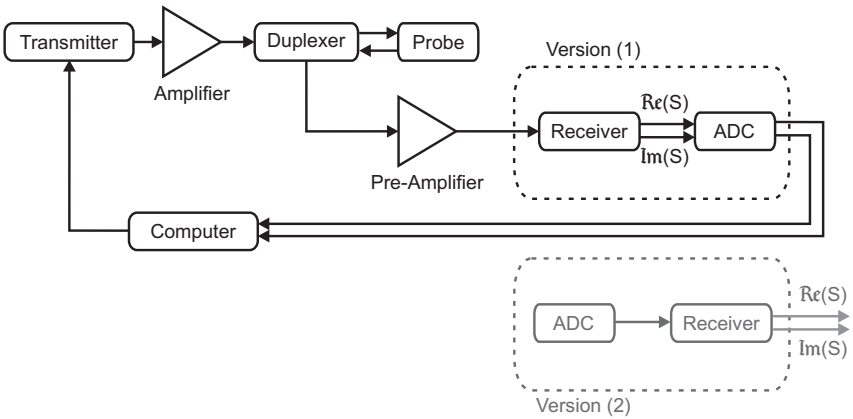

Figure 3.2.: Signal generation and processing system.

impedance of the circuit has to be *matched* by another variable capacitor to $50\,\Omega$, the standard value of the proceeding electronics, for optimal signal transfer. The geometry of the rf coil has to be chosen in such a way that the resulting $\vec{B}_1$ field is perpendicular to $\vec{B}_0$ and as homogeneous as possible in order to equally excite the magnetization across the sample. Standard solutions are solenoids, saddle coils, and as chosen in this work, so-called *birdcages*. For signal detection, the same coil can be used as soon as the rf excitation field has decayed, i.e. after the *dead time*. The switch between incoming and outgoing signal is realized by a duplexer. Since the detected signal is very weak, it is scaled up by a low-noise pre-amplifier directly after passing the duplexer.

Thereafter, the signal arrives at the receiver unit, where it is split and each part is mixed with the sine- and cosine-component of a reference wave, respectively, that oscillates at a lower frequency than the signal, i.e. typically at $\leq 1\,\mathrm{MHz}$. The mixing allows for better electronic signal processing because it results in a decreased signal frequency. The splitting into two components is known as *quadrature detection*: it artificially splits the signal into x and y components of the magnetization, which are treated as the real and imaginary parts of a now complex NMR signal. Both signals are then individually digitized in separate ADCs (analog-to-digital converters) before they are available in the computer for final processing. For receiving, another version has been developed due to the more advanced electronics (shown as Version (2) in Fig. 3.2): here, the NMR signal is directly digitized after the duplexer and only then reaches the receiver for quadrature detection avoiding

additional noise by mixing two analog signals.

In this work, two different NMR spectrometers were used. For Frank-sequence NMR, a Bruker DSX 200 MHz[1] spectrometer with a standard, vertical magnet bore hole of an inner diameter (ID) of 20 cm was used. It was equipped with a Bruker Micro 2.5 gradient system with a maximum strength of 1.50578 T/m. Bruker birdcage rf resonators of ID 10 mm and 20 mm were available. For hyperpolarized ^{129}Xe NMR experiments, a Bruker AV 300 MHz[2] spectrometer with a horizontal wide-bore magnet of ID = 40 cm was used, which was also equipped with a Bruker Micro 2.5 gradient system. Two ^{1}H/^{129}Xe-double resonant rf coils were employed with ID of 10 mm and 25 mm.

[1] 200 MHz ≅ 4.7 T for ^{1}H resonance.
[2] 300 MHz ≅ 7.0 T for ^{1}H resonance; for ^{129}Xe, a resonance frequency of 82.95 MHz results.

Part II.

Frank-Sequence Excitation

Chapter 4.

Introduction to Frank-Sequence NMR

A reduction of peak radio-frequency (rf) transmitter power in NMR experiments is of interest for different scenarios: For example, compact and miniaturized magnetic resonance has many applications in chemical engineering, biology, material testing [Lee 08; McDowell 08; Sillerud 06], as well as security [Garroway 01; Yesinowski 95]. A reduction or even elimination of large rf amplifiers benefits portability through savings in size and weight.

In medical MRI, great advances are made towards (ultra-) high static magnetic fields of strength $B_0 \geq 7\,\mathrm{T}$. On the one hand, high field strengths offer the great advantage of an intrinsically higher sensitivity leading to a higher Signal-to-Noise Ratio (SNR) and thus higher spatial and temporal resolution [Krug 09; Marques 10]. This allows for many new applications of MRI, in particular imaging of brain function. On the other hand, new issues arise: acoustic noise of more than 100 dB(A) generated by mechanical deformation of the gradient coils during switching is an important drawback of ultra high-field MRI [Budinger 91]. Moreover, due to increased susceptibility effects and changes in spin relaxation times, T_1 and T_2, image quality may be lost [Jezzard 96; Wansapura 99]. It therefore is essential to provide pulse sequences that also allow for measurement of short relaxation times. Another critical aspect is the exceeded SAR (Specific Absorption Rate) limit defined as the energy absorbed by body tissue per unit time and body weight [DIN 08]. Since it scales with the square of the main magnetic field strength, only small improvements could be achieved by modified rf coils and pulse sequences [Vaughan 01; Bottomley 78; Robitaille 98].

Solutions to these challenges may be found in low-power and low-energy excitation methods. The earliest NMR experiments were based on excitation with *Continuous*

Waves (CW) by either sweeping the strength of the applied magnetic field B_0 at constant rf frequency or vice versa by keeping B_0 constant and sweeping the rf frequency [Purcell 46; Bloch 46a]. CW NMR is performed in the *linear excitation regime* meaning that changes in longitudinal magnetization can be neglected, and that measured transverse magnetization is linearly proportional to the excitation field strength B_1. As rf excitation is irradiated continuously, saturation effects are avoided by low rf power levels. The NMR frequencies are scanned successively leading to the very low sensitivity of this method.

Pulsed excitation overcomes this disadvantage. It employs high peak excitation power yielding high impulse response power. While in CW NMR, the frequency spectrum is directly scanned yielding a narrow excitation bandwidth, the response of pulsed excitation experiments needs to be Fourier transformed [Ernst 66] and results in a broad spectrum. An intermediate technique is usage of a series of small CW pulses. This maintains the advantage of the low excitation power but excites all frequencies in a broad spectrum simultaneously. To retrieve the NMR spectrum from the response, the components of the response signal need to be assigned to the individual excitation pulses which therefor have to be distinguishable. One approach is to vary the rf amplitudes and phases in a random but known fashion. These ideas are realized in *noise excitation* and *stochastic NMR* [Ernst 70; Kaiser 70]. Both have the advantage of employing peak rf excitation powers that are several orders of magnitude lower than in NMR with single-pulse excitation. One realization of stochastic NMR is *Hadamard NMR* with constant rf amplitudes. Only pulse phases are varied pseudo-randomly between $\pm\pi/2$ following a phase modulation by binary sequences of numbers known as *m-sequences*. This sequence consists of $2m - 1$ points presenting a difficulty for *Fast Fourier Transformation (FFT)* algorithms that optimally require data lengths of powers of two. Furthermore, the power spectrum shows a singularity near the zero frequency. Both features can be eliminated with random noise excitation, however at the expense of forming ensemble averages of measurement traces upon calculation of the NMR spectrum [Blümich 87]. This prolongs the minimum measurement time from one scan in Hadamard NMR to the equivalent of many scans in NMR with white noise excitation. On the other hand, stochastic NMR provides strategies to measure multi-dimensional spectra by evaluation of the nonlinear response [Blümich 87; Paff 91; Paff 92].

The low sensitivity of CW NMR was improved by *rapid-scan NMR* [Dadok 74; Gupta 74]. The system response of such a rapid frequency sweep is a mixture of a resonance peak and a FID whenever a resonance frequency is met. Therefore, it is essential to avoid

interference of resonance lines and experiments have to be performed in the linear regime [Ferretti 76]. The possibility of acquiring also multidimensional spectra due to non-linear response components has made pulsed NMR an almost exclusive method for NMR and MRI.

Recently, different excitation schemes employing rf pulses with low power amplitudes have been introduced based on the idea of correlation NMR from 1974 [Dadok 74]: *Frank-sequence excitation* [Blümich 09; Amor 11], which will be discussed in detail in the subsequent chapters, and *SWIFT (Sweep Imaging With Fourier Transformation)* [Idiyatullin 06; Idiyatullin 08]. Both are based on the application of multiple low flip angle pulses with interleaved signal acquisition like in stochastic NMR. SWIFT NMR can be considered a pulsed version of rapid-scan NMR employing phase and amplitude modulated rf pulses. Even though low rf power is used, the response power is high and a white excitation profile is gained.

In the following, the fundamental theory of Frank-sequence NMR will be discussed (Chapter 5) and the relevant experimental setups will be presented (Chapter 6). Then, the focus will be on further investigations of the characteristics of the Frank-sequence method and on a detailed comparison to conventional hard-pulse NMR (Chapter 7). In Chapter 8, the application of the Frank-excitation scheme on MRI is shown and compared to standard imaging [Amor 11]. In order to achieve slice selection while maintaining low-power excitation, Frank excitation is combined with a technique called *SPREAD (Selective Pulses with REduced Amplitude Distribution)* [Nilgens 96] yielding three-dimensional MRI results.

Chapter 5.

Theory of Low-Power NMR and MRI

5.1. Frank Sequences

For use in NMR excitation, Frank sequences which have already been introduced in the early sixties and are commonly used in communication theory [Heimiller 61; Heimiller 62; Fan 96] are realized as so-called *polyphase perfect sequences*. Here, the term *polyphase* refers to phase modulation of the rf pulses, while *perfect* describes the constant absolute value of both the time-dependent function itself as well as of its Fourier transform. This translates into simple implementation of the phase modulation, which inherently allows for maximum pulse amplitude reduction, and into a white excitation profile, respectively.

For pure phase, constant-amplitude modulation of the rf pulses, rotating waves are chosen as the basic modulation function for the rf carrier because their frequencies are unambiguously determined by their phases at two points in time within one period, and because positive and negative frequencies can be distinguished:

$$x(t) = \exp(i\,2\pi\,f\,t). \tag{5.1}$$

Now, both time and frequency are discretized into m steps each:

$$f = \frac{f_\mathrm{w}}{m\,\Delta t},\ m \in \mathbb{N},\ 0 \le f_\mathrm{w} < m, \Delta t \cong DW, \tag{5.2}$$

$$t = t_\mathrm{w}\,\Delta t,\ 0 \le t_\mathrm{w} < m,\ t_n = m\,f_\mathrm{w} + t_\mathrm{w}, \tag{5.3}$$

where t_w and f_w serve as counters for the steps on the time and frequency grids, respectively, within one of the m wave packages. Substituting f and t in Eq. (5.1) by these new

expressions, the Frank sequence is obtained in the time-domain,

$$x(t_n\,\Delta t) = \exp(i\,2\pi\,\frac{f_{\mathrm{w}}\,t_{\mathrm{w}}}{m}), \tag{5.4}$$

consisting of $N = m^2$ pulses in time intervals of $\Delta t \cong DW$ (Dwell Time), as depicted in Fig. 5.1. As the maximum phase angle is 2π, the product $f_{\mathrm{w}}\,t_{\mathrm{w}}$ is evaluated modulo m.

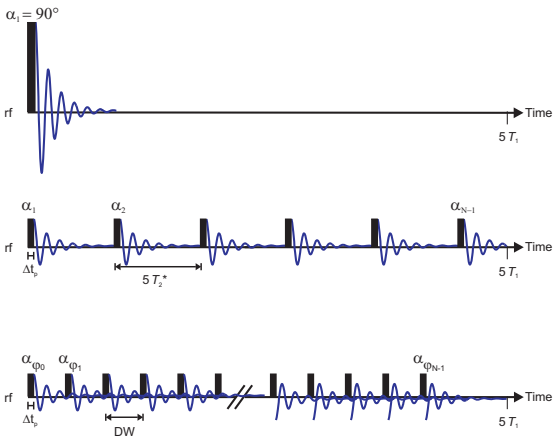

Figure 5.1.: Comparison of standard pulse sequence (top, center) and Frank (bottom) within the maximally available time $5 \cdot T_1$.

Finally, Fourier transformation yields

$$X(f_n) = m \exp\left\{-i\frac{2\pi}{m^2}(f_n \bmod m)\, f_n\right\}, \tag{5.5}$$

which is of constant absolute value m. Further details and a more formal derivation of the Frank sequence can be found in [Blümich 09; Fan 96].

According to linear system theory, the impulse response $y(t)$ is a convolution of the desired signal data $k(t)$ and the excitation function $x(t)$. By making use of the convolution theorem, the cross-correlation step can be executed in the frequency domain by multiplying the complex conjugate $X^*(f)$ with the response spectrum $Y(f)$ to obtain the spectrum directly [Blümich 00],

$$K(f) = \frac{Y(f)\,X^*(f)}{|X(f)|^2}. \tag{5.6}$$

Since for pure phase modulation, as in Frank NMR, this corresponds only to a special phase correction, deconvolution is not even necessary to obtain correct magnitude data.

5.2. SPREAD Slice Selection

In order to maintain the advantage of low-power excitation also in slice selection, which is essential for physiological MRI, an alternative to standard excitation needs to be employed. Conventionally, a clipped, sinc-shaped rf pulse ($\mathrm{sinc}(x) = \sin(x)/x$) is applied under a magnetic field gradient and transforms the longitudinal magnetization within a well-defined frequency band into detectable transverse magnetization (cf. section 2.3).

Alternatively, the fractions of longitudinal magnetization associated with frequencies outside the relevant slice can be pre-saturated before any non-selective excitation scheme is employed, e.g. Frank sequences, to make use of the remaining magnetization. This approach was first realized by the so-called DIGGER pulses (Discrete Isolation from Gradient Governed Elimination of Resonances) [Doddrell 86], for which an inverse Fourier transformation of the inverted frequency excitation profile leads to a narrow distribution of the amplitudes in the time domain. Another advantage of pre-saturating unnecessary magnetization is the fact that the saturating rf irradiation does not need to be phase coherent. The hereby gained degree of freedom can be used for a reduction of peak rf power: the SPREAD method (Selective Pulses with REduced Amplitude Distribution) is explained in detail in [Nilgens 96].

In Fig. 5.2, the idea of the construction and implementation of SPREAD pulses is reviewed: After choosing the slice width $\Delta\omega$, the remaining frequencies within the total band under investigation, $\Delta\Omega$, are assigned a random phase. Inverse Fourier Transformation (IFT) then yields the phase and amplitude of the rf pulse, which is optimized for minimum amplitude in the time domain. When applied in a preparation block that includes a slice selection gradient, any experiment can be performed afterwards, which will only detect magnetization from within the relevant slice. In the example given, the excitation is a single non-selective pulse for observation of an FID. Since usually one of these SPREAD pulses does not completely saturate unnecessary magnetization, several different pulses are applied in between successive scans. In order to avoid unwanted echo formation, these pulses should differ from each other in their phase and amplitude modulations.

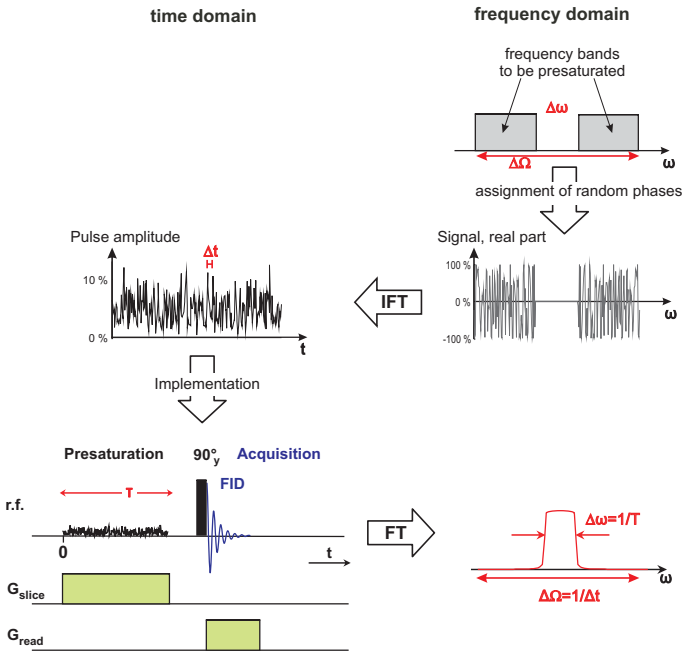

Figure 5.2.: Illustration of the construction of a SPREAD pulse and its implementation into a simple pulse program for slice selection by pre-saturation of longitudinal magnetization between successive scans. The SPREAD pulse is designed according to the desired profile shape and applied together with the selection gradient pulse. The signal is read out after a standard rf pulse and processed by Fourier transformation.

Chapter 6.

Experimentals - Frank NMR

6.1. Simulations

In order to gain deeper insight into the principles of Frank-sequence excitation, both simulations and experiments were performed. The simulations were based on calculations of the time evolution of the magnetization vectors as described by the Bloch equations [Bloch 46a]. The designated spectral shape was modeled by discretization of the relevant spectral bandwidth into a sufficiently high number of individual magnetization vectors with different resonance frequencies. For those vectors, transfer from longitudinal to transverse magnetization (and vice versa), precession and relaxation were calculated according to the variable parameters, e.g. rf pulse length, pulse amplitude, nutation frequency, T_1 and T_2 relaxation times, etc. Due to the linearity of the Fourier transformation, the resulting individual vector signals could be added in the time domain and processed like common NMR data.

6.2. Experimental Setup

All experiments were performed on a vertical-bore Bruker DSX 200 MHz spectrometer equipped with a Micro 2.5 gradient system with a maximum strength of 1 T/m using a standard 10 mm Bruker birdcage resonator (cf. Chapter 3). For general analysis of the Frank sequence in Chapter 7, the sample consisted of a 5 mm NMR tube filled with ($CuSO_4$-doped) water. By applying a conventional 90° hard pulse of 16 µs and recording the FID with 1024 complex points with a dwell time of $DW = 55$ µs, a spectral line with a width (FWHM) of 35 Hz and a T_1 relaxation time of 22 ms was recorded.

For imaging experiments (Chapter 8), standard 10 mm and 20 mm Bruker birdcage resonators were employed. Because image quality can more reliably be evaluated for

known samples, two different phantoms were assembled: the first (Fig. 6.1a) consisted of four small glass tubes of 3 mm inner diameter (ID), which were filled to different levels with $CuSO_4$-doped water with a spin-lattice relaxation time of $T_1 = 850$ ms to introduce image contrast. The second one was more complex (Fig. 6.1b). Two nested glass cylinders

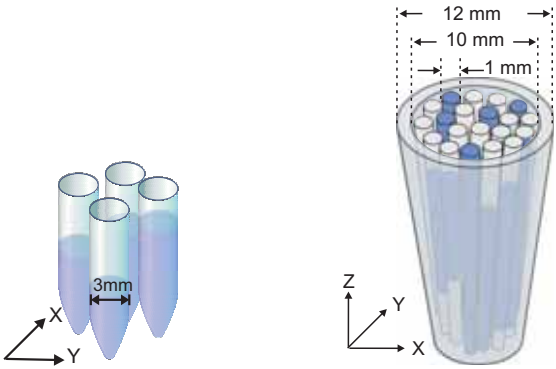

(a) Glass tube phantom (b) Capillary phantom

Figure 6.1.: (a) Imaging phantom consisting of four glass tubes of 3 mm ID, which were filled to different levels with $CuSO_4$-doped water. (b) Sketch of the capillary phantom, which consists of two nested glass cylinders with a fluid-filled gap of approx. 2 mm and 20 glass capillaries that were filled to different levels. The sample was again partially filled with $CuSO_4$-doped water.

produced a ring-shaped gap of approximately 2 mm which was completely filled with $CuSO_4$-doped water ($T_1 = 500$ ms). Inside the inner cylinder 20 glass capillaries with OD of 1 mm were placed, which again were filled to different levels with the same doped water.

6.3. NMR Methods

The Frank sequence was realized with the characteristic number $m = 32$, yielding a total number of $N = 1024$ pulses and thus an according number of acquired complex data points. All corresponding simulations were initialized with the same parameters.

Since linear Frank-sequence excitation does not give rise to echoes, only frequency encoding can be applied. Therefore, k-space needs to be sampled in other ways, e.g. radially or spirally. In this work, Filtered Backprojection (FBP) was employed, i.e. one-dimensional profiles are acquired along various spatial directions and the real image is

reconstructed by filtering and Radon-transforming the data set (cf. section 2.4) [Radon 17; Kak 88; Bracewell 95]. A scheme of the Frank FBP pulse sequence is demonstrated in Fig. 6.2. The FBP profiles were acquired in steps of 1° to cover the entire k-space with

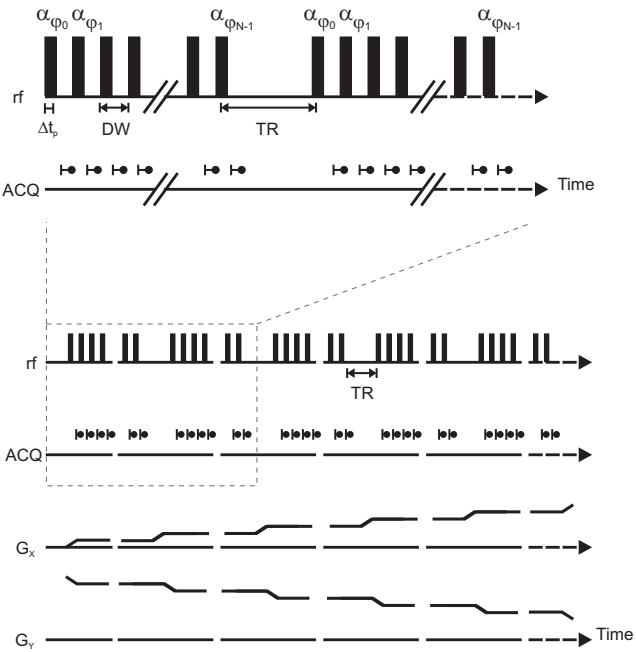

Figure 6.2.: Schematic drawing of a Frank excitation pulse sequence (top) integrated into radial imaging (bottom). The acquisition is interleaved with the N rf pulses. During each of the scans, a gradient is applied to encode the profiles needed for FBP.

sufficiently high resolution. Raw data was subjected to FFT and deconvolution and was filtered and Radon-transformed employing linear interpolation. The filter chosen for the images presented here was the so-called Hamming-filter, which is standard for FBP and is constructed from a ramp filter multiplied by a Hamming window to reduce noise sensitivity.

For low-power slice selection, the SPREAD technique was employed (cf. section 5.2). To avoid unwanted echo-formation, 20 different SPREAD pulses were designed according to the scheme shown before in Fig. 5.2. For selection of a 5 mm slice, each SPREAD pulse

was implemented with a length of 2560 µs defined by 256 points since the spectrometer requires a minimum time to process each point.

Chapter 7.

Analysis of Frank-Sequence NMR

In order to further analyze the Frank sequence, important characteristics were studied and quantified, including its sensitivity, excitation profile, and its steady-state behavior, as well as the effects of pulse length and amplitude.

7.1. Frequency Sweep Character

The most characteristic feature of the pulse sequence described in Eq. (5.4) can be understood by examining the phase in the complex plane of the rotating frame (Fig. 7.1). Within every time span $m\,\Delta t$, m pulses are applied, which describe a number of f_w turns in the complex plane ($-m/2+1 \leq f_\mathrm{w} < m/2$). Thus, every m pulses are expected to sequentially excite a frequency band in the spectrum by coherently flipping the respective magnetization onto the transverse plane. Consequently, the signals generated after each pulse within one package of m pulses interfere constructively within the respective frequency band. At the same time, magnetization from all other parts of the spectrum is to be excited incoherently leading to destructive interference. A way of demonstrating the effect of the individual Frank packages is to plot magnetization vectors in the Bloch sphere. The effect of the excitation Frank package of number $f_\mathrm{w}^\mathrm{exc}$ on the according detection resonance frequency, defined by $f_\mathrm{w}^\mathrm{det}$, is demonstrated in (Fig. 7.2) for $f_\mathrm{w}^\mathrm{exc} = f_\mathrm{w}^\mathrm{det}$. This model exactly reproduces the scheme of the excitation function in the complex plane, as shown in Fig. 7.1(b), demonstrating how the phase of the rf pulse follows the magnetization vector for coherent excitation.

By changing the order of the phases, the start, direction, and path of the sweep through the frequency domain can be chosen. These degrees of freedom can be explored, for example, for frequency-dependent signal weighting as well as frequency selective excitation in MR imaging. The following simulations and experiments were performed with a sweep

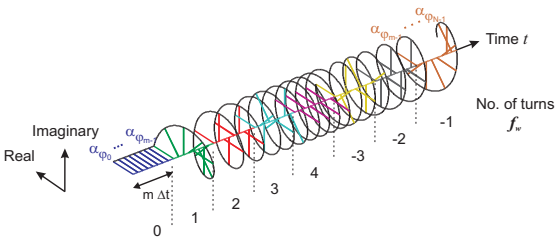

(a) Time domain

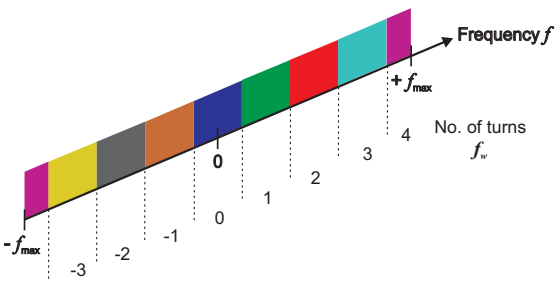

(b) Frequency domain

Figure 7.1.: Scheme of Frank-sequence excitation (a) in the complex plane of the time domain and (b) accordingly color-coded effect in the frequency domain. For clarity, the scheme shows a Frank sequence of only eight packages, i.e., $m = 8$ and thus the frequency intervals are counted by f_w as $-3 \leq f_w \leq 4$.

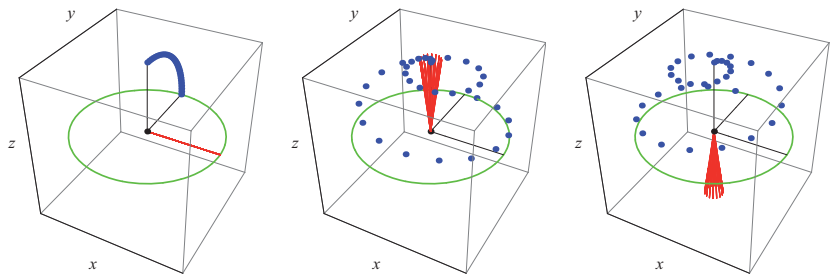

(a) $f_{\mathrm{w}}^{\mathrm{exc}} = f_{\mathrm{w}}^{\mathrm{det}} = 0$ (b) $f_{\mathrm{w}}^{\mathrm{exc}} = f_{\mathrm{w}}^{\mathrm{det}} = 2$ (c) $f_{\mathrm{w}}^{\mathrm{exc}} = f_{\mathrm{w}}^{\mathrm{det}} = -2$

Figure 7.2.: Bloch vectors demonstrating the on-resonant effect of various Frank packages, i.e., $f_{\mathrm{w}}^{\mathrm{exc}} = f_{\mathrm{w}}^{\mathrm{det}}$. Red lines depict the effective B_1 field, while the blue dots show the tip of the magnetization vector at every t_{w} time step within the investigated Frank package. While for $f_{\mathrm{w}} = 0$, the magnetization is directly flipped onto the x-y-plane, it describes two turns in opposite directions for $f_{\mathrm{w}} = \pm 2$.

from lower to higher frequencies.

For further analysis, the sequence consisting of a total of $N = m^2$ pulses was divided into its subunits of m wave packages, each consisting of m pulses (Fig. 7.3). As expected from the above discussion, each Frank package excites a frequency band shifted by f_{w} from the center resonance frequency. In every profile, a sinc-shaped amplitude modulation is observed which is caused by the step functions between the noise level and the points with constructively interfering signals. Due to the linearity of the excitation, the addition of individual signals should be consistent with the signal of the complete Frank sequence. The proof is given by the comparison of Fig. 7.3(c-e): the projections of the spectral data onto both dimensions (c,d) very nicely agree with the profile acquired within one normal Frank scan (f) regarding shape and amplitude. Since the projection onto the m-dimensional space of wave packages yields only 32 points instead of 1024 in the frequency dimension, the signal is 32 times higher. Also, summation of time data prior to the Fourier transformation does not alter the result.

Additionally, experiments were performed and compared with the simulations (Fig. 7.4). The required broad frequency distribution was experimentally realized by applying a magnetic field gradient along the axis of the cylindrical water sample. The results show very good agreement of simulated and experimental data when taking into account the excitation profile of the rf coil which leads to lower signals towards the edges.

Alternatively, the interactions of the Frank packages can be plotted with the Bloch

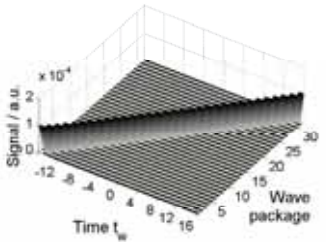

(a) Time data (magnitude)

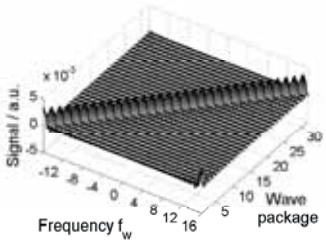

(b) Spectral data (real part)

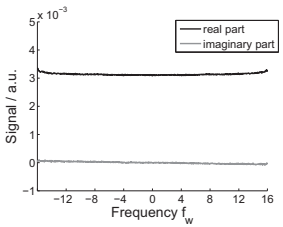

(c) Spectral data (real part) after projection of FT data onto 1st dimension

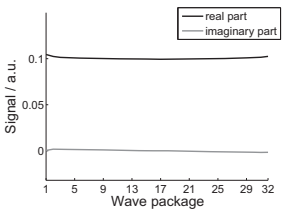

(d) Spectral data (real part) after projection of FT data onto 2nd dimension

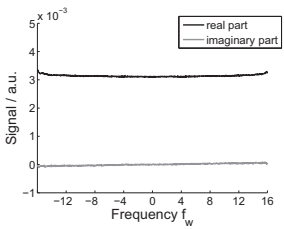

(e) Spectral data (real part) after summation of time data

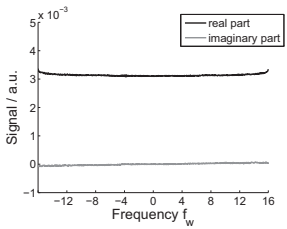

(f) Spectral data (real part) of one complete scan

Figure 7.3.: Simulation of individual Frank packages (a,b) and their further analysis by summation in both dimensions (c,d). In (e), the time data was added before the FT. In (f), the original Frank profile is shown, acquired within one complete scan. All images show the expected very good agreement.

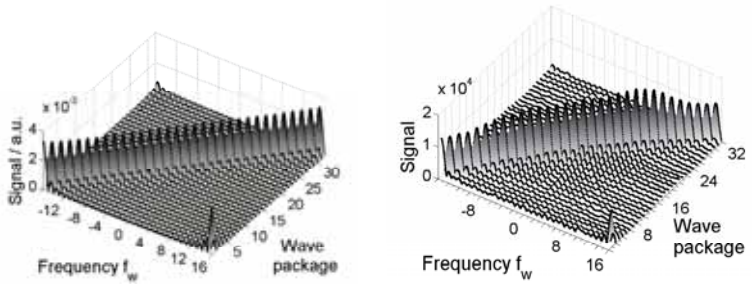

(a) Simulation (b) Experiment

Figure 7.4.: Simulation and experimental studies of rf excitation profiles by single Frank wave packages and their subsequent addition.

vectors again by now choosing different values for $f_{\mathrm{w}}^{\mathrm{exc}}$ and $f_{\mathrm{w}}^{\mathrm{det}}$ (Fig. 7.5). It can be seen from the amplitude of the angles by which the magnetization is tilted from equilibrium by the other packages, that there is a finite, varying signal from neighbouring packages. These interactions finally lead to the constructive and destructive interferences observed with the Frank sequence.

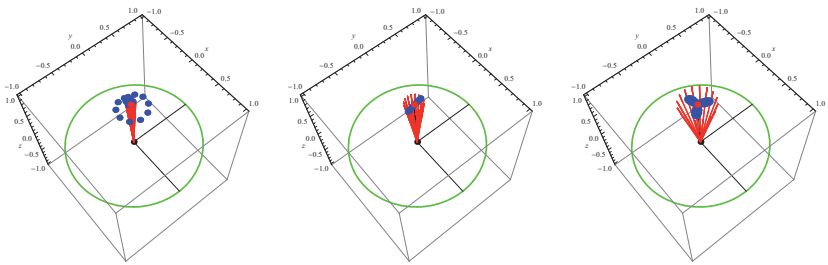

(a) $f_{\mathrm{w}}^{\mathrm{exc}} = 2$, $f_{\mathrm{w}}^{\mathrm{det}} = 4$ (b) $f_{\mathrm{w}}^{\mathrm{exc}} = -2$, $f_{\mathrm{w}}^{\mathrm{det}} = 2$ (c) $f_{\mathrm{w}}^{\mathrm{exc}} = -2$, $f_{\mathrm{w}}^{\mathrm{det}} = 1$

Figure 7.5.: Bloch vectors demonstrating the interaction of different Frank packages (for the case $m = 32$). As in Fig. 7.2, red lines depict the effective B_1 field, while the blue dots show the tip of the magnetization vector at every t_{w} time step.

7.2. Steady State Condition

Another characteristic of the Frank sequence is demonstrated in Fig. 7.6. If the pulse sequence is run once, those signals which have been excited by the first pulse packages are acquired during the entire Frank sequence of duration ACQ (depicted here as blue signal). However, signals with resonance frequencies that are reached later will be cut (red signal). This results in a frequency-dependent spectral resolution, which was proven by simulations of a fictitious spectrum consisting of seven equal lines (Fig. 7.7). In order

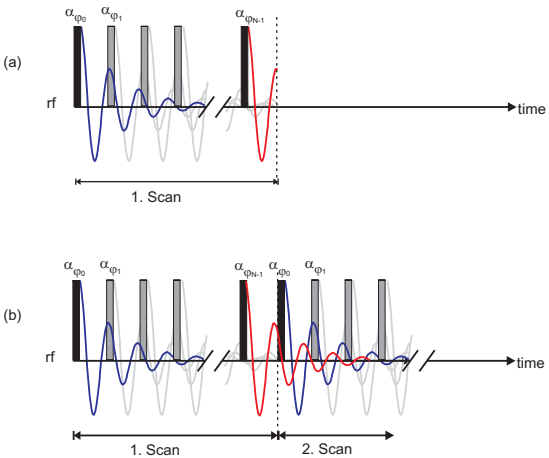

Figure 7.6.: Visualization of the steady state in Frank NMR: In (a), the red signal is cut. Thus, a second scan (b) is needed in order to acquire all signal components with the same weighting factor.

to avoid this effect, a steady state has to be obtained. In this case, running the sequence once before the acquisition like a dummy scan leads to a frequency-independent resolution. While for single-scan acquisition of NMR spectra this would lead to an increase in rf energy by another factor of two, for most imaging and spectroscopic applications this additional energy is negligible: It has already been shown in [Ziessow 74; Blümich 82] that even for radial k-space acquisition, the steady-state is well maintained, as long as the increment of the acquisition angles in k-space is small enough on the length-scale of the structures to be imaged. Similarly, this applies to NMR spectroscopy, for which the dynamics of the system under investigation needs to be slow compared to the time of one Frank scan.

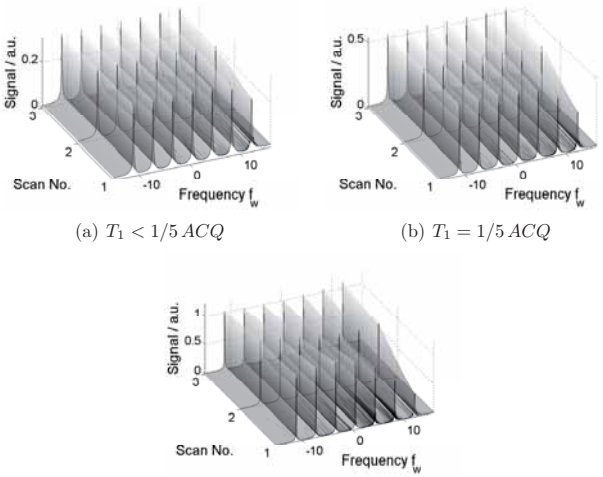

(a) $T_1 < 1/5\,ACQ$ (b) $T_1 = 1/5\,ACQ$

(c) $T_1 \gg 1/5\,ACQ$

Figure 7.7.: Simulated spectra with seven fictitious, equidistant peaks with originally equal amplitudes and widths after one, two, and three Frank scans for different T_1 relaxation times. After the first scan, a significant loss in spectral resolution with higher frequencies can be observed by broadening and lower amplitudes of the peaks. Already with the second scan, the spectrum reaches almost ideal shape.

7.3. Excitation Profile

The shape of the excited frequency profile is shown in the following to depend on both, pulse length and pulse amplitude. According calculations, simulations, and experiments were conducted.

7.3.1. Finite Pulse Length Effects

So far, as in [Blümich 09], the Frank sequence was only discussed and analyzed on discrete time and frequency grids, defined by Eq. (5.3) and (5.2), respectively. The excited frequency profile is then of constant absolute value m. However, in order to investigate the effect of finite pulse lengths Δt_p, it is now assumed that

$$p := \frac{\Delta t_\mathrm{p}}{\Delta t} \leq 1, \tag{7.1}$$

with $\Delta t = DW$ being the pulse spacing again. In [Blümich 09] a ratio of $p \leq 1/2$ was estimated to be favorable. For considering $p \leq 1$, the discrete Frank sequence has to be exchanged by a Frank function that is continuous in the time domain: $x : [0; m^2) \longrightarrow \mathbb{C}; t \longmapsto x(t)$. Computing the Fourier transform of this function, a further continuous function $X : [0; m^2) \longrightarrow \mathbb{C}$ will be obtained, of which finally the values on the discrete subset $\mathbb{Z}_{m^2}$ of $[0; m^2)$ are of interest. The detailed derivation can be found in Appendix A. The final expression for the absolute value of the Fourier transform of the excitation function is then given by

$$|X(f)| = m\,p \begin{cases} 1, & \text{if } f = 0, \\ \frac{|\sin(\frac{\pi f}{m^2} p[t])|}{\frac{\pi f}{m^2} p[t]} & \text{otherwise,} \end{cases} \tag{7.2}$$

where $[t]$ is the time unit of Δt and Δt_p needed to reconvert from dimensionless quantities to physical parameters. This gives the expected sinc-shaped profile, in which the ratio p between pulse length and pulse spacing influences the width of the excitation. As in standard NMR, the excitation profile becomes wider with decreasing pulse length.

The effect of finite pulses is also examined by simulations of the spectrum in Fig. 7.7 for varying pulse lengths Δt_p. They show that besides a first-order dephasing, the spectrum can be well reproduced for $p \leq 1/2$ (Fig. 7.8). Only the simulation with $p = 1$ shows a true signal depression at higher frequency offsets induced by the excitation profile of each individual pulse where the effective B_1-field is tilted by an angle that is not negligible

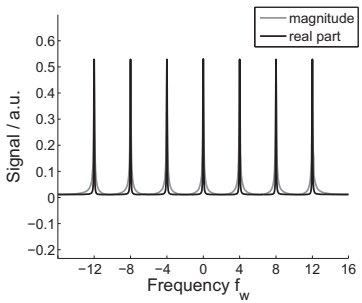

(a) $p < 1/2$

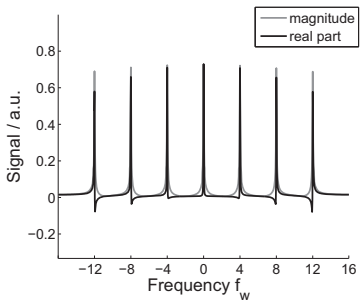

(b) $p = 1/2$

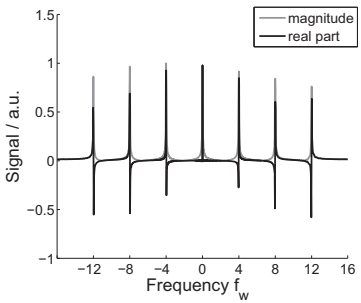

(c) $p = 1$

Figure 7.8.: Simulated spectra of the seven fictitious, equidistant peaks shown in Fig. 7.7 for varying pulse lengths Δt_p, and thus varying ratios p of pulse lengths Δt_p to dwell time Δt.

anymore.

For small enough α, the sine function can safely be approximated by

$$\sin(\alpha) \approx 1 - \frac{1}{6}\alpha^3. \tag{7.3}$$

This gives rise to further simplification in the expression for $|X(f)|$ in Eq. (7.2), namely

$$|X(f)| \approx mp\left(1 - \frac{\pi^2 f^2}{6m^4} p^2 [t]^2\right). \tag{7.4}$$

The consequence of keeping p small, say $p < 0.1$, i.e., the pulse length Δt_p is less than a tenth of the dwell time Δt, will then be that

$$0.98 \leq \frac{|X(f)|}{mp} \leq 1. \tag{7.5}$$

In the case $p < 1/2$, for which also a simulation has been shown above, the profile changes to

$$0.59 \leq \frac{|X(f)|}{mp} \leq 1. \tag{7.6}$$

Thus, if a maximum deviation of approximately 40% at the outer edges of the excited profile is considered acceptable, the pulse length can be set accordingly to one half of the dwell time.

7.3.2. Linear Excitation Limit

The rf pulse settings were further analyzed by simulating the excitation profiles with varying rf pulse peak powers at constant pulse lengths of Δt_p=1/40 Δt, i.e., $p \ll 1/2$ is always valid. When simulating the entire profile, the truncation of the excited signals from the outer edges leads to sinc-shaped distortions at those positions. Therefore, the simulated frequency distribution was limited here to one half of the total bandwidth for more clarity. In Fig. 7.9a, spectra were normalized to the average signal intensity in order to eliminate the effect of different flip angles and to simplify comparison of the spectral shape. Figure 7.9b shows corresponding experimental results.

For precise quantification of the non-linear effects observable at higher powers, the simulated profiles were processed in two different ways. First, in order to eliminate the deviations within the $m = 32$ frequency windows of the individual Frank packages, signals were averaged within these regions (Fig. 7.10a). An increasing asymmetry of the excitation profile over the frequency bandwidth with increasing rf peak power is then clearly

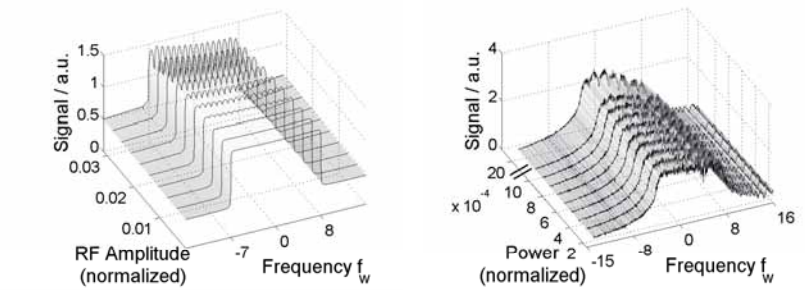

(a) Simulation (b) Experiment

Figure 7.9.: (a) Comparison of simulated Frank profiles with varying rf peak powers, here normalized to the rf pulse amplitude for which the 90° angle is reached, with the simulated pulse length Δt_{p}=1/40 Δt, i.e., $p \ll 1/2$. Thus, the settings yield flip angles for the entire wave package of $90°/1000 \leq m\,\alpha \leq 90°$ ($T_1 = T_2 = 1/5\,ACQ$). Original real amplitudes are normalized to the mean value of every spectrum to account for signal variations due to the varying flip angles. (b) According experimental results.

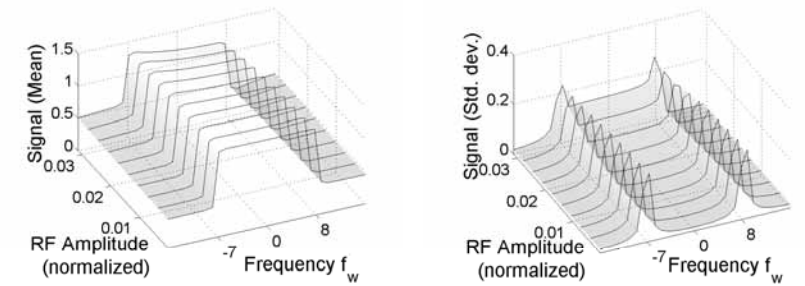

(a) Asymmetry of excitation (b) Non-white excitation pattern

Figure 7.10.: Effects of non-white excitation at increasing rf amplitude B_1 ($T_1 = T_2 = 1/5ACQ$). (a) shows the asymmetry of excitation across the frequency band by plotting the mean signal within every $m = 32$ frequency window of the Frank excitation. In (b), the standard deviation within every frequency window has been plotted for quantification of the excitation profile.

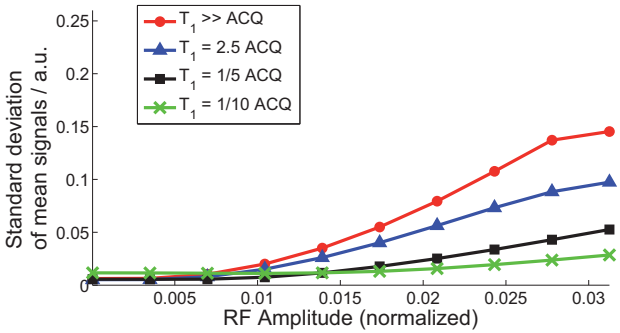

(a) Asymmetry of excitation

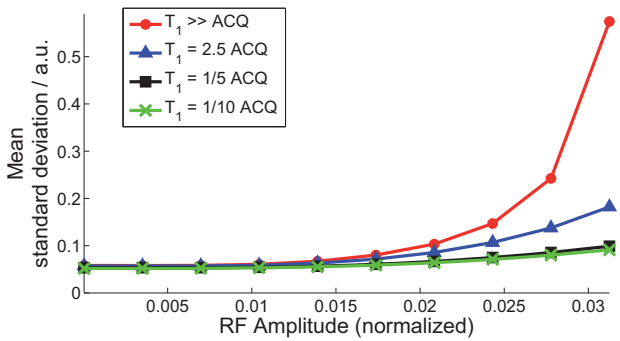

(b) Non-white excitation pattern

Figure 7.11.: Quantification of (a) asymmetry and (b) non-white excitation profile with increasing rf amplitude (B_1) for different relaxation times.

observable, even though the steady state is reached with the second scan (cf. section 7.2). Figure 7.11a demonstrates this effect quantitatively for various relaxation times by showing the standard deviations of the according average profiles. While all lines exhibit a basically sigmoidal shape, the effect of asymmetry becomes more prominent with increasing T_1 relaxation time. This is attributed to the fact that power is dissipated on longer time scales in spin systems with long relaxation times.

Secondly, the effect of non-white excitation patterns at high power levels was analyzed by calculating the standard deviations within every of the $m = 32$ frequency windows (Fig. 7.10b) and subsequent averaging (Fig. 7.11b). The amplitude of the non-white excitation pattern increases again with the pulse amplitude B_1 and relaxation time. While the dependence on the rf peak power appears to be exponential, no line fits were performed due to the lack of an analytic model.

In conclusion, the Frank sequence shows a white excitation profile for low enough power levels within the linear region of rf excitation. Due to the dependence of asymmetry and non-white profile on the relaxation times of the sample, one cannot give a simple limit for the pulse power without taking T_1 into account. However, generally using power levels of up to one 2500th of the power needed for one hard pulse can always be considered acceptable.

7.4. Sensitivity

For quantification of the actual savings in rf power and energy, the comparison of conventional and new methods has to request the same sensitivity. For a truly linear system and excitation that can be treated as conventional FT NMR, the comparison would yield in analogy to the derivation for the SWIFT technique in [Idiyatullin 06] :

$$\frac{SNR^{\mathrm{Frank}}}{SNR^{\mathrm{HP}}} = \sqrt{\frac{TR^{\mathrm{HP}}\, E_+^{\mathrm{HP}}\, E_-^{\mathrm{Frank}}}{TR^{\mathrm{Frank}}\, E_+^{\mathrm{Frank}}\, E_-^{\mathrm{HP}}}}, \tag{7.7}$$

with $E_\pm^i = 1 \pm \exp(-\frac{TR^i}{T_1})$, the scan repetition time TR, and $i \in \{HP, Frank\}$. Since for Frank excitation the minimum repetition time can be set to $TR^{\mathrm{Frank}} = TR^{\mathrm{HP}}$, as described in [Blümich 09] and in section 7.2, this expression would yield, for $T_1 \gg TR$, truly the same sensitivity for Frank and hard-pulse excitation, as compared to the loss of $\sqrt{2}$ estimated for SWIFT.

Alternatively, with $N = m^2$ pulses, the reduction of rf peak power achievable by spreading the power over the entire scan time can be approximated in the linear limit by com-

parison of the according power spectral densities, as briefly described in [Amor 11]. The spectral density $S_i(f)$ is defined as the absolute square of the Fourier transform of the excitation function $x_i(t)$,

$$S_i(f) = |\mathscr{F}\{x_i(t)\}|^2 = |X_i(f)|^2, \tag{7.8}$$

where $i = HP$ denotes the hard-pulse experiment and $i = Frank$ the new technique again. Assuming each pulse to last one time step $\Delta t_{\mathrm{p},90}$, one obtains for the conventional 90° pulse:

$$x_{90}(t) = B_{1,90}\,[\Theta(t) - \Theta(t - \Delta t_{\mathrm{p},90})], \tag{7.9}$$

where $B_{1,90}$ is the amplitude of the rf radiation and $\Theta(t)$ is the Heaviside step function. The Fourier transformation yields the desired spectral density function

$$S_{90}(f) = B_{1,90}^2 \frac{\sin^2(\Delta t_{\mathrm{p},90}\, f)}{f^2}. \tag{7.10}$$

The equivalent calculation for the Frank excitation yields together with Eq. (7.2),

$$S_{\mathrm{Frank}}(f) = B_{1,\mathrm{Frank}}^2\, m^2\, p^2 \frac{\sin^2(\frac{\pi\, p[t]}{m^2}\, f)}{\left(\frac{\pi\, p[t]}{m^2}\, f\right)^2}. \tag{7.11}$$

With $\Delta t_{\mathrm{p},90} = \frac{\pi\, p[t]}{m^2}$, the comparison yields the expected result that with $\Delta t_{\mathrm{p,Frank}} = \Delta t$, i.e., $p = 1$, for equal power spectral densities, it is required that

$$B_{1,90} = m\, B_{1,\mathrm{Frank}}. \tag{7.12}$$

Because $N = m^2$ pulses are applied, total rf energy cannot be saved by the Frank sequence. This result corrects an error in the original publication [Blümich 09], where a peak power savings of a fraction of m^4 was claimed, instead of a maximum of m^2. This feature is not particular for Frank sequences but applies to all time-extended forms of broad-band excitation.

However, these estimates are only valid for truly linear systems from which deviations are observable for high pulse lengths and powers (cf. section 7.3). Hence, the signal intensities of the conventional hard pulse and the new Frank-sequence excitation were again compared by simulations and experiments with varying pulse lengths and peak powers (Fig. 7.12).

For small flip angles ($\alpha < 90°/m$), the Frank sequence shows the same nutation behav-

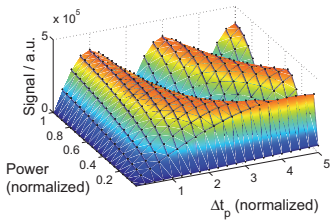

(a) Conventional excitation (simulation)

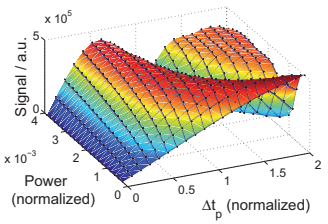

(b) Frank excitation (simulation)

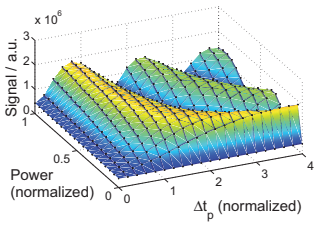

(c) Conventional excitation (experiment)

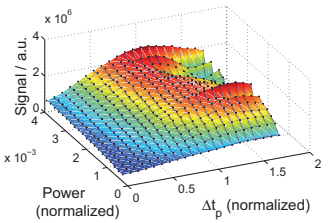

(d) Frank excitation (experiment)

Figure 7.12.: Comparison of sensitivity achieved by conventional hard-pulse excitation and by the new Frank-excitation method in simulations and experiments. Signal intensities depending on length and amplitude of the rf pulses are shown. For the Frank-sequence graphs (b, d), axes values apply to each individual of the $N = 1024$ total pulses.

ior as standard hard-pulse excitation, even though small deviations of the experimental results from the simulations can be observed due to rf turn-on characteristics, non-linear behavior of the rf amplifier, and voltage instabilities. For high flip angles, $\alpha > 90°/m$, the coherence condition for the addition of the signals from the various wave packages is not fulfilled anymore, and destructive interferences lead to a deviation from the expected two-dimensional sine-function.

The results prove that in order for the Frank sequence to yield maximum sensitivity, flip angles of 90° have to be chosen for every of the m wave packages, so no rf energy is saved compared to conventional excitation. Since signal points are acquired between all rf pulses, a signal amplitude is gained that is higher than in the standard experiment. An approximate total factor of

$$\sin\left(\frac{\pi}{2m}\right) \cdot \sum_{n=0}^{m-1} \cos^n\left(\frac{\pi}{2m}\right) \tag{7.13}$$

is determined quantifying the signal for the Frank sequence relative to the conventional signal, if longitudinal relaxation is neglected and total acquisition times are assumed equal, so the acquired noise levels are the same.

7.5. System Response for N$\rightarrow \infty$ and $N \rightarrow 1$ Pulses

If theoretically the number of pulses was to be increased to infinity, $N \rightarrow \infty$, the adverse effect of non-white profiles due to finite pulse lengths in the non-linear regime could be eliminated and the maximal reduction of rf peak power could be achieved. Besides reaching the limits of what can be implemented even in modern hardware, this would lead to maximal energy deposition, though, and the sequence would then result in continuous wave (CW) or rapid-scan NMR [Gupta 74; Dadok 74], depending on the time scale on which the sequence is performed: Even though the single Frank pulses become infinitesimally short and therefore each excites an infinitely broad spectral range, the interference of the resulting individual signals leads to an adiabatic frequency sweep with a signal response of only one δ-shaped frequency line at any given time in the scan. This corresponds to an excitation by a monochromatic continuous wave.

In general, there are two limits for the nuclear spin system, which apply to all NMR pulse sequences: For a small number of pulses, the final system response is dominated by the single-pulse excitation. For $N = 1$, i.e., standard FT NMR, the system response is simply the FT of the pulse shape. For very high numbers of pulses, $N \rightarrow \infty$, however,

groups of pulses which coherently excite certain parts of the spin ensemble govern the response and the single pulses become negligible. For Frank excitation, this means the group unit is one wave package consisting of m pulses and its response is the FT of a rectangle of length $m \cdot DW$. In conclusion, care has to be taken when a finite number of pulses is employed in multiple pulse sequences like Frank sequences or SWIFT because the real system response is a mixture of these two limits which has to be taken into consideration for analytical calculations of excitation profiles, sensitivity, MRI contrast, etc.

Chapter 8.

Magnetic Resonance Imaging with Frank Sequences

In order to analyze the feasibility of the Frank pulse sequence for MRI, images acquired using the novel excitation scheme were systematically compared to conventional images. The complexity of the MRI procedures was increased stepwise from two-dimensional MRI of one simple (Fig. 6.1a) and another more intricate phantom (Fig. 6.1a) over slice-selection up to three-dimensional MRI.

8.1. 2D MRI

A comparison of standard and Frank-sequence MRI was first made with 2D images of the simpler glass tube phantom (Fig. 8.1). Despite the reduction of rf power from 32 W to only 0.1 W and the enormous time savings, the Frank image exhibits equally high quality as the conventional SE image: in both images the regions of the water-filled tubes are well-distinguishable from the background and the contrast introduced by the varying filling degrees is clearly observable. Since the tubes could not be aligned perfectly, the projection images do not show exact circles, particularly for the top and the bottom tube. In the standard image (a), these regions appear to be blurred, while the backprojection image (b) represents slightly deformed edges. This effect has been found to be even more pronounced in a FBP image using standard excitation (Fig. 8.1c). Owing to the frequency sweep character of the Frank-sequence excitation, the recycle delay could be reduced from 2.5 s in the SE image to a minimum of only 100 ms for the Frank sequence. The short delay was set due to soft- and hardware requirements even though it leads to some loss in signal.

The same experiments were performed using the more complex phantom yielding the

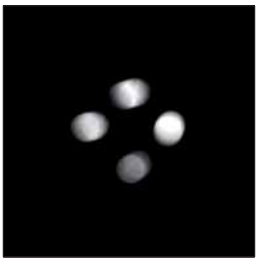

(a) Conventional excitation, SE

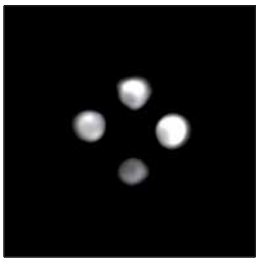

(b) Frank sequence, FBP

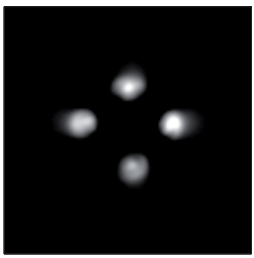

(c) Conventional excitation, FBP

Figure 8.1.: Two-dimensional projection images of the phantom depicted in Fig. 6.1a onto the transverse (XY) plane. FOV = $(32 \times 32)\,\mathrm{mm}^2$. (a) Original matrix size = $(256 \times 256)\,\mathrm{Px}^2$, 2-fold zero-filling, echo time $TE = 5\,\mathrm{ms}$, signal averaged over $NS = 8$ scans, repetition time $TR = 2.5\,\mathrm{s}$, total scan time = 85.47 min, SNR=1155. 256 rf pulses per scan of 25.9 µs at 32 W, flip angle = 90°. (b) Profiles in increments of 1°, FBP by linear interpolation and Hamming filtering, matrix size = $(1024 \times 1024)\,\mathrm{Px}^2$; $NS = 1$, $TR = 100\,\mathrm{ms}$, total scan time = 0.82 min, SNR = 337. 361×1024 rf pulses of 10.0 µs at only 0.1 W, flip angle = 2°. (c) Original matrix size = $(128 \times 128)\,\mathrm{Px}^2$; $NS = 8$, $TR = 2.5\,\mathrm{s}$, total scan time = 120.50 min, SNR=172 (real part of signal). 361 rf pulses per scan of 25.9 µs at 32 W, flip angle = 90°.

(a) Conventional excitation, SE (b) Frank sequence, FBP

Figure 8.2.: Two-dimensional MR projection images of the capillary phantom shown in Fig. 6.1b onto the transverse (XY) plane. (a) FOV=$(15 \times 15)\,\mathrm{mm}^2$, original matrix size = $(128 \times 64)\,\mathrm{Px}^2$, 4-fold zero-filling, $TE = 10\,\mathrm{ms}$, $NS = 16$, $TR = 3\,\mathrm{s}$, total scan time = 13.13 min, SNR = 904. 128 rf pulses per scan of 36 µs were employed at 32 W, flip angle = 90°. (b) Original FOV=$(21 \times 21)\,\mathrm{mm}^2$, original matrix size = $(1024 \times 1024)\,\mathrm{Px}^2$, $NS = 4$, $TR = 50\,\mathrm{ms}$, total scan time = 2.65 min, SNR = 6. 361 rf pulses per scan of 10 µs at only 0.1 W, flip angle = 2°.

results shown in Fig. 8.2. The Frank image principally reproduces intensities and shapes of the phantom very well. Contrast introduced by varying water levels is depicted correctly. The artifacts in the corners are due to the Hamming filter used in the backprojection procedure. In the center, noise leads to a ring-shaped artifact. The same effect has been observed later in a slice-selective FBP acquired with standard hard pulse excitation (Fig. 8.4c) and thereby has been proven to be independent of the Frank method itself. A constant colored noise peak outside the sample has been filtered during post-processing in order to avoid distortions introduced in the FBP. The ruffled edge of the outer ring is caused by partially non-white excitation, as the rf power of only 0.1 W still exceeded the limit for true linearity which is asked for in the Frank-sequence design. It was chosen that high to increase the effective flip angle and consequently, circumvent sensitivity losses. Thus, each of the $m = 32$ Frank packages becomes discriminable in the image. The repetition time was decreased again, so the total experiment time was reduced from 13.13 min to only 2.65 min. For equal SNR, numbers of averages, matrix sizes and FOV, a time saving of almost a factor of four was calculated.

8.2. Slice Selection

To measure 2D slice-selective images instead of 2D projections, the low-power SPREAD method was implemented and tested on a standard 10 mm NMR tube with an ID of 8 mm filled with $CuSO_4$-doped water. Figure 8.3 shows the direct comparison of sinc-excitation and the SPREAD technique by 1D images. The gray line marks the conventionally acquired complete 1D profile along the Z-axis, out of which slices of 6.25 mm were to be excited by sinc-shaped and SPREAD pulses. Side bands are excited by the finite and

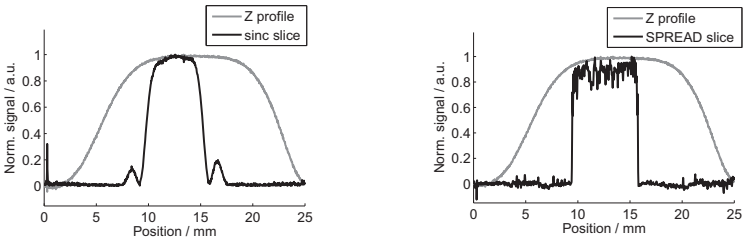

(a) Sinc slice selection

(b) SPREAD slice selection

Figure 8.3.: Comparison of conventional and SPREAD slice selection by comparing slices through one-dimensional profiles of the NMR tube (ID=8 mm) along the Z axis. FOV = 25 mm, matrix size= 1024 Px, slice thickness = 6.25 mm. (a) Sinc slice. One rf pulse for slice selection of 2000 µs at 32 W, flip angle = 90°. (b) SPREAD pre-saturation followed by conventional hard pulse. 20 SPREAD rf pulses of 2560 µs at only 0.3 W, followed by one rf pulse of 36 µs at 32 W, flip angle = 90°.

thus only approximately sinc-shaped pulse (Fig. 8.3a). The SPREAD pulse produced very sharp slice edges and very good signal saturation in the surrounding (Fig. 8.3b). However, unwanted echo formation by the series of SPREAD pulses led to an excitation pattern within the slice, which remained despite the application of varying pulse shapes. The use of SPREAD pulses allowed a reduction of rf power from 32 W to 0.3 W.

8.3. Slice-Selective 2D MRI

Finally, both low-power NMR techniques, Frank excitation and SPREAD, examined separately in sections 8.1 and 8.2 were combined to yield slice-selective two-dimensional images of the capillary phantom. Figure 8.4 illustrates again the comparison of conventional MRI, i.e., a sinc pulse SE image, and the new methods. The slice selection reduced the

(a) Conventional

(b) Low-power methods

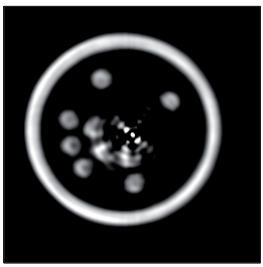

(c) Conventional excitation, SPREAD, FBP

Figure 8.4.: Slice-selective two-dimensional MR images of the capillary phantom shown in Fig. 6.1b onto the transverse (XY) plane. Slice thickness = 5 mm. (a) FOV = $(15 \times 15)\,\mathrm{mm}^2$, original matrix size = $(64 \times 64)\,\mathrm{Px}^2$, 4-fold zero-filling, $NS = 4$, $TR = 3\,\mathrm{s}$, total scan time = 13.03 min, SNR = 337. 64 rf excitation (90°) pulses per scan of 36 µs at 32 W and 64 refocusing pulses (180°) of 500 µs at 16 W. (b) Original FOV =$(21 \times 21)\,\mathrm{mm}^2$, matrix size = $(1024 \times 1024)\,\mathrm{Px}^2$, $NS = 4$, $TR = 50\,\mathrm{ms}$, total scan time = 5.12 min, SNR = 13. 361×20 SPREAD pulses per scan of 2560 µs at 0.3 W and 361×1024 Frank pulses (0.13°) of 10 µs at 0.16 W. (c) Original FOV =$(21 \times 21)\,\mathrm{mm}^2$, original matrix size = $(64 \times 64)\,\mathrm{Px}^2$, 4-fold zero-filling, $NS = 4$, $TR = 2\,\mathrm{s}$, total scan time = 48.43 min, SNR = 305. 361×20 SPREAD pulses per scan of 2560 µs at 0.3 W and 361 excitation (90°) pulses of 36 µs at 32 W and 361 refocusing pulses (180°) of 500 µs at 16 W.

SNR, so the difficulties with SPREAD, Frank excitation, and FBP discussed above add up and become more prominent. As demonstrated before in section 8.1, also the image employing conventional excitation but SPREAD slice selection and the FBP algorithm exhibits similar disadvantages and shows that those are not mainly caused by the Frank excitation. The most important features of the sample are reproduced. The outer ring shows a variation of the thickness which is caused by a dislocation of the inner glass tube from the center of the outer tube. As for previous images, rf power was reduced by several orders of magnitude and total scan time with the new low-power methods was less than half of the time needed for the conventionally acquired image.

A direct, quantitative comparison of all SNR values is difficult because identical acquisition conditions and spectrometer filters have to be assured. Also, the comparison requires the backprojection from cylindrical to Cartesian coordinates to employ identical filters. When using the SNR normalized to the pixel area A of the final image and to the square root of the total acquisition time $\sqrt{t_{\mathrm{acq}}}$, then for the slice selective images of Fig. 8.4, comparable values are obtained ($SNR^{\mathrm{SE}}/(A^{\mathrm{SE}}\sqrt{t_{\mathrm{acq}}^{\mathrm{SE}}}) = 2.7 \cdot 10^4\, Px^2/(mm^2\sqrt{min})$; $SNR^{\mathrm{FBP}}/(A^{\mathrm{FBP}}\sqrt{t_{\mathrm{acq}}^{\mathrm{FBP}}}) = 1.4 \cdot 10^4\, Px^2/(mm^2\sqrt{min})$).

Chapter 9.

Conclusions and Outlook

A detailed analysis of the most important characteristics of Frank-sequence excitation was presented. With regard to the sensitivity of Frank excitation, simulations and experiments consistently showed that every wave package applied excites spins within a certain bandwidth almost independently. For meeting the requirement of linear excitation for the Frank sequence, limits for pulse length and power were discussed. Since those limitations are easy to meet, it could be shown that Frank-sequence excitation is well-suited for excitation of a white profile over a broad spectral bandwidth.

Sensitivity considerations revealed that in order to achieve the same sensitivity as conventional 90° hard-pulse experiments, a factor of two more in rf energy has to be spent, if signal averaging is not applied to reach the steady state. An increase in signal intensity due to signal acquisition between the rf pulses resulting in a possible decrease of rf energy is given by Eq. (eq:FrankCos), yielding a factor of 0.6 in rf energy for typically $N = 1024$ pulses. Furthermore, it was shown that the expected reduction of peak rf power by $m^2 = N$ (typically order of 10^2 to 10^4) can be achieved. Generally, the upper limit of this number is only given by NMR spectrometer performance. Frank excitation constitutes optimal power savings due to pure phase modulation of the rf pulses. Additionally, ringing effects can be assumed constant throughout the sequence because constant flip angles are applied.

Moreover, it could be shown for the first time that Frank-sequence excitation allows for reduction of rf peak power in MRI by several orders of magnitude and of total acquisition time while maintaining image quality. Two-dimensional MRI was successfully performed and extended to slice-selective imaging routines employing a combination of the SPREAD and Frank schemes. The radial imaging scheme used for FBP enabled smooth gradient switching and thereby effectively reduced acoustic noise.

In conclusion, Frank-sequence excitation allows for miniaturization or even omission

of rf amplifiers which constitutes an essential basis for portable and miniaturized NMR. Even though the full potential of Frank excitation is somewhat compromised by sensitivity losses and limitations when performing the Frank sequence in the linear excitation regime, there may be special applications that depend on advantages like the free pathway through frequency space. Therefore, feasibility of Frank-sequence excitation for multi-dimensional NMR as well as generation of spin echoes to make use of the large number of very advanced and specialized echo-based NMR techniques will be explored in the future.

Although findings regarding rf-energy transmission do not support inherent reduction of SAR for medical MRI, Frank MRI greatly profits from the extension of total rf power over the acquisition time because peak rf power decreases in proportion to the number of time increments, which is equal to the number of rf pulses. Furthermore, the short dead times of Frank excitation allow for imaging of solids, which is unfeasible with standard echo-based methods [Amor 11]. In future applications, artifacts arising from the filtered backprojection algorithm can be avoided by referring to the more advanced method of *gridding* instead [Jackson 91]. For three-dimensional MRI, an encoding gradient can be used in addition to the 2D imaging scheme presented here. Because only Frank excitation is used then, maximal power reduction can be achieved. Also for slice selection, rf peak power and even total rf energy can further be reduced by application of separate wave packages of the Frank sequences instead of the SPREAD pre-saturation block. The Frank wave package, applied under a slice selection gradient, will only excite a defined section of the complete spectral bandwidth.

Part III.

Hyperpolarized ^{129}Xe

Chapter 10.

Introduction to Hyperpolarized ^{129}Xe NMR and MRI

Over the last decades, novel solutions to the problem of the rather low sensitivity of NMR compared to other spectroscopy and imaging techniques have been found. The signal is enhanced by several orders of magnitude through an increase of the spin polarization via *hyperpolarization*. Several methods have been developed for different NMR-active isotopes: *ParaHydrogen-Induced Polarization (PHIP)* exploits the higher spin order of hydrogen at low temperatures and transfers the hyperpolarization to the substrate of interest by catalytic reactions and by employing adequate polarization-transfer pulse sequences [Bowers 86; Natterer 97]. In *Dynamic Nuclear Polarization (DNP)*, electron polarization is raised usually in free radicals by irradiation of microwaves followed by electron-nuclear cross relaxation or spin-state mixing to yield a hyperpolarized nuclear spin system [Abragam 78].

Another principle for hyperpolarization of the noble gases ^{3}He[1] and ^{129}Xe is based on the work by Alfred Kastler and Marie-Anne Bouchiat in the 1950s and William Happer in the 80s [Kastler 50; Bouchiat 60; Happer 84]: in *Spin-Exchange Optical Pumping (SEOP)* electronic states of an alkali metal are optically pumped by irradiation of polarized laser light. Via hyperfine coupling during particle collisions, the hyperpolarization is then transferred to the ^{3}He or ^{129}Xe nuclei [Appelt 98; Appelt 04].

This part of the thesis focuses on applications of hyperpolarized (HP) ^{129}Xe in NMR and MRI, which offers a multitude of advantages over conventional ^{1}H NMR and has become a valuable tool in many fields of modern research, e.g. material analysis, monitoring of chemical reactions, and medical imaging [Goodson 02; Oros 04]. For most applications of HP ^{129}Xe, the atoms serve as very sensitive probes of their chemical and physical surround-

[1] ^{3}He can also be hyperpolarized by the method of Metastability Exchange Optical Pumping (MEOP) [Colegrove 63].

ings. Since ^{129}Xe is not naturally present in most samples, background-free measurements are possible. The large electron cloud is easily polarizable and yields a large chemical shift dispersion of more than 200 ppm in solution and up to several thousand ppm in rare solid compounds [Pietraß 95]. This together with the possibility of transferring polarization to other nuclei, the so-called *SPINOE (Spin Polarized Induced Nuclear Overhauser Effect)* makes ^{129}Xe NMR an interesting method of spectroscopy, e.g. surface NMR spectroscopy and solution NMR [Raftery 91; Navon 96; Appelt 01]. Many studies have also been conducted in the field of protein research as well as on polymers [Cherubini 03; Goodson 02]. Certain polymers have also been used as model systems of porous media to experimentally and theoretically investigate the interactions of ^{129}Xe with the surface, nanochannels, and the pores of the material [Moudrakovski 00; Jameson 02]. The exchange dynamics of the ^{129}Xe gas-polymer system have been analyzed in [Simonutti 06; Melian-Flaman 09; Utiu 12] by one- and two-dimensional spectroscopy.

Due to its sensitive chemical shift, ^{129}Xe is also favorable for molecular imaging by means of spectroscopic MRI. as demonstrated for example in [Han 04]. The use of HP ^{129}Xe for *in-vivo* MRI has first been demonstrated in 1994 in mouse lungs and hearts [Albert 94]. While gas-space imaging for analysis of lung ventilation has been shown to be feasible with HP ^{3}He as well, ^{129}Xe has the great advantage of being soluble due its lipophilic property. Thus, it crosses membrane barriers such as the brain-blood barrier [Swanson 97] or the lung-blood barrier, where it exchanges between alveoli and capillaries and partly dissolves in various tissues additionally allowing for MRI of lung perfusion and function [Driehuys 06; Driehuys 09; Imai 10]. Also advanced studies making use of selective saturation of one signal with subsequent exchange between the various signals observed in the ^{129}Xe spectrum (*HYPER-Chemical Exchange Saturation Transfer, HYPERCEST*), e.g. between HP ^{129}Xe in cryptophane cages with specific molecular linkers used as biosensors and their surroundings [Ruppert 00; Schröder 06; Ruppert 07], or the determination of apparent diffusion coefficients are feasible with HP ^{129}Xe MRI [Wakayama 08]. Also NMR of HP ^{129}Xe dissolved in blood has recently become an interesting field of research [Albert 95; Bifone 96; J. Wolber 99; Wolber 00b; Wolber 00a].

Furthermore, blood-dissolved HP ^{129}Xe MRI allows for investigation of blood flow dynamics and erythrocyte rheology in capillaries, which is of great importance not only because they are the major site of oxygen and nutrient exchange. Also, the proper microcirculatory function is primarily determined by the rheological behavior of red blood cells [Altman 71]. Moreover, many medical devices, e.g. dialyzers, blood pumps, and oxygenators, require a design that minimizes mechanical stress on blood. In such tech-

nical systems shear gradients are two to three orders higher than in a healthy human subject leading to significant blood damage. Typical stress situations occur, for example, at the outlet of blood pumps [Bludszuweit 94] or in and after mechanical heart valves [Giersiepen 90; Paul 00]. Thus, improvements of these setups rely on detailed knowledge of the internal flow behavior.

However, well-established optical methods can only be applied on model fluids due to the opaqueness of blood, while tests with blood can only be performed indirectly [Blackshear 87; Yeleswarapu 98]. Consequently, NMR as a direct and non-invasive tool is an ideal means of blood investigations and in particular HP ^{129}Xe can provide important molecular information due to the chemical shift difference, e.g. between ^{129}Xe in plasma and in blood cells. Additionally, ^{1}H NMR velocimetry techniques [Callaghan 93; Jeffrey 94] have been employed for flow investigations [Callaghan 93; Li 94]. A first comprehensive ^{1}H NMR study of capillary blood flow by Han et al. could reproduce non-Newtonian flow behavior of whole blood [Han 01].

Even though xenon provides good solubility even in aqueous solutions like blood, the efficient and bubble-free dissolution has been an obstacle for a long time for making use of HP ^{129}Xe in solution. Either the gas has been shaken into the solvent leading to undesirable foams or the gas has freely diffused into the carrier fluid, which is very inefficient. Recently, the use of dissolved HP ^{129}Xe has been enhanced by the so-called *xenonizer* setup, which mainly consists of hollow-fiber membranes like commercial blood oxygenators and dissolves HP ^{129}Xe continuously and bubble-free [Blümler 08; Baumer 06b]. In [Amor 09], the xenonizer has principally been proven to yield sufficient dissolution efficiency for different MRI experiments. The type of membrane material in commercial oxygenators has been shown to sometimes impede dissolution of anesthetic gases. Wiesenack has compared commercially available oxygenators with either polypropylene (PP) or polymethylpentene (PMP) fibers with respect to isoflurane insertion [Wiesenack 02]. A similar comparison of a commercial PP fiber with fibers of special composition has been performed by Catapano [Catapano 04]. These investigations have been extended to various narcotic gases including xenon [Philipp 02; Hoffmann 09].

In this part of the thesis, an investigation of different xenonizers and various biomedical applications of HP ^{129}Xe NMR and MRI are described. First, a theoretical background of the performed HP ^{129}Xe experiments (Chapter 11) and the necessary materials and methods are provided (Chapter 12). In Chapter 13, xenonizers are analyzed spectroscopically and by means of MRI and a detailed, systematical comparison of different hollow-fibers is presented. On the basis of these results, blood-gas exchange and porcine blood rheology

are studied in Chapter 14 by one- and two-dimensional HP ^{129}Xe NMR spectroscopy. Finally, conclusions and an outlook for future experiments and possible improvements are summarized in Chapter 15.

Chapter 11.

Theoretical Background

This chapter deals with the theory that is necessary to understand the experimental setup, results, and discussion of the hyperpolarized ^{129}Xe NMR and MRI investigations presented in this thesis. First, the process of hyperpolarization by means of spin-exchange optical pumping and relevant relaxation mechanisms are discussed. In section 11.2, important physical and chemical characteristics of ^{129}Xe are presented. Finally, section 11.3 gives a summary of relevant blood fundamentals including blood-gas exchange and blood rheology.

11.1. Hyperpolarized Gases

One of the major drawbacks of conventional NMR is the lack of sensitivity. As discussed in more detail in Chapter 1, the magnetization M being the source of the NMR signal depends linearly on the polarization P. Thus, signal enhancement can be achieved by increasing the polarization above thermal equilibrium, a process called *hyperpolarization* (HP). Figure 11.1 gives a graphical illustration of this state. Hyperpolarization of ^{129}Xe can be achieved by *Spin-Exchange Optical Pumping* (SEOP) [Happer 84]. By optical pumping of electron spins, followed by spin exchange with the nuclear spin, a high degree of polarization of up to $> 65\,\%$ can be achieved [Zook 02]. Since hyperpolarization constitutes a state of non-equilibrium, it relaxes back into the equilibrium state. Therefore, the most important relaxation mechanisms will also be discussed in this chapter. The physical and chemical properties that are relevant to the biomedical applications presented in this work will be pointed out in section 11.2.

11.1.1. Optical Pumping

The first step in SEOP is *Optical Pumping (OP)*, that Alfred Kastler developed in 1950 and for which he was awarded the Nobel Prize in 1966 [Kastler 50]. A detailed description of the theory can be found in [Walker 97] und [Appelt 98]. In the following, the fundamentals of the method of optical pumping will be explained.

The principle of optical pumping is based on the polarization transfer of circularly polarized laser light onto the electronic spin states of alkali atoms. In most cases, rubidium (Rb) is used for this purpose, the electronic term scheme of which is shown in Fig. 11.2. Due to a coupling of spin and orbital momentum of the electrons, a fine structure splitting of the energy levels is observable[1]. For spectroscopy, the symbolic specification of the levels as $n^{2S+1}L_J$ with main quantum number n, total spin quantum number S, and total orbital momentum L has prevailed [Haken 03]. Since Rb as an alkali metal has one valence electron, the ground state is the $5^2S_{1/2}$ level, while the two sublevels of the first excited state are described by $5^2P_{1/2}$ and $5^2P_{3/2}$. Those levels with total angular momentum of $J = L + S$ additionally split into $(2J + 1)$ *Zeeman levels* in a magnetic field B_0, which are characterized by means of the magnetic quantum number $m_J = J, J-1, \ldots, -J$. In this work, the *D1 transition* from the ground state $^2S_{1/2}$ into the state $2P_{1/2}$ is selectively excited by irradiation of right circularly polarized laser light, σ^+, with $\Delta m = +1$ and a wave length of 794.8 nm.

Via collisions of Rb atoms among each other (at 10 bar approximately one collision within 10 ps [Appelt 04]) the two excited states with $m = -1/2$ and $m = +1/2$ mix and then relax into the ground states $^2S_{1/2}$ with $m = -1/2$ and $m = +1/2$ with a probability

[1] The effect of a hyperfine splitting of the sublevels can be neglected due to dominating pressure broadening of the lines.

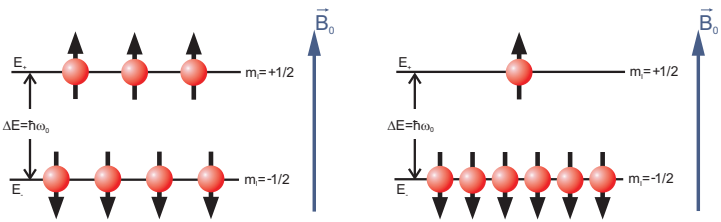

(a) Thermal ^{129}Xe polarization (b) *Hyperpolarized* ^{129}Xe

Figure 11.1.: Comparison of term schemes of (a) thermally polarized and (b) hyperpolarized ^{129}Xe.

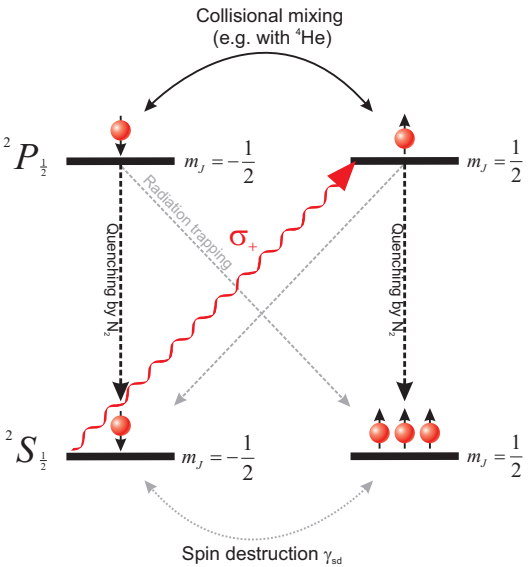

Figure 11.2.: Term scheme of the alkali metal rubidium in an applied magnetic field.

of 2/3 and 1/3, respectively [Chupp 87]. However, since the aim of OP is the accumulation in the state $^2S_{1/2}$ with $m = +1/2$ only, on average three photons are needed per atom for hyperpolarization. By admixing N_2, this ratio can be optimized to relaxation probabilities of 1/2 for either relaxation path.

The excited state typically has a lifetime of approximately 30 ns [Appelt 04] before it relaxes back to the ground state by emission of a photon that is again circularly polarized due to conservation of angular momentum. If this photon is left circularly polarized ($\Delta m = -1$) and it is absorbed by other alkali metals, the pumping process is disturbed. In order to prevent this effect of *radiation trapping*, a *quench gas* is admixed to the Rb vapor allowing for a radiation-free transition into the ground state, e.g. by conversion of the photon energy into rotational or vibrational energy of the quench gas molecules. Usually, the already added nitrogen serves this purposes effectively. At a partial pressure of about $0.35 - 0.40$ bar N_2, the lifetime of the excited state decreases from 30 ns to only 1 ns almost entirely suppressing radiation trapping (remaining probability of approx. $0.8 - 4\,\%$ [Wagshul 89]).

Because the transition that has to be pumped corresponds to a wave length of 794.8 nm, commercially available laser diode arrays can be employed. They suffer from a broad emission spectrum of $2 - 4$ nm, however. Consequently, the line width of the laser and the *natural line width* $\Delta\nu$ of the D1 transition of 5.7 MHz differ by several orders of magnitude [Wagshul 94]. As a consequence of the Heisenberg uncertainty principle, every resonance line with an average lifetime τ of the excited state has a natural line width $\Delta\nu$. Inelastic collisions can reduce the lifetime τ resulting in a further broadening of the line [Romalis 97],

$$\Delta\nu_\mathrm{p} = \frac{1}{2\pi\tau} \propto \sum_i \gamma_i P_i. \tag{11.1}$$

Here, γ_i is the *pressure broadening coefficient*, which is available only experimentally in most cases, and P_i denotes the partial pressure of the gas i.

Therefore, in order to make use of a larger fraction of the laser energy, the absorption line can be broadened up to 0.5 nm by increasing the pressure typically up to 7 bar. As a buffer gas, helium is used minimizing *spin destruction (sd)* of the built-up Rb polarization. The *spin destruction rate* $\gamma_\mathrm{sd} = \langle v\sigma_\mathrm{sd}\rangle$ is defined by the velocity-averaged expectation value of the cross section of collisions of two collision partners with velocity v [Appelt 98; Appelt 04],

$$\gamma_\mathrm{sd} = \gamma_\mathrm{SS}^{\mathrm{Rb-Rb}} + \gamma_\mathrm{NS}^{\mathrm{Rb-Xe}} + \gamma_\mathrm{NS}^{\mathrm{Rb-He/N_2}} + \gamma_\mathrm{vdW}. \tag{11.2}$$

The individual contributions arise from spin-rotational couplings of the Rb electron spins

Table 11.1.: Typical cross sections of processes destroying spin polarization (sd) and spin-conserving exchange processes (sx) [Appelt 98; Walker 97; Appelt 04].

Collison partners	Cross section
Rb-Rb	$\sigma(sx; Rb-Rb) = 2 \cdot 10^{-14} cm^2$
Rb-Rb	$\sigma(sd; Rb-Rb) = 1.6 \cdot 10^{-17} cm^2$
Rb-N_2	$\sigma(sd; Rb-N_2) = 1.2 \cdot 10^{-22} cm^2$
Rb-He	$\sigma(sd; Rb-He) = 9 \cdot 10^{-24} cm^2$
Rb-Xe	$\sigma(sx; Rb-Xe) = 1.5 \cdot 10^{-20} cm^2$

in Rb-Rb collisions ($\gamma_{\mathrm{SS}}^{\mathrm{Rb-Rb}}$), of the Rb electron and the total angular momentum in Rb-Xe ($\gamma_{\mathrm{NS}}^{\mathrm{Rb-Xe}}$) as well as in Rb-He and Rb-N_2 collisions ($\gamma_{\mathrm{NS}}^{\mathrm{Rb-He/N_2}}$), and from van-der Waals interactions (γ_{vdW}). Cross sections for the most important spin-exchange and spin-destruction process are given in Tab. 11.1.1. The total Rb polarization P_{Rb} can be described by

$$P_{\mathrm{Rb}} = \frac{s_z R + 2\gamma_{\mathrm{sx}} \langle K_z \rangle}{\gamma_{\mathrm{sd}} + R}, \tag{11.3}$$

where s_z is the z-component of the laser light polarization ($s_z = +1$ for σ_+-light), R is the optical pumping rate, $\langle K_z \rangle$ is the mean ^{129}Xe polarization, and γ_{sx} is the rate of spin exchange, which is further described in the following section.

11.1.2. Spin Exchange

A favorable type of transfer of the Rb spin-polarization is *spin exchange (sx)* between Rb electrons and the xenon nuclei via hyperfine coupling. The principle of spin exchange was discovered in 1960 by Marie-Anne Bouchiat and was proven 17 years later by Bruce C. Grover with ^{129}Xe ($P \leq 10\,\%$) [Bouchiat 60; Grover 78].

There are two mechanisms of spin transfer (Fig. 11.3): binary collisions of Rb and Xe atoms and the formation of *van der Waals (vdW) molecules* in three-particle collisions [Happer 84]. The exchange rate γ_{sx} for the spin exchange from Rb electrons to the xenon nucleus is given by [Driehuys 96],

$$\gamma_{\mathrm{sx}}(Xe-Rb) = [Rb] \cdot \left(\langle v\sigma_{\mathrm{sx}} \rangle + \frac{\kappa_{\mathrm{He}}}{[He]} \right), \tag{11.4}$$

where the spin-exchange rate for binary collisions, $\langle \sigma_{\mathrm{sx}}(v) \rangle$, takes values between $0.6 \cdot 10^{-16}\,\mathrm{cm^3 s^{-1}}$ and $3.7 \cdot 10^{-16}\,\mathrm{cm^3 s^{-1}}$ [Cates 92; Driehuys 96]. The analogon for the formation of vdW molecules is the constant $\kappa_{\mathrm{He}} = 1.7 \cdot 10^4\,\mathrm{s^{-1}}$ [Cates 92]. The terms in square

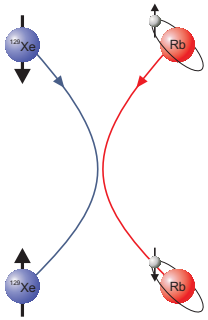

(a) Binary collisions

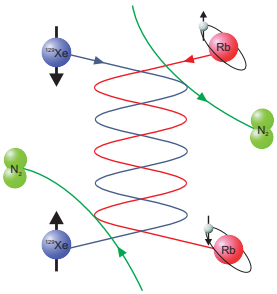

(b) Formation of van der Waals molecules

Figure 11.3.: Illustration of the mechanisms of spin exchange from Rb electrons to ^{129}Xe nuclei.

brackets in Eq. (11.4) denote the respective particle densities in amagat[2]. Which process is dominating thus depends on the gas pressure: at high pressures of several bars as used in this work, two-body collisions between Rb and ^{129}Xe dominate. The developing Rb-Xe complexes are very short-lived with lifetimes of approximately 1 ps. The lifetime of the vdW molecules is strongly gas pressure dependent, because they only exist until the next N_2 collision. Even at only 1.3 mbar, their lifetime is as short as 0.1 µs. Further details regarding these collisional processes can be found in [Happer 84; Appelt 98; Appelt 04]. Interactions at very low pressures (0.15 bar) have been discussed in [Imai 08]. Overall, due to additional translational degrees of freedom, the spin-exchange probability per Rb atom is about 0.07 [Driehuys 96].

In modern experiments, degrees of polarization of more than 65 % at very low xenon densities are achieved by re-circulating the gas mixture in the setup [Knagge 04], with extremely high laser powers [Zook 02] or with low gas pressures and counter-flow of the gas mixture with the laser light across a long optical pumping region in order to enhance spin exchange efficiencies [Ruset 06]. With the setup used in this work (cf. section 12.1.1), polarization degrees of up to 20 % can be achieved.

[2] 1 amagat ≅ particle density of a real gas under standard conditions ($p_0 = 1013$ mbar und $T = 273$ K)

11.1.3. Relaxation Mechanisms

The aim of hyperpolarization is reaching a non-equilibrium population of the ^{129}Xe nuclear spin levels. However, this polarization exponentially returns back to thermal equilibrium with the time constant T_1,

$$P(t) = P_0 \mathrm{e}^{-t/T_1}. \tag{11.5}$$

For HP gases, several processes i contribute to the relaxation rate $1/T_1$ of the noble gas:

$$\frac{1}{T_1^{\text{total}}} = \sum_i \frac{1}{T_1^i}. \tag{11.6}$$

For ^{129}Xe, as mentioned in Chapter 1, quadrupolar interactions or intra-molecular nuclear dipole fields can be neglected. Because it is monoatomical, only mechanisms are relevant that refer to interatomic dipolar interactions, strong van-der-Waals forces, collisions with surfaces, diffusion, and adsorption on solid materials [Schrobilgen 78]. The most important of these relaxation processes, including surface relaxation, oxygen-induced relaxation, dipolar and spin-rotational relaxation, as well as relaxation in magnetic gradient fields [Walker 97; Ruset 06], will be discussed in the following sections.

Collision-Induced Relaxation

Surface relaxation: One of the dominant relaxation effects is *surface relaxation*, i.e., decay of nuclear spin polarization by collisions of ^{129}Xe atoms with, for example, the walls of the glass pump cell (cf. section 12.1.1). During the collision, the xenon is ad- or absorbed and can relax by means of interactions with the glass surface. It is assumed that the polarization is lost only after several wall collisions [Baumer 06a]. For a cylindrical pump cell geometry as found in this work, the T_1 relaxation time increases with the square of the cell diameter [Fujiwara 01]. Consequently, cells with minimum surface-to-volume ratio S/V maintain the polarization for the longest period of time. According to [Driehuys 95], it is:

$$\frac{1}{T_1^{\text{surface}}} = \frac{1}{\eta}\frac{S}{V}. \tag{11.7}$$

The material-specific coefficient η is temperature as well as magnetic field dependent. A prolongation of the relaxation time can be achieved by special coatings of the pump cell that reduce contact with paramagnetic glass ingredients. Silicates like Surfasil^{TM} (Pierce Chemical Lab.), for example, have shown T_1 time increases of 15 % [Baumer 06a]. In [Rich 02], a T_1 time of even 840 h has been achieved using Rb coatings. Further

materials have been tested in [Breeze 99; Moudrakovski 01]. For HP ^{3}He, it could be shown that surface relaxation for alumino silicate glasses is dominated by ferro-magnetic impurities. By demagnetizing the pump cell, this effect has been reduced yielding average T_1 relaxation times of 150 h [Schmiedeskamp 06a; Schmiedeskamp 06b]. For ^{129}Xe in a silica cell, a T_1 time of 3 h has been measured.

Oxygen-induced Relaxation: The rate of *oxygen-induced relaxation* has been determined empirically by Jameson et al. for ^{129}Xe gas at room temperature for a partial pressure pO_2 of the paramagnetic oxygen [Jameson 88]:

$$\frac{1}{T_1^{O_2}} = \frac{pO_2}{2.80\,\mathrm{bar}}. \tag{11.8}$$

For example in air, a value of $T_1 \approx 13$ s has been obtained. The origin of this effect shortening T_1 by orders of magnitude is the dominant intermolecular dipole-dipole coupling of the ^{129}Xe nuclear spin and the O_2 electron spin [Pfeffer 95].

Relaxation through ^{129}Xe-^{129}Xe Collisions: Considering Xe-Xe collisions, two interactions have to be taken into account: dipolar and spin-rotational coupling. *Dipolar relaxation* decreases proportionally with the time between two collisions, which for gases typically is very long and can last up to several hours. Furthermore, dipolar coupling is a very short-ranged interaction because it decreases with the third power of the distance between the nuclei. Therefore, it is negligible under the conditions relevant in this work.

Nevertheless, this assumption does not apply for *relaxation by spin-rotational coupling (sr)* [Spiess 71]. During a ^{129}Xe-^{129}Xe collision, a van-der-Waals molecule can form, the angular momentum of which couples with the ^{129}Xe nuclear spin. According to the empirically derived relation by Chann et al. [Chann 02], the following relation holds true as long as the gas pressure does not reach very low levels and the magnetic field strength does not exceed several tens of tesla:

$$\frac{1}{T_1^{sr}} = \frac{1}{4.1\,\mathrm{h}}. \tag{11.9}$$

Relaxation through Magnetic Field Gradients

Another essential influence on relaxation is constituted by diffusion of the xenon spins within a magnetic gradient field. Any magnetic field inhomogeneities can be regarded as an additional transverse field $\vec{B}_\perp$ changing the orientation of the magnetic moments

[Cates 88]. The polarization then decreases due to induced spin flips depending on the diffusion constant $D = const./p$ or the pressure p as well as on the strength of the gradients $\nabla B_\perp$ in the main magnetic field B_0 [Schearer 65]:

$$\frac{1}{T_1^{\mathrm{Grad}}} = D\,\frac{|\nabla B_\perp|^2}{B_0^2} = \frac{const.}{p}\,\frac{|\nabla B_x|^2 + |\nabla B_y|^2}{B_0^2}. \tag{11.10}$$

This formula is only valid for high enough pressures and magnetic fields, though. For a container of radius r and a Larmor frequency $\omega_0 = \gamma B_0$, the condition $\omega_0 r^2/D >> 1$ has to be adhered to [Cates 88].

Relaxation through Chemical Shift Anisotropy

Additional relaxation terms have to be considered, if the shielding of the nucleus through the electron cloud is not symmetric and is not averaged by isotropic movements. This effect is known as *Chemical Shift Anisotropy (CSA)*. It is mainly found in solids, while in liquids it is magnetic field dependent [Spiess 71]. In [Moudrakovski 01], a dependence of the relaxation rate in xenon gas on the field at very high pressures has been observed in connection with CSA, but this effect is irrelevant for the gas pressures below 20 amagat employed here.

11.2. Physical and Chemical Properties of ^{129}Xe

In this chapter, the most important properties of pure gaseous xenon as well as of dissolved xenon are presented. First, general characteristics are described (section 11.2.1). Then, the solubility of xenon is discussed (section 11.2.2), before in section 11.2.3, the chemical shift properties are considered.

11.2.1. General Properties of Xenon

Xenon (from Greek: *xenos* = foreign, strange) is a mono-atomic noble gas constituting 0.087 ppm of the atmosphere. It is of atomic number 54, electron configuration [Kr] 4d105s25p6 and of atomic mass $A = (131.29 \pm 3)$. Nine stable isotopes[3] and two radioactive isotopes[4] are known. Those isotopes with highest natural abundance are ^{129}Xe (26, 44 %) und ^{131}Xe (21.29 %) [Römpp 99], the first of which can be enriched to

[3] $A = 124, 126, 128, 129, 130, 131, 132, 134, 136$
[4] $A = 127, 133$

up to 80 % (at very high costs). Xenon is unpolar and between the atoms, only week van-der-Waals interactions exist.

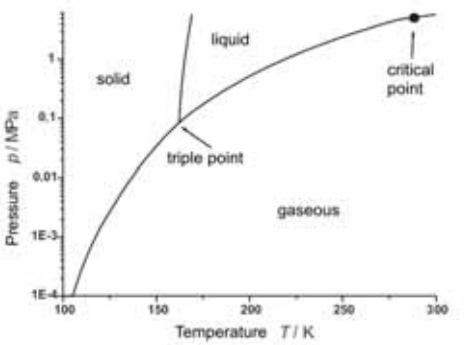

Figure 11.4.: Phase diagram of xenon with triple point at (161.3 K, 81.6 MPa) and critical point at (289.7 K, 5.83 MPa) [NIST 07].

In Fig. (11.4), the phase diagram of xenon is shown. Under standard conditions, xenon is gaseous. Due to the high boiling point at 165.1 K and 0.1 MPa and the melting point at 161 K and 0,1 MPa, xenon can easily be liquefied or frozen using liquid nitrogen (77.35 K). This allows for easy separation of xenon from gases like helium and nitrogen that have to be admixed in the process of hyperpolarization (cf. section 11.1). As a consequence of the closed outer electron shell, the chemical reactivity of xenon is very low. Oftentimes, it is therefore called "chemically inert", even though there are isolable compounds since xenon belongs to the most reactive noble gas. Especially with oxygen, fluorine, and nitrogen, bonds are possible [Bartlett 62; Hoppe 62]. Furthermore, the large and thus easily polarizable electron cloud causes the lipophilic character of xenon [Clever 79].

In medicine, xenon gas is used as an anesthetic, even though the exact mechanism of this effect has not been understood, yet. Since xenon does not build stable compounds in the human body [Lynch 00], its bio-distribution is well-known, and different pharmaco-kinetic models have been developed for the *in-vivo* uptake of HP ^{129}Xe [Peled 96; Martin 97], it is advantageous for physiological applications. As opposed to conventional contrast agents like Gd-DTPA (Gadolinium-diethylene-triamine Pentaacetic Acid), xenon can pass body membranes like the blood-brain barrier and the blood-gas barrier of the lung due to its lipophilic character and its small atomic diameter of 4.42 Å.

11.2.2. Solubility of Xenon

Because noble gases like xenon are uncharged, non-polar and hydrophobic, they provide a lower solubility in water making non-polar environments like lipids favorable. Therefore, xenon can ingress into phospholipid membranes as shown in [Baumer 06a]. The good solubility in lipids is also assumed a probable explanation for the anesthetic effect of xenon.

The solubility of xenon in blood and related exchange dynamics between different sites in whole blood are explained in section 11.3.1 after the introduction to blood fundamentals.

11.2.3. Chemical Shift of ^{129}Xe

The strong polarizability of the large electron cloud of ^{129}Xe does not only cause the lipophilic character, it also results in a high sensitivity for the chemical and physical environment. This results in a broad distribution of the chemical shift δ ranging from 0 ppm in gases to 300 ppm in solutions and even up to 7500 ppm in rare chemical compounds (Fig. 11.5). In comparison, typical shifts of the spectroscopically most relevant nuclei of ^{1}H and ^{13}C reach maximum values of 12 ppm and 250 ppm, respectively [Goodson 02]. As shown in Chapter 1, a reference is needed for quantification of the chemical shift. In

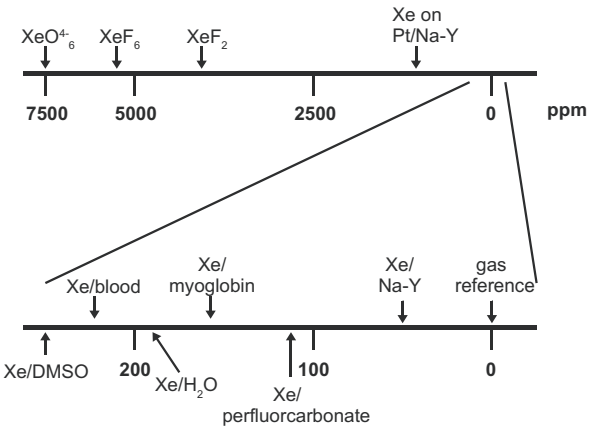

Figure 11.5.: Distribution of the chemical shift of ^{129}Xe in solution and in solids relative to free ^{129}Xe gas in infinite solution [Pietraß 95].

^{129}Xe NMR, sometimes $XeOF_4$ is used as a standard. Often, as in this work, the signal of the free ^{129}Xe gas at the current pressure or after extrapolation to zero density is used as an internal reference. According to literature [Jameson 73; Baumer 03], the chemical shift in the gas phase can be written in dependence on the xenon density ρ (in amagat) as:

$$\frac{\delta_{\text{gas}}}{ppm} = \sigma_1\rho + \sigma_2\rho^2 + \sigma_3\rho^3 + \sigma_4\rho^4 + \sigma_5\rho^5, \tag{11.11}$$

with

$$\sigma_1 = (+0.509 \pm 0,030)\,\frac{ppm}{amagat}, \tag{11.12}$$

$$\sigma_2 = (+0.989 \pm 0,050)\cdot 10^{-3}\,\frac{\text{ppm}}{\text{amagat}}, \tag{11.13}$$

$$\sigma_3 = (-0.178 \pm 0,015)\cdot 10^{-4}\,\frac{\text{ppm}}{\text{amagat}}, \tag{11.14}$$

$$\sigma_4 = (+0.653 \pm 0,010)\cdot 10^{-7}\,\frac{\text{ppm}}{\text{amagat}}, \tag{11.15}$$

$$\sigma_5 = (-0.700 \pm 0,010)\cdot 10^{-10}\,\frac{\text{ppm}}{\text{amagat}}. \tag{11.16}$$

Up to $30-40$ amagat, xenon behaves like an ideal gas, and up to 100 amagat (ca. 55 bar) first-order terms have to be taken into account in first approximation. Under typical conditions, a linear dependence of the chemical shift on the ^{129}Xe density is observable, which is mainly due to binary collisions between ^{129}Xe atoms. Only in regions of very high pressures, in which three-particle collisions become relevant, higher-order terms cannot be neglected, anymore.

For the chemical shift in solutions, a relation can be given when neglecting xenon-xenon interactions [Stengle 81]:

$$\delta_{\text{solution}} = \delta_{\text{A}} + \delta_{\text{iD}} + \delta_{\text{pD}} + \delta_{\text{dis}} + \delta_{\text{rep}}. \tag{11.17}$$

Here, the magnetic anisotropy (δ_{A}), the induced (δ_{iD}) and the permanent dipole of the solvent, as well as the dispersive (δ_{dis}) and repulsive (δ_{rep}) fractions of the van-der-Waals interactions between xenon and solvent have to be assumed. Thus, even though the relative contributions are unknown, every solvent shows a different ^{129}Xe chemical shift.

In human blood, ^{129}Xe NMR shows distinct chemical shifts of approximately 195 ppm for physically dissolved xenon in plasma and of 215 - 222 ppm for xenon in the red blood cells [Albert 95; Wolber 00a]. These resonances cannot be resolved by ^{1}H NMR due to fast exchange between the intra- and extracellular medium. For ^{129}Xe, a characteristic

exchange time of 12 ms [Bifone 96] has been determined, which is of the same order as that of water [Stanisz 98]. The distribution of chemical shifts for red blood cells is caused by a dependence on blood oxygenation. This effect is further elucidated in section 11.3.1.

11.3. Blood Fundamentals

Blood is one of the most important organs of the human body. Circulating through the blood vessels, it supplies all tissues with oxygen and nutrients, transports carbon dioxide and metabolites, and plays an important role in heat regulation and distribution of enzymes, hormones, etc. It consists of a carrier fluid, *plasma*, making up for 55% of the total blood volume and suspended corpuscular components. Plasma contains 90% water plus proteins, ions as well as above mentioned transported substances. Blood particles can be devided into *Red Blood Cells (RBCs)*, also called *erythrocytes*, white cells (*leukocytes*) and blood platelets (*thrombocytes*). Since erythrocytes account for 99% of the total blood particle volume and thus represent a total blood volume fraction, called *hematocrit (Hct)*, of 40-54%, they dominate blood flow behavior [Altman 71].

Human RBCs are acaryote, biconcave discs without an inner matrix and contain the oxygen carrying *Hemoglobin (Hb)* molecules (Fig. 11.6) [Deetjen 99]. The mean corpuscular volume (MCV) of porcine RBC amounts to $60\,\mu m^3$ [Altman 71]. In comparison to a sphere of equal volume, the surface is strongly enlarged enhancing gas exchange [Schmidt 95]. The typical lifetime of erythrocytes is approximately 120 days before they are degraded by physiological *hemolysis*, which mainly occurs as a consequence of changes in mechanical properties. For healthy erythrocytes, it is possible to pass capillaries with diameters smaller than their own in normal conditions. Besides the ability of the cell to deform, this behavior is enabled by a *tank tread*-like motion of the RBC membrane around its core causing circulation of the internal cytoplasm, which reduces the overall flow resistance. The rolling motion requires an extra-ordinary visco-elasticity of the membrane [Flieger 98].

11.3.1. Fundamentals of Blood-Gas Exchange

One of the most important functions of blood is the transport of oxygen because of its essential role in cell respiration. Physical dissolution of O_2 in blood plasma follows Henry's law,

$$c_{O_2}^{\text{Plasma}} = \alpha_{O_2}^{\text{Plasma}}\, pO_2, \tag{11.18}$$

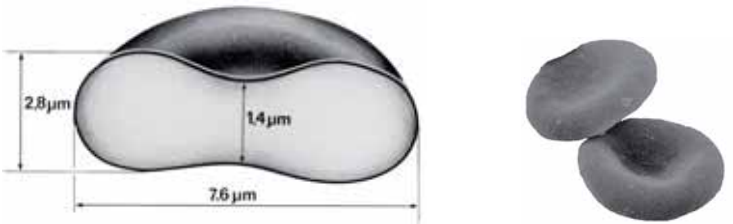

(a) (b)

Figure 11.6.: Human erythrocytes. (a) Schematic drawing of sectional view. (b) Scanning electron micrograph [Flieger 98; Deetjen 99]. Porcine RBCs are slightly smaller with a diameter of 6 µm [Altman 71].

with an O_2 solubility coefficient of $\alpha_{O_2}^{\text{Plasma}} = 3.67 \cdot 10^{-5}$ml O_2 ml^{-1} blood mmHg^{-1} O_2 [Cattaneo 06]. pO_2 denotes the partial oxygen pressure in the gas phase for a state of equilibrium with the solvent, and $c_{O_2}^{\text{Plasma}}$ is the resulting oxygen concentration. Most of the oxygen, however, is transported chemically bound to hemoglobin within the erythrocytes. Only 1 g of porcine hemoglobin binds 1.34 ml O_2 at a maximum oxygen saturation of $sO_2 = 100\%$ [Cummings 59],

$$c_{O_2}^{\text{Blood}} = 1.34\,\text{ml/g}\, c_{\text{Hb}}^{\text{Blood}}\, sO_2, \tag{11.19}$$

where the concentration of hemoglobin in porcine blood was set to a typical value of (12 ± 1) g/dl in this work (c.f. section 12.1.4). Since on average, every RBC contains $c_{\text{Hb}}^{\text{RBC}} = 2.15 \cdot 10^{-11}$ g/RBC [Altman 71], which is also called *mean corpuscular hemoglobin (MCH)* in medicine, this corresponds to a hematocrit of $Hct = 33.5\%$. The oxygen concentration and thus the oxygen saturation are not directly proportional to the partial pressure, but follow a more complicated relation, known as the *Hill equation*:

$$sO_2 = \frac{(pO_2/p_{50})^n}{1 + (pO_2/p_{50})^n}. \tag{11.20}$$

The value p_{50} describes the partial pressure at 50% oxygen saturation and has been experimentally determined to $p_{50} = (34.2 \pm 2.2)$ mmHg [Tweeddale 73]. The *Hill parameter* n specifies the oxygen affinity of hemoglobin and has been found to be approximately $n = 2.7$ for porcine hemoglobin [Tweeddale 73; Mockros 85; Willford 86; Cattaneo 06].

The oxygen saturation curve can be shifted by changing various blood parameters. An increase in total oxygen binding capacity n due to reduced pH (*root effect*) is not

seen in mammalian blood. Nevertheless, an increase of carbon dioxide concentration and the resulting decrease of pH leads to a reduction of oxygen affinity [Bohr 04]. For porcine blood, this *(fixed acid) Bohr effect* has been quantified with good agreement by Tweeddale and Willford et al. [Tweeddale 73; Willford 86]:

$$\frac{d \log pO_2}{d\mathrm{pH}} = -0.44 \pm 0.05. \tag{11.21}$$

While nitrogen is known to change blood pH, the solubilities of inert gases such as N_2 themselves have been shown to be independent of pH [Yamaguchi 93]. Even though Tweeddale reported almost no dependence of p_{50} on temperature, Willford found a small effect:

$$\frac{d \log pO_2}{dT} = 0.016/(1/K). \tag{11.22}$$

More complex interdependencies of blood gas concentrations, temperature, and pH can be found in [Siggaard-Ande 88] and are neglected here.

Kinetics of O_2 Exchange in Blood

The kinetics of O_2 transfer between the various sites in blood and the dependencies on pH and temperature, especially under stopped-flow conditions, have been investigated in detail by [Yamaguchi 87]. They divided the processes involved in O_2 transfer of RBCs which could limit the exchange rates into (1) chemical reaction of O_2 with hemoglobin, (2) diffusion across the RBC membrane, and (3) diffusion of O_2 in the extracellular medium and inside the RBC, as well as of hemoglobin within the RBC. The result was that the transfer was mainly limited by diffusion of O_2 and hemoglobin in the RBC interior and by diffusion of O_2 in plasma, and less by diffusion across the lipid cell membrane and by chemical reaction kinetics.

Explicitly, they considered that since for O_2 transfer of RBCs no significant changes with pH in the range between 7.1 and 7.7 were observed, (1) a predominant limitation by chemical reaction can be excluded even though the reaction velocity constants are expected to be sensitive to changes of pH. (2) Diffusion in the non-aqueous phase also was found to be negligible because the diffusive conductance, expected to be proportional to the O_2 solubility and to the O_2 diffusion coefficient, yielded no evidence for important limitation of O_2 transfer by the RBC membrane. For case (3), diffusion limitation in the aqueous phase, diffusion coefficients for O_2 in the extracellular plasma and within the RBCs, and that for hemoglobin within the RBCs were assumed to follow the temperature dependence of the viscosity of water and aqueous media. Resulting energy considerations

suggested a relatively more important role of Hb diffusion.

Under physiological conditions with active blood flow, little limitation of O_2 exchange by blood plasma is assumed. The main limitation is then expected to only be O_2 diffusion inside RBCs with some contribution by hemoglobin diffusion and Hb/O_2 reactions.

Gas Exchange via Hollow-Fiber Membranes

For medical applications, not only gas exchange within the various blood compartments is of great interest. Whenever the O_2 uptake and CO_2 release cannot be performed by the lungs anymore due to any pathologic lung condition, disease, or during lung surgery, an artificial gas exchange setup can provide a preliminary alternative. Commercial clinical oxygenators consist of hollow fibers with selective permeability for small molecules like O_2 and CO_2 gases. The fluid cannot pass the fiber walls.

There are different designs for hollow fibers, two very common of which are analyzed in this work. Purely porous fibers provide passage ways through which the gas has direct contact to the blood. In order to prevent blood flow onto the gas side, the fibers are made from hydrophobic materials. Nevertheless, plasma proteins can adsorb to the pores thereby increasing resistance to the gas flow and lowering the performance of the fibers [Meyns 05]. This process also leads to a reduction of the hydrophobic character of the material and finally to *plasma leakage* through the fiber walls. Homogeneous fibers without pores on the other hand only allow for diffusive gas passage, but have the advantage of reduced or even prevented plasma leakage [Niwa 04; Eash 04]. Recently, the two fiber structures have been combined. Asymmetric fibers mainly consist of porous materials with low gas flow resistance but are surrounded by a thin homogeneous skin layer to prevent protein adsorption [Matsuda 85; Mueller 00]. A disadvantage of the fibers described is their low resistance to elevated gas pressures. Even the dense skin layer of asymmetric fibers cannot prevent development of bubbles [Karichev 99]. If as in this work the gas pressure cannot be decreased, the blood pressure has to be adapted accordingly. Alternatively, a more robust membrane material has to be employed. In Chapters 12 and 13, medical silicone tubings are suggested and tested for this purpose.

The driving force for gas exchange via hollow fibers is a gas concentration gradient between the gas and the fluid side. The O_2 molecules have to diffuse through four areas from the interior of the hollow fiber, through the fiber pores, through a *diffusive membrane layer*, and within the blood to reach the RBCs for chemical binding to hemoglobin molecules. The different regions are often treated as serial resistors. Since the diffusive resistance within the blood usually is dominant, all other areas can be neglected

[Eash 04; Wickramasingh 02]. Thus at the outer fiber wall, a gas concentration step is considered which is related to the O_2 solubility in blood. At a specific distance from the membrane wall, the blood gas concentration asymptotically reaches equilibrium. The boundary layer with a gas concentration gradient into which gas diffusion takes place is the so-called *diffusive membrane layer*.

Since the blood flow velocity is very low, laminar flow conditions parallel to the fibers dominate. Perpendicularly, the gas diffuses to and from the membrane. Higher blood velocities, which usually do not occur in oxygenators, can induce turbulent flow at a certain distance from the fibers and consequently radial velocity components. The resulting mixing causes convective transport of dissolved or hemoglobin-bound gas and yields an almost homogeneous distribution of gas molecules outside the boundary layer. Flow patterns reducing the width of the diffusive membrane layer at constant gas concentration gradient therefore enhance gas exchange. Blood flow perpendicular to the fibers, known as *cross flow*, even yields a permanent change of flow direction and blood mixing. In contrast, stopped blood flow conditions as in this work lead to a very broad boundary layer and gas exchange is purely diffusive.

In order to quantitatively model gas exchange via hollow-fiber membranes, the mass transport of a number n of moles of the analyzed gas with a concentration c_l of liquid-dissolved gas through a membrane area A_m is considered [Cleveland 09]:

$$\frac{1}{A_\mathrm{m}}\frac{dn}{dt} = k\,(c_\mathrm{l,eq} - c_\mathrm{l}), \tag{11.23}$$

where $c_\mathrm{l,eq}$ denotes the dissolved gas concentration at equilibrium. The factor k is the *mass transport coefficient* and depends on geometrical and hydraulic parameters of the fiber module. With a constant liquid volume, that is

$$n = V_\mathrm{l}\,c_\mathrm{l};\ V_\mathrm{l} = const., \tag{11.24}$$

the solution of the differential equation becomes

$$c_\mathrm{l}(t) = c_\mathrm{l,eq} + (c_\mathrm{l,0} - c_\mathrm{l,eq})\,\left(1 - \exp\left\{-\frac{A_\mathrm{m}}{V_\mathrm{l}}\,k\,t\right\}\right), \tag{11.25}$$

where $c_\mathrm{l,0}$ is the initial dissolved gas concentration. Any interactions of molecules of different gases are neglected in this model. Conventionally, the mass transfer coefficient k

is expressed in terms of rheological parameters yielding a final expression [Cleveland 09]:

$$k = a \left(\frac{\epsilon_\mathrm{m}}{1-\epsilon_\mathrm{m}} d_0 \right)^{b-1} D_\mathrm{l}^{1-c} v^b \left(\frac{\rho}{\eta} \right)^{b-c}, \tag{11.26}$$

with a volume void fraction ϵ_m[5], an outer fiber diameter d_0, a diffusion coefficient of the dissolved gas D_l, and fluid velocity v. The parameters ρ and η are the density and the dynamic viscosity of the fluid, while a, b, and c are experimental constants.

Since blood-dissolved oxygen is available both physically dissolved in plasma and bound to hemoglobin, an effective diffusion coefficient $D_{\mathrm{O}_2}^{\mathrm{eff}}$ is introduced,

$$D_{\mathrm{O}_2}^{\mathrm{eff}} = D_{\mathrm{O}_2} \left(1 + \frac{d\, c_{\mathrm{O}_2}^{\mathrm{Hb}}}{d\, c_{\mathrm{O}_2}^{\mathrm{Blood}}} \right)^{-1}. \tag{11.27}$$

With Eq. (11.18)-(11.20), the effective diffusion coefficient and thus the mass transport coefficient show a complex dependency on partial O_2 pressure pO_2. Therefore, pO_2 is often considered the driving force in blood oxygenation.

Xenon in Blood

Various studies have been conducted to analyze the dependence of xenon solubility in blood on changes of blood parameters. In analogy to the independence of the solubility coefficients found for the inert gases nitrogen and argon by [Pelster 88] amending earlier reports on significant pH dependence of the Ostwald coefficient, no significant dependence of xenon solubility in blood on pH is assumed.

In [Chen 80], the Ostwald solubility coefficient $L_{\mathrm{Xe}}^{\mathrm{Blood}}$ of xenon in whole blood was found to be linearly dependent on the hematocrit. For the two major blood compartments, plasma and red blood cells, the following relations on temperature T were derived:

$$\log L_{\mathrm{Xe}}^{\mathrm{Plasma}} = -3.709 + 826.61/K \cdot 1/T, \tag{11.28}$$

$$\log L_{\mathrm{Xe}}^{\mathrm{RBC}} = -4.054 + 1080.41/K \cdot 1/T, \tag{11.29}$$

yielding $L_{\mathrm{Xe}}^{\mathrm{Plasma}} = 0.35$ and $L_{\mathrm{Xe}}^{\mathrm{RBC}} = 0.27$ at the physiological temperature of $T = 37°C$, and $L_{\mathrm{Xe}}^{\mathrm{Plasma}} = 0.41$ and $L_{\mathrm{Xe}}^{\mathrm{RBC}} = 0.43$ at $T = 20°C$ as used in this work (cf. section B.1). In contrast, [Ladefoged 67] reports values of $L_{\mathrm{Xe}}^{\mathrm{RBC}} = 0.17 \pm 0.008$ for oxygen-saturated blood and $L_{\mathrm{Xe}}^{\mathrm{RBC}} = 0.20 \pm 0.010$ for N_2-saturated blood under physiological conditions of

[5] Sometimes ϵ_m is also called *porosity*. This must not be confused with the porosity of the fiber material itself, however.

$T = 37°C$ and a pH of 7.4. While there is little agreement of absolute values of xenon solubility in erythrocytes in the literature, the difference in L_{Xe}^{RBC} for oxygenated and deoxygenated RBCs has been accepted and attributed to conformational changes of the hemoglobin molecule with varying O_2 saturation [Wolber 00a]. These changes also lead to the chemical shift difference between the observed plasma resonance which is insensitive to oxygenation and the resonance at oxygenated and deoxygenated RBCs of 20 - 27 ppm, respectively. The dependence on sO_2 is nonlinear following a sigmoidal shape with a more pronounced effect for higher oxygenation levels. Similarly, the T_1 relaxation time of ^{129}Xe in RBCs was found to depend on sO_2, with varying dependencies and absolute values in bulk blood samples and in blood foam [Wolber 00b; Tseng 97]. Wolber et al. report $T_1^{Plasma} \approx 9\,s$, $T_1^{RBC,N_2} \approx 3\,s$, $T_1^{RBC,O_2} \approx 6\,s$ for HP ^{129}Xe in plasma and RBCs equilibrated with N_2 and O_2, respectively. In Tseng et al., values $T_1^{Plasma} > 23\,s$, $T_1^{RBC,N_2} > 40\,s$, $T_1^{RBC,O_2} \approx 21\,s$ have been determined.

Other causes for the oxygenation depending ^{129}Xe solubility, chemical shift, and T_1 have been discussed and found less relevant than the change in affinity of hemoglobin for xenon. As both carbon monoxyhemoglobin and oxyhemoglobin are diamagnetic, whereas deoxyhemoglobin is paramagnetic [Pauling 36], bulk susceptibility effects inside the RBCs have been considered. Even though this effect is responsible for the 0.33 ppm ^{1}H shift [Playavin 83], it can only account for 0.25 ppm of the large ^{129}Xe shift [Ye 95]. Furthermore, the change in susceptibility is directly proportional to the concentration of paramagnetic deoxyhemoglobin and consequently should result in a linear dependence.

Interactions of xenon with hemoglobin also cannot account for the chemical shift difference. Large discrepancies between results from hemoglobin solutions and from whole blood can be observed [Tilton 82; Wolber 00a] suggesting that xenon interaction with hemoglobin is different in solution and in RBCs. Interactions of the complex hemoglobin molecule with dissolved gases are modulated by cofactors, which may influence the binding of xenon and therefore allow for access of hemoglobin sites that would not be accessible in solution. However, paramagnetic interactions with the Fe ion in hemoglobin alone cannot serve as the only explanation due to the nonlinear dependence of the chemical shift on the concentration of paramagnetic deoxyhemoglobin. This concept was supported by X-ray crystallographic studies that locate the only xenon binding site to hemoglobin far from the heme group [Schoenborn 65].

Thus, the variation of the chemical shift in whole blood is the result of an oxygenation-dependent hemoglobin affinity for xenon [Wolber 00a]. Conformational changes induced by oxygen binding [Perutz 70] can affect accessibility to the xenon binding sites and xenon

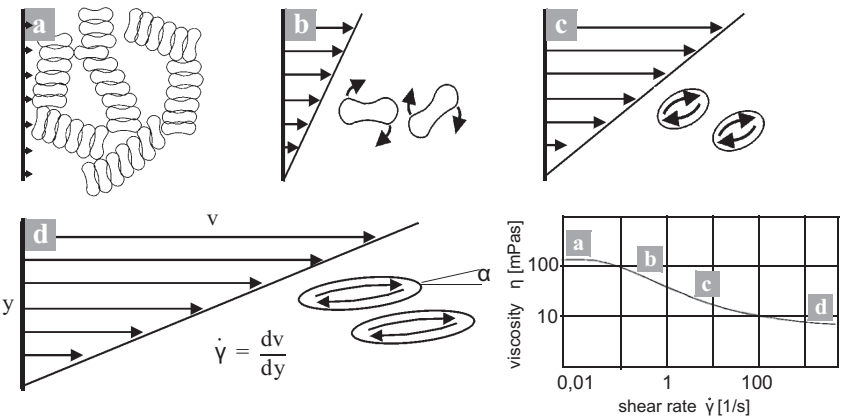

Figure 11.7.: Behavior of RBCs in flow field with increasing shear gradient dv/dy and resulting change in apparent viscosity [Klaus 04; Chmiel 73].

binding kinetics in globins [Tilton 86]. Oxygen therefore is assumed to act as an allosteric inhibitor for xenon binding to hemoglobin.

11.3.2. Blood Rheology

Usually, blood is treated as an isotropic continuum in fluid dynamics studies. Heterogeneities of relative velocities and resulting exchange of momentum between the different phases are approximated by pseudo-homogeneities with adapted parameters of apparent densities and apparent viscosities. Macroscopically, the apparent dynamic viscosity of whole blood depends on many variables, including shear velocity, temperature, hematocrit and the geometry and surface of the vessel, and thus cannot be considered a Newtonian fluid with constant viscosity. The dependence of the apparent dynamic viscosity (in the following only *viscosity*) on the shear velocity is strongly coupled to the aggregation and deformation behavior of erythrocytes leading to *shear thinning*, i.e., the viscosity *decreases* with increasing shear forces [Chmiel 73; Chien 70].

This observation is visualized in Fig. 11.7: at stagnant flow conditions (a), RBCs aggregate and present an elevated shear resistance, which is known as the *rouleaux effect*. With increasing shear rates, these aggregates dissolve and the viscosity declines [Fung 81]. While at low shear velocities, the cells maintain their original discoid shape and perform tumbling motions (b), they deform to a more ellipsoid shape at higher shear gradients (c)

and finally reach a cigar-shaped state (d). The elongated RBCs align along the direction of flow with a decreasing pitch angle α with increasing velocity, which is accompanied by tank-treading of the cell membrane and consequently by movement due to the *Magnus effect*. As long as the shear stress the erythrocyte is exposed to is low enough, the cell can return to the discoid shape. Otherwise, permanent and irreversible residual deformations remain.

Although plasma is considered a Newtonian fluid [Paul 03], cellular components cause a much more complex flow behavior [Blackshear 87], which is approximated by different models [Casson 59; Yeleswarapu 98; Paul 03; Quemada 78] that all assume Newtonian flow behavior for high flow rates, however. These models are only valid for certain shear velocities and particle volume fractions.

Moreover, deformation and migration behavior of flowing erythrocytes are of great importance for fluid dynamics and physiology. Since the membranes of RBCs exhibit visco-elastic deformability, only highly simplified substitutes or singular cells are examined for descriptions of cell flow [Fung 96]. Experiments on blood traumatizing mostly correlate shear stress of entire erythrocyte populations with according blood parameters [Giersiepen 90; Klaus 04; Paul 03; Blackshear 87]. Hereby, direct interactions of neighboring cells are neglected. Individual effects of blood flow have been demonstrated in simple geometries in the literature, two of which are tube flow and Couette flow.

Tube flow

In a tube of radius R, Newtonian fluids develop a parabolic velocity profile under laminar flow conditions, as demonstrated in Fig. 11.8. The shear rate $\dot{\gamma}$, for which generally

$$\dot{\gamma} \propto v/d, \tag{11.30}$$

with flow velocity v and characteristic length d, is valid, increases linearly from the center of the tube to the walls at $R = d/2$. The velocity is averaged by taking mean velocity across the tube diameter, $v = \bar{v}$. For quantification of all relevant flow parameters, the *Reynolds number* Re is defined,

$$Re = \frac{\rho v d}{\eta}, \tag{11.31}$$

where ρ is the fluid density.

For sufficiently small tube diameters ($R \leq 50\,\mu m$), effects of shear thinning can easily be induced. Another effect which has not been completely understood yet is cell migration in tube flow: the RBCs migrate towards the central axis of the tube [Pries 92; Barnes 95;

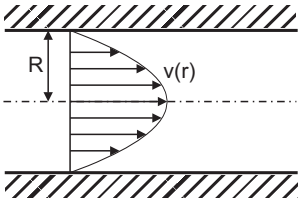

Figure 11.8.: Velocity profile of Newtonian tube flow.

Sharan 01]. Due to higher velocities in the center compared to the plasma-dominated outer regions, volumes with high cell concentrations leave the tube faster. Thus, the mean velocity of the cells exceeds the overall mean velocity, and the mean hematocrit within the tube is smaller than at the inlet. This effect is termed *Fåhraeus effect* [Fung 81; Skalak 87; Pries 92]. Consequently, the flow resistance and the mean viscosity of the blood flow decrease, which is known as the *Fåhraeus-Lindqvist effect*.

Couette Flow

Experimentally, simple tube flow is not always favorable because the fluid leaves the measurement region comparatively fast. An alternative is provided by *Couette systems*. They are composed of two nested concentric cylinders, the narrow gap between which contains the fluid under investigation. To induce flow, either the outer or the inner cylinder is rotating. The exposure time of the fluid to shear stress is controlled by the axial flow rate and, therefore, is independent of the stress loading. The velocity profile of a cylindrical Couette system is shown in Fig. 11.9. The shear rate $\dot{\gamma}$ is uniform and constant across the shear gap.

For the cylindrical Couette system, the Reynolds number is defined at the inner and the outer cylinder as

$$Re_i = \frac{\rho\, R_i\, \Omega_i}{\eta},\ i = inner, outer. \tag{11.32}$$

Further characteristics are the ratio of radii, the ratio of height and width of the shear gap, and the cylinder material.

With this setup, reproducible shear conditions in laminar flow can be exactly defined and blood damaging effects can be confined to the area within the shear gap. The shear stress is directly proportional to the rotational speed of the cylinder. A viscosity reduction of blood within the gap due to the Fåhraeus-Lindqvist effect is not observed [Paul 03].

Depending on the rotation speed, secondary flow patterns, e.g. Taylor vortices, can

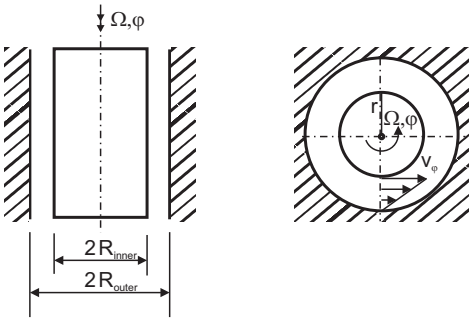

Figure 11.9.: Velocity flow profile in cylindrical Couette system.

occur. Due to destabilizing centrifugal forces, these effects develop faster in systems with internally driven cylinders than in systems with rotating outer cylinders. For $Re_{\text{outer}} = 0$, various flow types are passed with increasing rotation speed of the inner cylinder: first, Couette flow, then laminar flow with Taylor vortices, laminar flow with wave-shaped Taylor vortices, laminar flow with modulated Taylor vortices, and finally fully turbulent flow with vortices.

Chapter 12.

Experimentals - HP Xenon-129

12.1. Experimental Setup

For experiments with hyperpolarized ^{129}Xe, several fundamental setups were required: the hyperpolarizer increased the ^{129}Xe spin polarization above thermal equilibrium, while the so-called xenonizer provided a membrane module for continuous dissolution of the HP ^{129}Xe gas. For rheological investigations, according flow setups were designed and implemented. Important parameters of the porcine blood used in this work were adjusted to experimental needs and measured in order to monitor possible changes during the experiments.

12.1.1. The Hyperpolarizer

In Chapter 11, the physical process of hyperpolarization by means of spin-exchange optical pumping (SEOP) has been explained. The setup used for hyperpolarizing the ^{129}Xe spin system was a more compact and advanced version of those described in [Driehuys 96; Appelt 98; Shah 00; Appelt 04] and was built by Stephan Appelt at Research Center Jülich. A scheme and a picture of this setup are shown in Fig. 12.1 and 12.2, respectively. Its most important components, the laser system and the optical pumping unit, will be explained in the following.

Laser optical system

Optical pumping is based on the transfer of angular momentum from circularly polarized light onto rubidium (Rb) electrons (cf. section 11.1.1). The light is provided by two semiconducting diode lasers[1] with an optical unit for circular polarization. Each laser

[1] In most of the experiments, only one laser was available resulting in a loss of signal by approximately a factor of two.

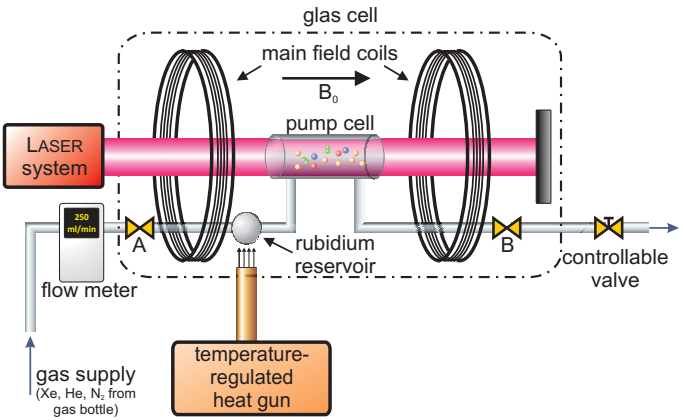

Figure 12.1.: Schematic drawing of the ^{129}Xe hyperpolarizer.

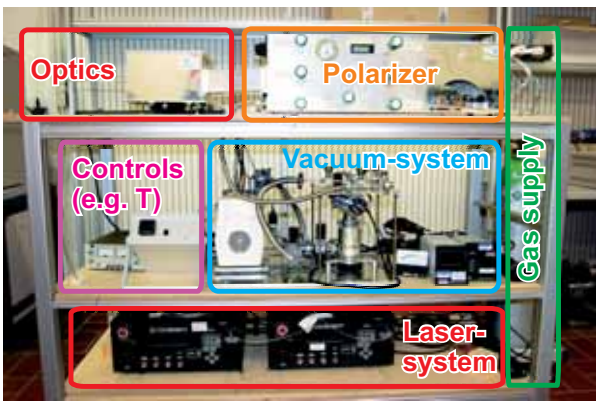

Figure 12.2.: Picture of the hyperpolarizer with various sub-systems.

consists of two fiber-optically coupled laser diodes (FAP, Fiber Array Packed; Coherent GmbH, Germany) resulting in a power of 60 W and a spectral line width of approximately 2.5 nm (FWHM). Via a glass fiber, the unpolarized laser light is led into the optical unit (Fig. 12.3). Here, the laser beam is split into two perpendicularly linearly polarized

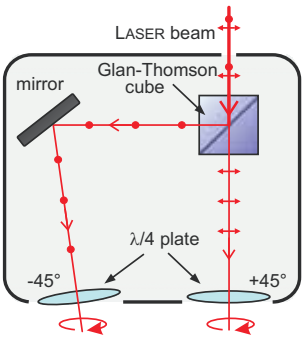

Figure 12.3.: Scheme of the optical unit for circular polarization.

beams of equal intensity by a Glan-Thompson cube. The beams are then transformed to right circularly polarized light ($\Delta m = +1$) by two $\lambda/4$-plates. The delay axes of these plates have to be adjusted to precisely 45° in order to prevent generation of elliptically polarized light with left circular components ($\Delta m = -1$) which would counteract the hyperpolarization process. Since the laser light is not completely absorbed by the Rb vapor, the transmitted light can principally be analyzed by an optical spectrometer in order to precisely calibrate the laser wave length and the heating temperature of the pump cell.

Optical Pumping Volume

The optical pumping (OP) system is placed inside an aluminum box in order to prevent stray light, to provide additional safety for the high-pressure pump cell, and to shield electromagnetic stray fields. In Fig. 12.1, a picture of the glass cell is shown. The gas mixture of 2% ^{129}Xe, 9% N_2, and 89% He at 2 bar above ambient pressure first flows at a rate of 170-200 ml/min through valve A and the heated Rb reservoir picking up the Rb vapor before reaching the pump cell and finally leaving the polarizer through valve B. Since for SEOP a magnetic field is needed, the pump cell is surrounded by four coils, similar to Helmholtz coils.

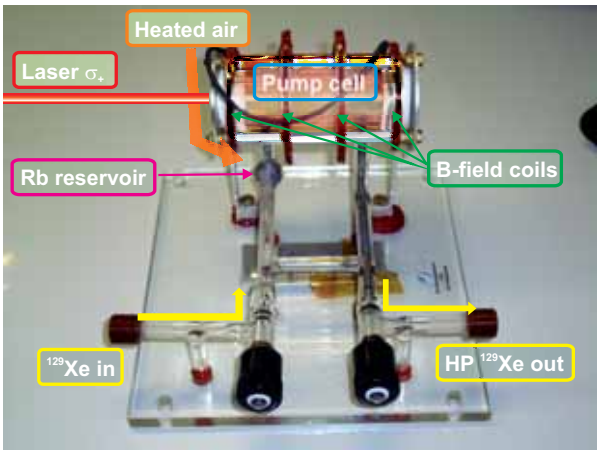

Figure 12.4.: Pump cell in which the hyperpolarization process takes place. The gas mixture enters through the left valve and picks up the heated Rb vapor. In the cylindrical cell, circularly polarized laser light polarizes first Rb-electrons, which requires a magnetic field, before ^{129}Xe nuclei are polarized via hyperfine coupling. The gas mixture with the HP ^{129}Xe finally leaves the glass cell through the right valve.

The pump cell is made of 5 mm thick borosilicate glass and provides a cylindrical geometry with an inner diameter of 24 mm and a length of 70 mm. In order to prevent lense effects, the window areas are manufactured as parallel as possible. The entire cell has been proven to resist pressures up to 15 bar. It is covered by a glass box in which by means of a regulated heat gun, temperatures of $160 - 200\,^{\circ}\mathrm{C}$ were reached. Previous analysis with optical spectrometers has shown that at the beginning of the hyperpolarization process, higher heating temperatures are needed in order to gain optimal Rb vapor densities [Mühlbauer 07]. However, after approximately $15 - 30$ min, laser irradiation has led itself to additional heating of the cell and the Rb reservoir resulting in a very high Rb density which prevents illumination of the entire pumping volume. At low temperatures ($\leq 160\,^{\circ}\mathrm{C}$), the Rb density is too low and the laser light is only partially absorbed. Thus, the optimal temperature depends on the amount of Rb and the necessary OP period. Values of $170 - 180\,^{\circ}\mathrm{C}$ have shown good results in this work. Finally, approximate degrees of polarization of up to 15%[2] could be achieved in this work.

12.1.2. The Xenonizer

Part of the central aims of this work were the detailed analysis and application of a hollow-fiber membrane system used to continuously dissolve HP ^{129}Xe into solvents, e.g. blood and its components [Baumer 06b; Blümler 08; Amor 09]. The system is also called *xenonizer*. Conventionally, a batch of HP ^{129}Xe is dissolved into the solvent by either shaking or by diffusion. The first method leads to bubbles resulting in susceptibility inhomogeneities within the sample. Additionally, especially in lipid emulsions which are often preferable due to the lipophilic character of xenon (cf. section 11.2.1), as well as in blood, very stable foams can build up. The waiting time for the decay of such foams often exceeds the relaxation time T_1 of the HP ^{129}Xe corresponding to a loss of signal. In the second approach, xenon freely diffuses into the solvent. This again is very time-consuming and therefore not an effective method for dissolution of HP gases [Zänker 07].

Consequently, a procedure for continuously delivering "fresh" hyperpolarized ^{129}Xe with minimal effect on the fluid is preferable. For surface NMR, experiments similar to the presented membrane-method have been realized [Haake 97; Brunner 98; Nossov 03]. In [Han 05], a system is reported providing dissolution of HP ^{129}Xe in microbubbles. In order to reduce inhomogeneities and therefore a loss of spectral resolution, the gas flow needs to be stopped, though. Therefore in the following, the *xenonizer* setup is described for continuous dissolution of HP ^{129}Xe.

[2] Due to the defect of one of the lasers, usually only approx. 7% could be reached.

Table 12.1.: Most important characteristics and setup parameters of the membrane types investigated.

Name	OXYPHAN®	CELGARD®	OXYPLUS®	Silclear®
Material	PP	PP	PMP	PDMS
OD	300 µm	300 µm	380 µm	635 µm
ID	200 µm	240 µm	200 µm	305 µm
Average Pore Size	0.03-0.04 µm	0.03 µm	none	none
Porosity	45%	40%	none, outer skin <1 µm	none
Active Fiber Surface, A_m	0.054 m²	0.037 m²	0.050 m²	0.031 m²
Active Fluid Volume, V_{Fluid}	4.86 ml	5.79 ml	4.31 ml	3.94 ml

OD: outer diameter, ID: inner diameter; PP: polypropylene, PMP: polymethylpentene, PDMS: polydimethylsiloxane

Hollow Fibers

For dissolution of hyperpolarized ^{129}Xe gas, a series of different fiber membrane materials was investigated in this work. Their main characteristics are summarized in Tab. 12.1. Scanning electron microscopy (SEM) images as well as the principal membrane mat weaving technology are shown in Fig. 12.5.

OXYPHAN® (Membrana GmbH, Wuppertal, Germany) is a hydrophobic polyolefin membrane featuring a homogeneous pore distribution. According to manufacturer information, this polypropylene (PP) membrane is stable against plasma leakage and in-break into the lumen of the hollow fibers despite its high porosity, because of its small pores (< 0.2 µm) and the large hydrophobic surface area. CELGARD® (Membrana GmbH, Wuppertal, Germany) is also a hydrophobic membrane made from PP. The mean pore diameter is declared to be 0.03 µm. In addition, CELGARD® exhibits a fairly high tensile and breaking strength according to manufacturer information. Like the two previous fibers, OXYPLUS® is a hydrophobic polyolefin hollow-fiber membrane but with an asymmetric structure. The highly porous polymethylpentene (PMP) membrane wall is surrounded by a dense PMP layer (<1 µm), which classifies it as a diffusion membrane. Another material has been included in the investigations in order to provide improved

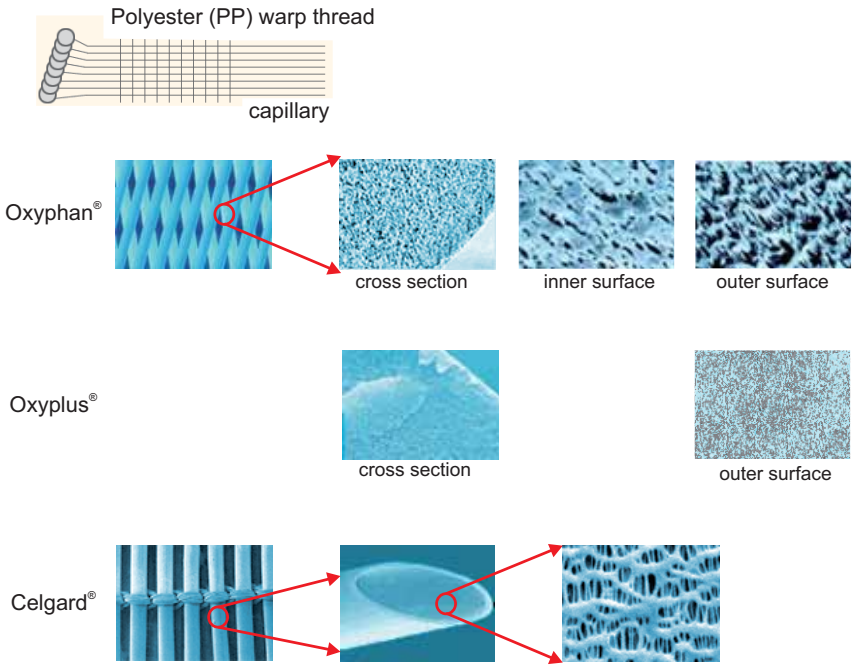

Figure 12.5.: Weaving technology and Scanning Electron Microscopy (SEM) images of the fibers (source: Membrana GmbH).

pressure stability: Silclear consists of a very dense polydimethylsiloxane (PDMS) membrane wall. This fiber material is a translucent silicone rubber material for medical tubing and offers very good mechanical properties.

For a comparative study, four identically constructed xenonizer housings were assembled at the Helmholtz Institute of RWTH Aachen University, each with one of the fiber types [Hamilton 12]. The polyolefin membranes were supplied in mats by the manufacturer and were spooled to membrane modules, which were potted into the housing. The membrane fibers exhibit different outer diameters and the mats have varying spaces between each fiber. Thus, the membrane surface area which participated in the gas transfer varied with membrane type. The theoretically involved areas were calculated to $0.054\,\mathrm{m}^2$ for OXYPHAN®, $0.037\,\mathrm{m}^2$ for CELGARD®, and $0.050\,\mathrm{m}^2$ for OXYPLUS®. The Silclear membrane was available in single fiber-form only. The fibers therefore had to be inserted individually by hand, yielding a theoretically active surface area of $0.031\,\mathrm{m}^2$.

The Complete Xenonizer Systems

For the purpose-built xenonizer used in this work, hollow fibers were embedded with silicone into a PMMA (polymethylmethacrylate) housing that essentially maintained the hyperpolarization and was customized to fit into the birdcage resonator. Figure 12.6 shows a sectional view of this setup indicating the gas and fluid flow directions: the gas mixture flows into the module through the luminal side of the hollow-fiber membranes. After leaving the membranes, the gas flows around the fiber housing back to the hyperpolarizer. Fluid inflow takes place in the axial center of the fiber module, leaving the module via an outer fluid cumulative ring. Thus, the liquid is forced to cross-flow through the fiber membrane module, ensuring that the entire fiber module participates in the gas transfer. This minimizes shunt flows between in- and outflow and avoids stagnation areas, which reduce the effective gas exchange surface and always hold thrombotic risks. Furthermore, in case of the polyolefin membranes (cf. section 12.1.2), the cross-laying of the membrane mats by an angle of 20° lead to greater mixed flow areas and to a more homogeneous distribution of dissolved gas. The xenonizer can be operated either following the principle of countervailing influence, as described above, or with parallel flow.

After connecting the xenonizer module to the gas in- and outlets of the hyperpolarizer, the pressure on the fluid was adapted to the excess pressure of the gas mixture in order to avoid bubbles due to the expansion of the fluid tubings. Whenever required, an active liquid flow could be applied by a magnetically driven rotary blood pump (Deltastream®, Medos Medizintechnik GmbH, Stolberg, Germany), which is characterized by high dy-

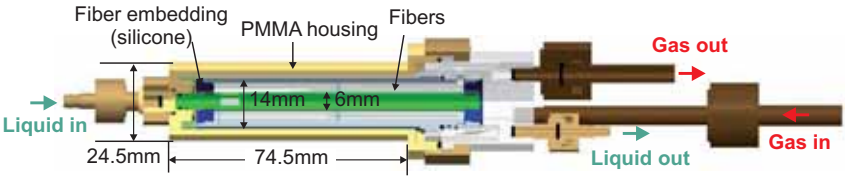

Figure 12.6.: Draft of the xenonizer setup [Hamilton 12]. The gas flows through the hollow fibers and is dissolved into the counter-flowing fluid. Undesirable effects as development of bubbles or stagnation areas can be avoided.

namic performance at low blood damage. The principal setup including the xenonizer module is shown in Fig. 12.7.

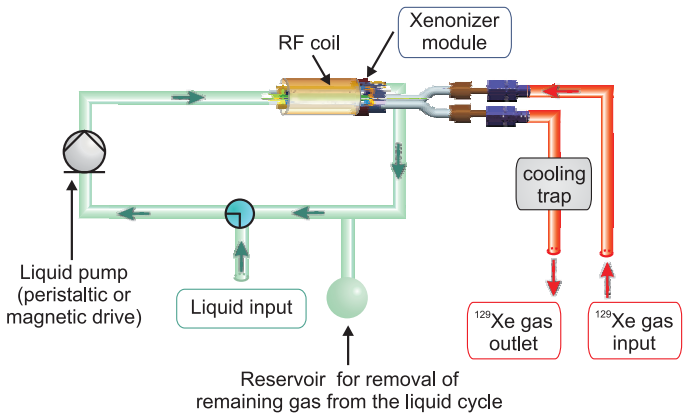

Figure 12.7.: Schematic drawing of the setup used for experiments on the xenonizer.

12.1.3. Setups for Blood Flow Investigations

Capillary Setup

While the principal setup used to analyze blood flow in capillaries is similar to the general setup demonstrated before, the fluid is now contained in two pressurized bags for fresh delivery (Fig. 12.8). Furthermore, the xenonizer is integrated before the resonator to allow placement of the capillary within the measurement area. The capillaries used in this work were made from PEEK (polyetheretherketone) with an inner diameter (ID) of 750 µm.

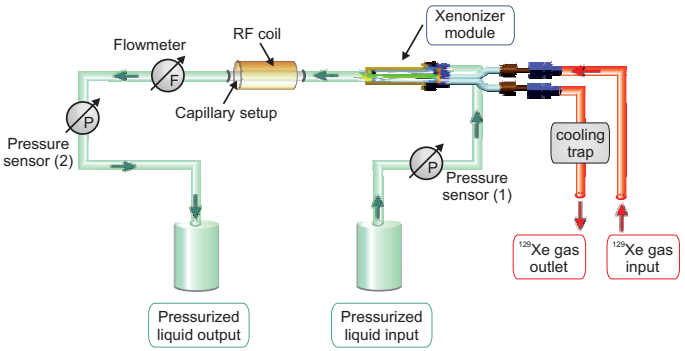

Figure 12.8.: Scheme of the setup used for experiments on samples placed after the xenonizer, e.g. capillary experiments.

For most experiments, they were placed in a glass cylinder to provide constant in- and outflow conditions, to enhance sample centering, and to reduce susceptibility effects. A photo of the setup is shown in Fig. 12.9, which also shows another tool to center the capillary within a 25 mm resonator. The glass cylinder was favorable, though, because it allowed for usage of a 10 mm rf resonator yielding a better filling factor and thus higher SNR. The capillary was approximately 10 cm long in order to establish stationary flow within the NMR resonator.

For all ^{129}Xe experiments, flow was driven by pressurizing the two fluid reservoirs, which also provided the necessary counter-pressure against the gas mixture. For ^{1}H velocimetry measurements [Utiu 12], the flow rate was set using the magnetically driven rotary blood pump. While measuring the flow rate with an ultrasonic flowmeter (Console T110R, Transonic Systems Inc., Ithaca, USA), the mean velocity was incremented from 4.53 mm/s to 453 mm/s for the ^{1}H experiments, corresponding to Reynolds numbers of 1 to 100. For the HP ^{129}Xe experiments, the flow rate was set to 12 ml/min, corresponding to a mean velocity of $\bar{v} = 450$ mm/s, a maximum velocity of $v_{\max} = 900$ mm/s and a Reynolds number of $Re = 100$. At this flow rate, HP ^{129}Xe could be replenished fast enough without introducing considerable flow artifacts by spins leaving the resonant volume.

For first testings, water and glycerin were mixed with a volume fraction ratio of 39/100 resulting in a dynamic viscosity of 3.6 mPas to match the viscosity of blood. For ^{1}H studies, the fluid was doped with $CuSO_4$ to reduce the longitudinal relaxation time T_1 to about 200 ms.

For all blood experiments, fresh porcine blood was used. In order to enhance longi-

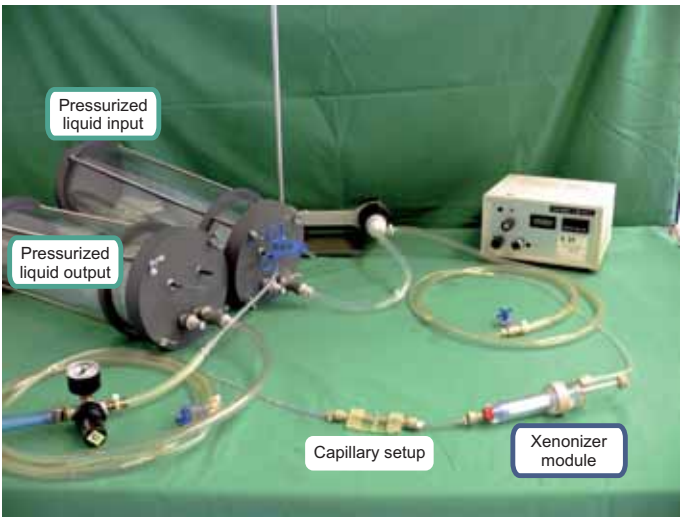

Figure 12.9.: Picture of the capillary flow setup including the xenonizer module.

tudinal relaxation for ^{1}H velocity mapping again, a Gd-complex-based doping reagent (Magnograf®, Bayer Schering Pharma AG, Germany) was added in a volume concentration of 0.05%, resulting in T_1 values of 80 ms and 230 ms for plasma and erythrocytes, respectively [Utiu 12].

Couette Setup

Regarding placement and control of xenonizer and fluid, the setup used for more advanced rheological studies within a Couette system resembles the one described for the capillaries. The Couette system, which was designed and purpose-built at the Helmholtz Institute, is sketched in Fig. 12.10. The technical drawing in Fig. 12.11 demonstrates the positioning within the bore-hole of the NMR magnet. All details on design, function and mechanical tests of this system can be found in [Hamilton 12]. In the Couette system used, well-defined blood flow was to be generated within a narrow gap while maintaining a laminar flow pattern in a wide range of velocities and shear stress values. Furthermore, an axial flow had to be realized in order to ensure continuous supply of fresh xenon-enriched blood. The Couette setup itself required a design that minimized damage of the blood, i.e., the conduction of the flow to and from the shear gap as well as sealings and construction

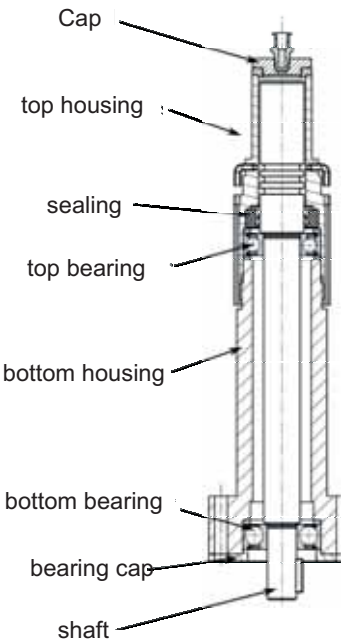

Figure 12.10.: Technical drawing of the Couette system [Hamilton 12].

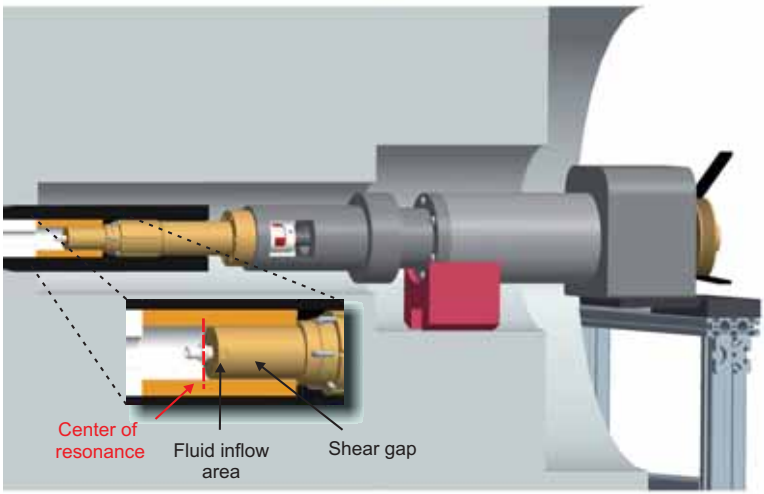

Figure 12.11.: Image of the Couette system placed inside the bore of the NMR magnet [Hamilton 12].

material had to be chosen with regard to highest hemo-compatibility. Furthermore, the system had to meet requirements resulting from the conditions it was to be used in: first, the geometric limitations due to the limited space within the bore-hole, and secondly, the necessity of non-magnetic materials. Even though an outer rotating cylinder is favorable for stable laminar flow, restricted space impeded the realization of this type of setup. The system used provided a shear gap of 0.7 mm with an average diameter of 18.7 mm. The mechanical drive for rotating the inner cylinder had to be positioned in the weak stray-field area of the magnet and was developed as a belt drive yielding a stable and low-vibrational force transmission for a wide range of rotational frequencies even across long distances.

12.1.4. Blood Preparation and Analysis

All experiments were performed with porcine blood, which was prepared and analyzed by cooperation partners at the Helmholtz Institute. It was obtained from the cut neck vessels immediately after death of a pig in the slaughterhouse and anti-coagulated by heparin (15.000 I.U. heparin/ml blood, corresponds to 3 ml Heparin-sodium-25000-ratiopharm; Ratiopharm GmbH, Ulm, Germany) and mixed with 1.6 ml of 50 % glucose solution (Glucose 50 %; DeltaSelect GmbH, Dreieich, Germany) per liter blood dissolved in 95 ml physiological saline solution (B. Braun Melsungen AG, Melsungen Germany).

Since, in general, the blood composition is not only species dependent but also differs greatly between individuals, certain blood parameters were equally adjusted for all experiments: The hematocrit was set to $Hct = 33.5\%$ by adjusting the hemoglobin content to 12 ± 1 g Hb/dl blood by adding saline solution and withdrawing plasma, respectively. In addition, the acid-base metabolism was controlled by means of the base excess value, which was set to 0 ± 5 by adding sodium hydrogen carbonate ($NaHCO_3$) (DeltaSelect GmbH, Dreieich, Germany) as needed. A summary of important blood and RBC parameters is given in Tab. 12.2. The further preparation steps depended on the experiment:

1. Blood oxygen saturation sO_2 was adjusted in a separate circuit according to DIN EN 12022. The blood is ventilated by means of an oxygenator (hilite2000, Medos Medizintechnik AG, Stolberg, Germany) with a gas mixture consisting of O_2, CO_2, and N_2. The gas component ratios were adjusted by a gas mixer (Medit, RWTH Aachen University, Aachen, Germany) according to the desired O_2 saturation of the blood at the corresponding O_2 and CO_2 partial pressures.

Table 12.2.: Characteristic blood and RBC parameters.

Parameter	Symbol	Value	Source
O_2 concentration in hemoglobin at 100% O_2 saturation	$c_{O_2}^{Hb}\,(sO_2 = 100\%)$	$1.34\,\frac{ml\,O_2}{g\,Hb}$	[Cummings 59]
Hemoglobin concentration in blood	c_{Hb}^{Blood}	$0.12\,\frac{g\,Hb}{ml\,Blood}$	
Mean hemoglobin concentration in RBC (MCH)	c_{Hb}^{RBC}	$2.15{\cdot}10^{-11}\,\frac{g\,Hb}{RBC}$	[Altman 71]
Mean RBC volume, MCV	V_{RBC}	$60\,\mu m^3$	[Altman 71]
Hematocrit	Hct	33.4%	

MCH: mean corpuscular hemoglobin; MCV: mean corpuscular volume

2. Plasma was derived from the supernatant of centrifuged whole blood. After adjusting the O_2 saturation, the whole blood was centrifuged in 50 ml flasks at 20,000 rpm for 15 min. The supernatant was pipetted and centrifuged again at the same conditions. The cell-free plasma as well as the erythrocyte concentrate was then filled into separate blood bags.

3. Erythrocyte concentrate was produced by centrifugation as described in paragraph 2.

Blood constituents were determined by an electronic cell counter, Celltac Alpha MEK-6400 (Nihon Kohden Corp., Tokyo, Japan). Plasma hemoglobin was determined spectrophotometrically. Partial pressures of oxygen (pO_2), carbon dioxide (pCO_2), and oxygen saturation (sO_2) were analyzed by the blood gas analyzer ABL800 Flex (Radiometer GmbH, Willich, Germany). In addition, total hemoglobin content as well as oxyhemoglobin (O_2Hb), carbon monoxide hemoglobin (COHb), methemoglobin (MetHb), and deoxyhemoglobin (RHb) were determined. Blood gas analysis was performed at 37°C and ambient pressure, whereas the NMR measurements were performed at 20°C and 2 bar pressure. The partial pressure and pH values were corrected to account for resulting temperature effects.

12.2. NMR Methods

Experiments were performed on a 7.4 T wide bore magnet, corresponding to a ^{129}Xe resonance frequency of 82.95 MHz, equipped with a Bruker AVIII spectrometer and a Bruker Micro 2.5 micro-imaging gradient system with a maximal strength of 1.50578 T/m (cf. Chapter 3). A ^{129}Xe/^{1}H double resonant Bruker rf birdcage coil with an inner diameter of 25 mm was used for excitation and signal acquisition. For the xenonizer as the sample, a 90° flip angle of the ^{129}Xe magnetization was attained by a rectangular 70 µs rf pulse at 57 W peak power. Spectra were acquired with varying numbers of scans to ensure acceptable signal-to-noise ratio (SNR) with a dwell time of typically $DW \approx 20\,\mu s$ to cover the region of interest of approximately 250 ppm.

For MR imaging experiments with selectively excited signals, gradient echo (GE) sequences were applied. By taking advantage of the large chemical shift difference between dissolved and the free ^{129}Xe gas of approximately 200 ppm and of the digital filter of the spectrometer, selective excitation of the signal of the water-dissolved ^{129}Xe was possible using a rectangular rf pulse. For analysis of configurations with more complex fluids that yield several dissolved signal peaks in the ^{129}Xe spectrum, gradient echo MRI was not applicable anymore without using selective rf pulses. Furthermore, a complete experiment would have had to be performed for each signal yielding incomparable results if the system did not provide high enough temporal stability.

Spectroscopic imaging (CSI, Chemical Shift Imaging) allowed for acquisition of all images within one experiment while maintaining the great advantage of the detailed information of ^{129}Xe NMR spectroscopy. By pure phase encoding of the spatial dimensions, an additional matrix dimension encoded the ^{129}Xe spectrum in the spin echo (SE). SNR values were determined by calculating the ratio of the maximal signal to the noise level, i.e., the root mean square of the signal, in the bottom right eighth of the image.

^{1}H velocity mapping was performed based on a PGSE sequence: the velocity-encoded phase map resulted from including a bipolar pair of velocity encoding gradients (length δ, spacing Δ) into a standard spin-echo imaging sequence after the spatial encoding gradient pulses. This map was then subtracted from a reference map without velocity-encoding gradients to yield the final velocity image. Data for all ^{1}H velocity maps shown in this work was provided by L. Utiu [Utiu 12].

For two-dimensional spectroscopy to directly measure ^{129}Xe exchange within the xenonizer setup, the EXSY experiment described in section 1.3.3 was conducted. Typically, a dwell time of $DW = 15\,\mu s$ with an original matrix size of (1024×64) Px^2 before zero-filling was used. All EXSY experiments were performed in TPPI mode.

Chapter 13.

Analysis of the Xenonizer Setup

In order to compare previous studies on xenon gas exchange via hollow-fibers [Wiesenack 02; Philipp 02; Hoffmann 09] to direct measurements of the dissolved gas by HP ^{129}Xe NMR, xenonizers have been designed and assembled with four different commercially available fiber types [Hamilton 12]. Among them are three polyolefin hollow-fiber membranes, which are already optimized for O_2 transport into blood and CO_2 elimination from blood: two microporous hollow-fiber membranes, OXYPHAN® and CELGARD®, and the diffusion membrane OXYPLUS® (Membrana GmbH, Wuppertal, Germany). In addition, the dissolution efficiency of a gas-tight polydimethylsiloxane membrane, Silclear (silicone tubing, Silclear Inc., Hampshire, UK), has been analyzed. All fiber types are known to be hemocompatible and biocompatible. The suitability of each fiber type regarding dissolution effectiveness, blood hemolysis, and stability of blood gas saturation parameters is compared quantitatively to facilitate improvements in future applications of the xenonizer technology as well as for clinical use of xenon as an anesthetic [Lynch 00].

NMR spectroscopy was performed on xenonizers with all fiber types and various carrier fluids, including water, saline solution (0.9 %), porcine plasma as well as porcine whole blood and erythrocyte concentrates at different oxygenation levels. Spectra that were acquired for the three different xenonizers all filled with whole blood at oxygenation levels of approximately 50 % are shown as examples in Fig. 13.1. Due to the complexity of the spectrum and the involved exchange processes between the multiple sites inside the xenonizer both leading to a distortion of the baseline, spectra were phased separately for regions around the gas peak and the dissolved xenon peaks. Within the spectra, free gas serves as the frequency reference at 0 ppm. Restricted diffusion within the fiber pores leads to broad signal distributions up to approximately 40 ppm [Demarquay 87; Golemme 03]. The high signal for OXYPHAN® within this region corresponds to the larger pore sizes of this material. ^{129}Xe that diffuses into the polymer yields broad signals

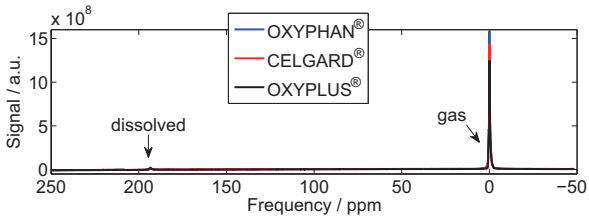

(a) Complete Spectrum

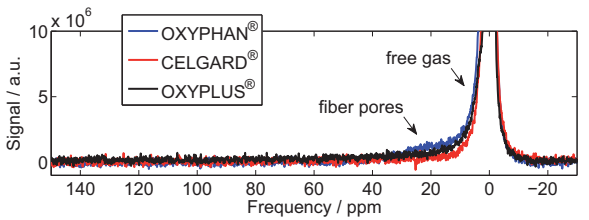

(b) -30 ppm - 150 ppm

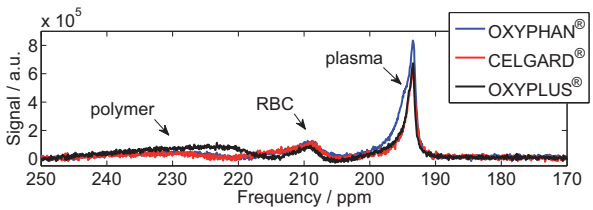

(c) 170 ppm - 250 ppm

Figure 13.1.: Example spectra acquired in whole blood using the three different hollow fibers. In (a), the complete spectrum is shown, while for more details the spectra were split into two parts with separate phasing and baseline corrections for (b) dissolved and (c) gaseous ^{129}Xe. NMR parameters used: 2048 Px, $DW = 20\,\mu s$, number of averaged scans: $NS = 32$, recycle delay TR = 3 s.

at approximately 223 ppm for the PMP fiber and 230 ppm for the two PP fibers, which is in good agreement with previous studies [Simonutti 06; Melian-Flaman 09]. The peak at 193.5 ppm is known to arise from dissolved ^{129}Xe in blood plasma, while the signal at approximately 209 ppm originating from ^{129}Xe bound to hemoglobin inside erythrocytes shifts with varying blood oxygenation due to conformational changes of the hemoglobin molecule [Albert 95; Bifone 96; Albert 00; Wolber 00a; Cherubini 03].

13.1. Optimization of the Dissolution Process

In order to optimize and quantify the dissolution process, gas and liquid flow rates were varied for an OXYPLUS®-xenonizer filled with water, and spectra with the xenonizer as the sample were acquired (Fig. 13.2). Repetitions of this experiment with small changes

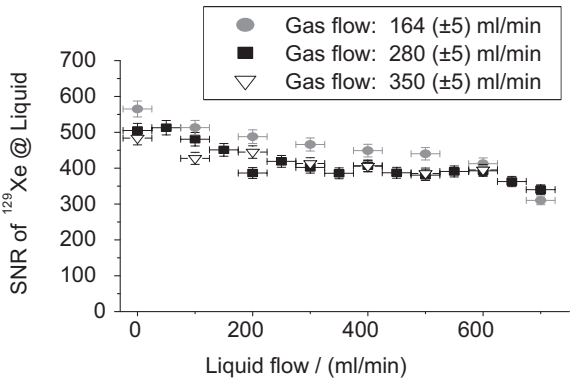

Figure 13.2.: Signal of water-dissolved HP ^{129}Xe, depending on liquid flow for three different flow rates of the gas mixture. Errors reflect pump calibration error and standard deviation of repeated experiments.

of the basic configurations of the system, especially experiments with different fractions of xenon in the gas mixture of the hyperpolarizer, produced slightly different data. Consequently, the flow rate calibration has to be repeated for individual non-standardized setups for precise quantitative comparison of signal intensities. The decrease of signal intensity with higher liquid flow rates is due to the decrease of dwell duration of the liquid inside the fiber module, thus leading to a reduction of the available time for mass transfer.

13.2. MRI of the Xenonizer Setup

Imaging studies of the OXYPLUS®-xenonizer setup consisted of transverse and longitudinal two-dimensional projections in order to analyze the transverse distribution of free and dissolved HP ^{129}Xe gas and of the axial dissolution efficiency along the fibers. For better comparison, all ^{129}Xe images are overlaid on conventional ^{1}H FLASH images (Fig. 13.3, 13.4).

In a first configuration, free HP ^{129}Xe gas was imaged without filling the fiber module with fluid in order to exclude distortions from ^{129}Xe site-exchange effects. The result in Fig. 13.3a properly shows the spatial distribution of the free gas around the fiber bundles and in the outer ring. The setting of the digital filter of the spectrometer led to a signal depletion at the edges of the frequency-encoded dimension. In the image, this lowered the gas signal from the outer ring in the X-direction to an intensity of the same order as the noise. The ring therefore appears to be interrupted due to this artifact.

In the next step, the xenonizer was filled with water. A GE experiment was performed under stopped liquid-flow conditions to minimize velocity-induced phase distortions. The acquired image (Fig. 13.3b) reflects the expected ring-shaped distribution. However, highest intensities can be found in a central region of the xenonizer around the core cylinder (PEEK, polyetheretherketone). While the achieved SNR does not permit significant quantification of this effect, one may deduce qualitatively, that gas dissolution is not equally effective across the xenonizer diameter, due to inhomogeneous flow pattern or partly clogged fiber lumen.

Additionally, the saline solution-filled xenonizer was studied by spectroscopic imaging (CSI) as a model setup for analysis with more complex fluids. Figure 13.3c demonstrates that within one experiment, results comparable to the standard GE images could be achieved. The higher signal intensity of the free gas in the outer ring of the xenonizer and consequently, the lower intensity within the fiber area is not only caused by the gas up-take into the fluid but also by a reversed gas flow leading to a loss of hyperpolarization by rf saturation. The inhomogeneous distribution of dissolved gas is reproduced in this image again very well.

Also longitudinal GE projections were acquired for a setup filled with saline solution. Figures 13.4a and b show the outcome of selective excitation of the gaseous and the dissolved HP ^{129}Xe, respectively, which were acquired in two separate experiments. The gas is equally distributed with the exception of a narrow region near the center. Here, a locally higher flow rate, which can be due to a narrowing of the hollow fibers, causes the spins to accumulate different additional velocity-encoding phases. This leads to the

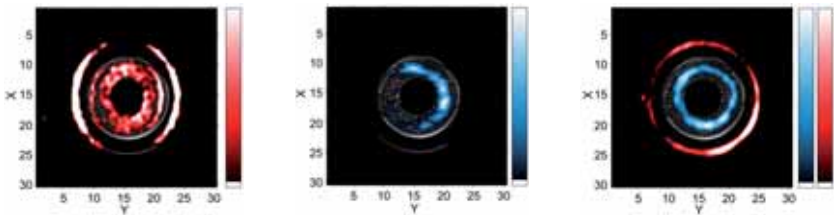

(a) Free HP ^{129}Xe gas in empty xenonizer (GE)

(b) Dissolved HP ^{129}Xe (GE)

(c) Free (red) and dissolved (blue) HP ^{129}Xe gas (CSI)

Figure 13.3.: Transverse HP ^{129}Xe 2D projection images (FOV = $(30 \times 30)\,\mathrm{mm}^2$, flip angle = 90°) of the xenonizer overlaid on gray-scale ^{1}H FLASH images ($TR = 60\,\mathrm{ms}$, $TE = 3.7\,\mathrm{ms}$, flip angle = 30°, slice thickness = 1 mm, $NS = 16$, original matrix size = $(512 \times 512)\,\mathrm{Px}^2$). (a) GE image of free HP ^{129}Xe gas: FOV = $(90 \times 80)\,\mathrm{mm}^2$, original matrix size = $(128 \times 128)\,\mathrm{Px}^2$, $NS = 2$, $TE = 10\,\mathrm{ms}$, $TR = 5\,\mathrm{s}$, $\mathrm{SNR}_{\mathrm{gas}} = 37$. (b) GE image of water-dissolved HP ^{129}Xe: FOV= $(30\times 30)\,\mathrm{mm}^2$, original matrix size= $(64\times 32)\,\mathrm{Px}^2$, $NS = 32$, $TE = 12\,\mathrm{ms}$, $TR = 3\,\mathrm{s}$, $\mathrm{SNR}_{\mathrm{dissolved}} = 54$. (c) CSI of saline solution-filled xenonizer: FOV = $(25 \times 25)\,\mathrm{mm}^2$, matrix size= $(256\times 32 \times 32)\,\mathrm{Px}^3$, $NS = 4$, $TE = 12\,\mathrm{ms}$, $TR = 0.5\,\mathrm{s}$, $\mathrm{SNR}_{\mathrm{gas}} = 154$, $\mathrm{SNR}_{\mathrm{dissolved}} = 24$.

ghost at the bottom of the image. The axial image of dissolved ^{129}Xe reflects a high dissolution efficiency throughout the entire fluid-filled regions with higher intensity in the area where the gas enters the fiber setup (here shown at the top of the image). The gas image exhibits no intensity deviations along the main axis and varying flip angles towards the edges as well as loss of hyperpolarization due to rf pulsing, or filtering effects should principally have the same impact on gaseous and dissolved signals. Thus, the observed intensity differences can be considered to be real dissolution efficiency variations.

These findings are supported by CSI, shown in Fig. 13.4c: the gaseous ^{129}Xe yields constant signal distribution across the entire xenonizer with the small depletion at the center already observed in Fig. 13.4a. The image of dissolved ^{129}Xe exactly reproduces results from GE imaging. Even though spatial resolution was lost again due to faster timings to account for the longer scan time of the pure phase encoding, comparisons of signals arising from the different sites are generally more reliable in terms of functional interpretations of the setup because the signals were acquired simultaneously. Furthermore, fluids with several dissolved ^{129}Xe signals, e.g. blood, could be imaged within the same time and without the need for selective rf excitation.

It should be noted that generally some attention has to be paid when quantitatively evaluating HP ^{129}Xe MRI results. As discussed in section 11.1.3, spin flips can be induced

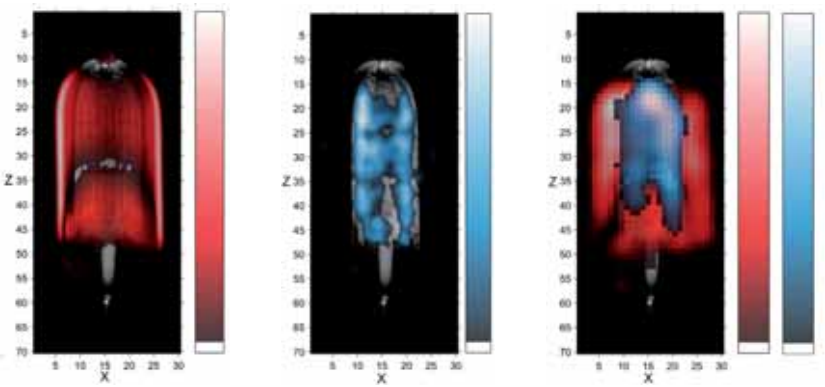

(a) Free HP ^{129}Xe gas (GE)

(b) Saline-dissolved HP ^{129}Xe (GE)

(c) Free (red) and saline-dissolved (blue) HP ^{129}Xe gas (CSI)

Figure 13.4.: Longitudinal HP ^{129}Xe 2D projection images (FOV = $(70 \times 30)\,\mathrm{mm}^2$, flip angle = 90°) of the saline solution-filled xenonizer overlaid on gray-scale ^{1}H FLASH image ($NS = 4$, original matrix size = $(512 \times 512)\,\mathrm{Px}^2$ for original FOV = $(100 \times 100)\,\mathrm{mm}^2$). (a) GE image of free HP ^{129}Xe gas: FOV = $(70 \times 50)\,\mathrm{mm}^2$, original matrix size = $(64 \times 64)\,\mathrm{Px}^2$, $NS = 8$; $TE = 7\,\mathrm{ms}$, $TR = 3\,\mathrm{s}$, $\mathrm{SNR}_{\mathrm{gas}} = 751$. (b) GE image of dissolved HP ^{129}Xe: FOV = $(100 \times 50)\,\mathrm{mm}^2$, original matrix size = $(64 \times 32)\,\mathrm{Px}^2$, $NS = 8$; $TE = 7\,\mathrm{ms}$, $TR = 6\,\mathrm{s}$, $\mathrm{SNR}_{\mathrm{dissolved}} = 217$. (c) CSI: FOV = $(70 \times 70)\,\mathrm{mm}^2$, original matrix size = $(256 \times 16 \times 16)\,\mathrm{Px}^3$, $NS = 4$; $TE = 11\,\mathrm{ms}$, $TR = 1\,\mathrm{s}$, $\mathrm{SNR}_{\mathrm{gas}} = 49$, $\mathrm{SNR}_{\mathrm{dissolved}} = 69$.

Table 13.1.: Average efficiencies ϵ of ^{129}Xe dissolution into fluid and RBCs calculated from normalized SNRs (depicted as dashed lines in Fig. 13.5). $\Delta\epsilon$ gives errors calculated from standard deviations of SNR averages of all experiments.

Fiber	ϵ_{Fluid} / a.u.	$\Delta\epsilon_{\text{Fluid}}$ / a.u.	ϵ_{RBC} / a.u.	$\Delta\epsilon_{\text{RBC}}$ / a.u.
OXYPHAN®	0.58	0.11	0.65	0.09
CELGARD®	0.50	0.10	0.60	0.13
OXYPLUS®	0.21	0.05	0.36	0.08

by magnetic field gradients. As a simple experiment with varied gradient strength and duration indicates (cf. section B.2), the switching of the imaging gradients can lead to significant loss of hyperpolarization. Since at constant switching times this effect becomes stronger with increasing gradient strength, this is a possible explanation for the difficulties experienced with high resolution HP ^{129}Xe MRI.

13.3. Dissolution Efficiencies of Different Fibers

For comparison of gas dissolution efficiencies of the various fibers, SNRs from several spectra were averaged after normalization to the number of signal averages and rescaling to the highest value. Because of slightly fluctuating HP gas volumes and because some blood samples were taken after particle sedimentation was not negligible anymore, signals were not calibrated to the free gas reference signal to account for fluctuations in the initial degree of hyperpolarization, nor to the hematocrit values measured before and after the experiments. Different gas-to-liquid ratios arising from different fiber-to-total volume ratios within the xenonizer (cf. section 12.1.2) were accounted for in the calculations.

The comparison in Fig. 13.5 and Tab. 13.1 shows that the highest degree of xenon dissolution is reached for OXYPHAN® fibers for both liquid phase and erythrocytes independent of the original filling fluid. While CELGARD® shows an average efficiency that complies with OXYPHAN® within experimental error, the amount of HP ^{129}Xe dissolved by OXYPLUS® is lower by approximately a factor of two. This major difference might be caused by the different material of this fiber type leading to faster relaxation of the ^{129}Xe hyperpolarization. More likely, the thin skin layer either prevents the xenon gas from dissolving into the carrier fluid or increases the relaxation rate.

In order to rule out that ^{129}Xe exchange is strongly altered by the different fiber types and thereby influences signal intensity ratios, the chemical shifts of ^{129}Xe at the fluid

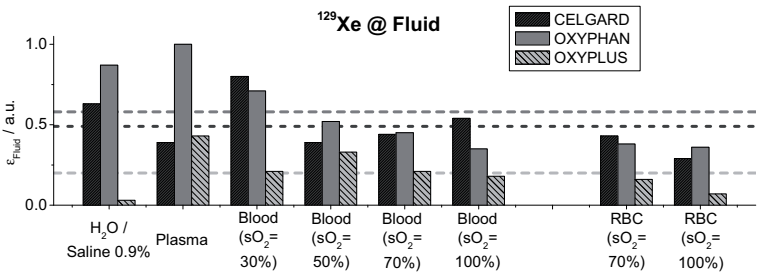

(a) Dissolution in fluid phase

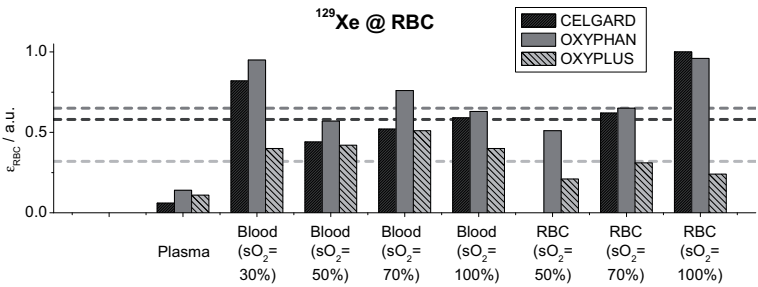

(b) Dissolution in cells

Figure 13.5.: Dissolution efficiencies of three different hollow fibers for varying fluids with which the xenonizers were filled, derived from (a) the ^{129}Xe in the fluid and (b) the ^{129}Xe in the RBCs. Averaged SNR values were normalized to maxima of fluid- and RBC-dissolved results, respectively. Two individual categories, for which no reliable data could be acquired, are displayed in gray. Dashed lines represent mean dissolution efficiencies of the according fiber averaged over all carrier fluids.

Table 13.2.: Average chemical shifts δ of HP ^{129}Xe at the fluid and the RBCs in ppm with reference to the free gas signal. Δδ gives errors calculated from standard deviations of averaged experiments.

Fiber	δ_{Fluid} / ppm	$\Delta\delta_{\text{Fluid}}$ / ppm	δ_{RBC} / ppm	$\Delta\delta_{\text{RBC}}$ / ppm
OXYPHAN®	193.0	0.1	206.4	1.3
CELGARD®	193.0	0.1	207.8	1.6
OXYPLUS®	193.2	0.2	207.6	1.5

phase and at the cells have been compared for all three fibers. If the fiber type played a role, a material-dependent change in chemical shift should be observed. The results (Tab. 13.2), clearly show that within the error the same shifts are observed. This proves that no corrections for dynamic effects have to be included in the above comparison of dissolution efficiencies.

13.4. Effects on Blood Parameters

An important aspect of the different xenonizer configurations is their impact on blood parameters. While blood flows through the xenonizer, all gases in the HP-gas mixture and in the blood exchange. This was studied by comparing various parameters from blood gas analysis before and after xenonizing a batch of whole blood for 20 min.

For analyzing oxygen degassing from the blood, O_2 saturations were measured before and after each experiment. The decay in O_2 saturations, ΔsO_2, for the three fiber types (Fig. 13.6) shows that oxygenation is retained for the longest period with CELGARD® fibers, whereas OXYPHAN® allows fastest exchange.

Because the administered gas mixture contains nitrogen, which has a great effect on the pH of blood, the blood samples were also analyzed for their pH values. The change of pH, ΔpH, over the xenonization phase is presented in Fig. 13.7. The differences in ΔpH between OXYPHAN® and OXYPLUS® may due to differences in N_2-flux of 8 ml/(cm min) and 5 ml/(cm min), respectively (manufacturer information).

The agreement of the sO_2 and pH results is expected since the bond lengths of O_2 and N_2 of 121 pm and 110 pm, respectively, can be considered equal on the scale of the pore diameters.

Finally, the content of free hemoglobin in the plasma was measured to quantify the hemolytic effects of the whole setup. However, no systematic difference within experi-

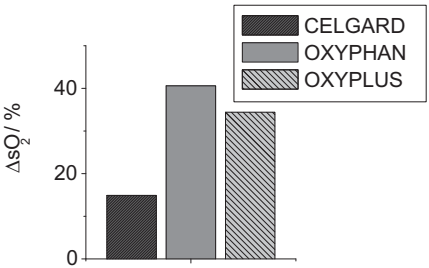

Figure 13.6.: O_2 saturation decrease of originally fully oxygenated blood samples over 20 min for different fibers. Results are calculated from oxygen saturation levels, sO_2, from blood sample analysis before and after 20 min xenonization periods (in cooperation with [Hamilton 12]).

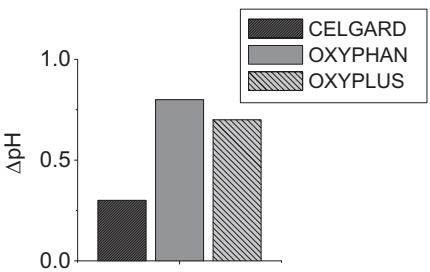

Figure 13.7.: Change in pH for different fibers derived from blood sample analysis before and after 20 min xenonization periods (in cooperation with [Hamilton 12]).

mental error was found between the three porous fiber types. Thus, mechanical blood damage through the fibers can be neglected for the comparison.

Chapter 14.

Biomedical Applications

Hyperpolarized ^{129}Xe, which was pre-dissolved into porcine blood, was employed in two different applications. First, it was used to study the blood-gas exchange dynamics in the xenonizer setup, including oxygen and xenon exchange measured by one- and two-dimensional HP ^{129}Xe spectroscopy. Secondly, HP ^{129}Xe was used as a sensor for blood rheology investigations under tube and Couette flow conditions.

14.1. Blood-Gas Exchange Dynamics

The first part of this chapter is devoted to online-monitoring of the change in blood oxygenation and the resulting possibility to derive important parameters of gas-exchange membranes. In the second section, the complex multi-site xenon exchange is measured directly in 2D HP ^{129}Xe EXSY experiments.

14.1.1. Online Monitoring of Blood Deoxygenation

Experiments on the xenonizer under stopped fluid-flow conditions revealed a change of the signal arising from HP ^{129}Xe in erythrocytes before and after a 20 min exposure to the gas flow. Figure 14.1 shows an example of consecutive spectra from whole blood in an OXYPHAN® xenonizer starting approximately 30 s after starting the gas flow.

The asymmetric line shape could indicate a chemical shift anisotropy (CSA) effect as described before by [Jameson 02] in nanochannels. However, the geometric scales within the xenonizer are orders of magnitude larger than nanochannels and only the fiber polymer presents a solid material in the region of interest. Therefore CSA can be ruled out as a possible origin of the observed RBC peak shape modification.

For solving the problem, blood gas analysis yielded valuable information. Before the measurements, the blood sample was almost 100% oxygenated with a partial O_2 pressure

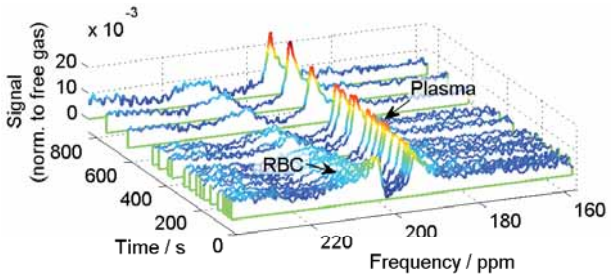

Figure 14.1.: Change of HP ^{129}Xe spectrum (160-240 ppm) of originally fully oxygenated porcine whole blood with exposure time to flow of hyperpolarization gas mixture.

of $pO_2 = 27.4\,\mathrm{mmHg}$ at 20°C which was found to be reduced to $pO_2 = 8.3\,\mathrm{mmHg}$ only thereafter. This indicates an O_2 exchange from the blood through the fibers into the gas space from which it is transported out of the setup with the flowing gas mixture.

Spectroscopically, one can observe that while the HP ^{129}Xe gas reference peak at 0 ppm remains unchanged and the plasma peak (194.2 ppm) experiences only minor narrowing, the signal assigned to xenon bound to the RBCs shows a significant chemical shift and change in peak width and shape over time. In Fig. 14.2, manually determined peak widths $\Delta\omega$, defined as full width at half maximum (FWHM), and positions δ are plotted. The

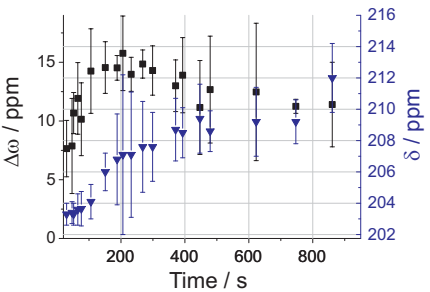

Figure 14.2.: Deoxygenation process of whole blood, manual evaluation. Peak width $\Delta\omega$ (FWHM, squares) and position δ (triangles) are plotted versus the xenonization time. Errors reflect estimated uncertainties in determination of the two parameters.

broadening of the total erythrocyte peak is interpreted as an increase of deoxygenated hemoglobin (RHb, ~208 ppm) and a decrease of oxygenated hemoglobin concentration (O_2Hb, ~201 ppm) reaching a maximum width after approximately 200 s. Afterwards, the

signal is dominated by xenon in deoxygenated hemoglobin and thus shows lower width at higher chemical shift values. In [Wolber 00a], the change in chemical shift between blood equilibrated with N_2 and with O_2 exhibited the opposite behavior. However, human instead of porcine blood was measured in those experiments in a completely different setup. The para- and diamagnetic character of RHb and O_2Hb, respectively, leads to varying reactions to the physical surroundings. Even more importantly, differences in cell size and blood composition of human and porcine blood may lead to different conformational changes and to different reactions of cofactors to varying gases, as indicated by the different chemical shifts found by [Tilton 82] (cf. section 11.3.1). A similar deviation has already been found regarding T_1 relaxation times between the work by Wolber et al. in a bulk blood sample and measurements performed in blood foam [Wolber 00b; Tseng 97]. In the first work, an increase of T_1 with increasing blood oxygenation was reported, whereas the opposite trend was found by Tseng et al.

The assignment of the two signals to RHb and O_2Hb in this work could additionally be supported by measurements of blood samples that were freshly inserted into the xenonizer after being equilibrated to different oxygenation levels. Figure 14.3 shows an example of data acquired with CELGARD® fibers. Hereby, other blood changes which might occur during the xenonization process are ruled out as reasons for the observed signal changes since the only varied parameter in the entire experiment is the blood oxygenation level.

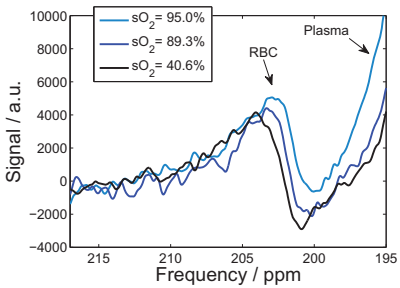

Figure 14.3.: HP ^{129}Xe spectra acquired in a CELGARD® xenonizer with freshly inserted whole blood at different oxygenation levels.

For reproduction and a more quantitative evaluation of this blood deoxygenation during the xenonization process, erythrocyte concentrates were administered into the setup to enhance SNR. After the start of the flow of the xenon gas mixture, spectra were acquired every 10 s. In Fig. 14.4, results for the three different hollow fiber types are depicted.

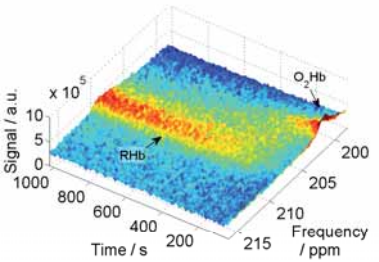

(a) OXYPHAN®

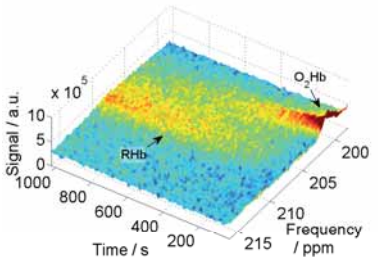

(b) CELGARD®

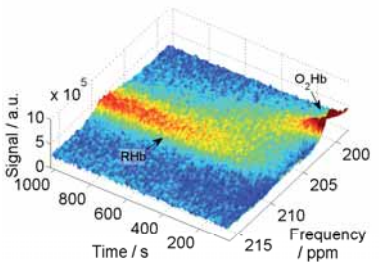

(c) OXYPLUS®

Figure 14.4.: HP ^{129}Xe RBC signals from erythrocyte concentrates in various fiber types depending on exposure time to xenonizer.

It can be seen that signals from oxygenated (203 ppm) and deoxygenated (212 ppm) Hb in RBCs can be spectroscopically resolved and do not yield one average Gaussian line as described before in the literature [Wolber 00a]. The collapse to one signal observed before is caused by fast exchange of the detected ^{129}Xe nuclei between oxy- and deoxyhemoglobin molecules. However, O_2 binding to one particular Hb molecule becomes more likely the more oxygen atoms are already bound to the four possible binding sites, which is expressed by the positive oxygen cooperativity of Hb. Therefore, a certain oxygen saturation level sO_2 is proportional to the concentration of oxyhemoglobin molecules $c_{O_2Hb}^{Blood}$, and accordingly $(1 - sO_2)$ is proportional to c_{RHb}^{Blood}. In a system like the xenonizer providing either slower exchange dynamics or another exchange pattern, detection of the ^{129}Xe magnetization before the chemical shift information from de-/oxyhemoglobin is averaged allows for spectroscopic separation of the two signals. To directly test if the detected line

truly is composed of two separate signals, selective saturation of one signal should leave the other unchanged, whereas in the case of one asymmetric line, the entire signal would be depleted. Yet, experiments revealed that the small chemical shift difference between the two presumed signals of only a few ppm and the exchange dynamics did not permit selective saturation and fast enough acquisition for a quantitative evaluation (Fig. B.4). Measurements of the same spectra with active flow of 58% oxygenated whole blood, however, manifested a less pronounced peak shape variation (Fig. B.5) because of enhanced exchange in the flowing and thus continously mixed blood. The exchange dynamics themselves are analyzed in the next section 14.1.2. The information that can be gained from the two distinct signals is derived by processing both signals separately in the following.

Assuming completely independent signals, two partly overlapping line shapes are expected. Corresponding fit results turned out to be rather unstable due to low SNR and imperfect baseline corrections. As an example, the gained peak widths $\Delta\omega$ of de-/oxygenated Hb in an OXYPHAN® xenonizer are shown in Fig. 14.5. Consequently, more robust evaluation protocols had to be chosen.

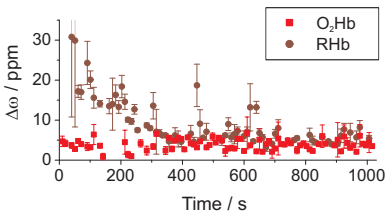

Figure 14.5.: Peak widths $\Delta\omega$ of de-/oxygenated hemoglobin in RBCs in OXYPHAN® xenonizer derived from fit of two Lorentzian line shapes. Error bars reflect fitting errors.

An alternative for the derivation of the line widths is based on calculations of the spectral moments of the respective signals. The n-th spectral moment of a spectral line $f(\omega)$ is defined as

$$M_n = \int (\omega - \omega_0)^n \, f(\omega) \, d\omega. \tag{14.1}$$

For Lorentzian lines with FWHM $\Delta\omega$, approximations need to be adhered to for the integrals to converge. A crude model assumes the curve to be zero outside the interval $|\omega - \omega_0| \leq \alpha$ with $\alpha \gg \Delta\omega$ [Abragam 61]. Neglecting terms of the order of $\Delta\omega/\alpha$, one

gains

$$M_2 = \frac{\Delta\omega\,\alpha}{\pi}, \tag{14.2}$$

$$M_4 = \frac{\Delta\omega\,\alpha^3}{3\pi}. \tag{14.3}$$

This approach was employed for the two RBC signals. The results are presented in Fig. 14.6. Regarding absolute values, the results have to be treated with some care, not

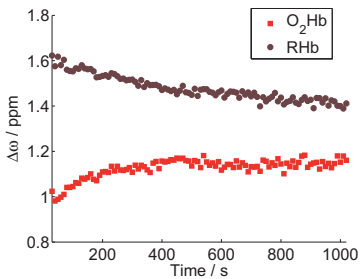

(a) OXYPHAN®

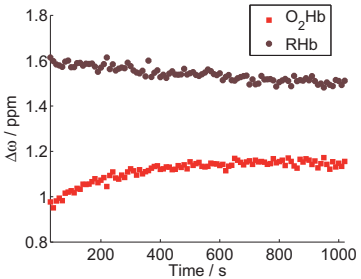

(b) CELGARD®

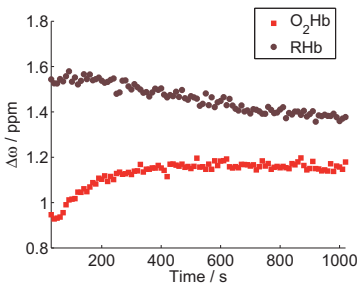

(c) OXYPLUS®

Figure 14.6.: Peak widths $\Delta\omega$ of de-/oxygenated hemoglobin (dark and light red, respectively) depending on exposure time to xenonizer. Values are derived from second and fourth spectral moments.

only because the calculation of the moments is based on an approximate model. Also, the condition $\alpha \gg \Delta\omega$ is not fulfilled completely satisfactory and the peaks do not drop to zero at the edges, especially in the area where they partly overlap. Thus, the determined data for $\Delta\omega$ do not reflect the FWHM but a less well-defined, lower peak width. Nevertheless,

similar behavior is noted for all fiber types: the signal from deoxygenated Hb narrows with increasing xenonization time indicating a decrease in paramagnetic susceptibility effects and an acceleration of internal dynamics. On the contrary, the oxygenated Hb signal becomes wider, which in turn gives reference of slower dynamics.

In order to quantify the deoxygenation effect itself, the integrals of the two peaks were determined and normalized to the total RBC signal to eliminate fluctuations. For modeling the gained data, the gas exchange model for hollow fibers presented in section 11.3 is used. Since it has been shown that xenon exchange with the fluid reaches equilibrium within less than a second [Amor 07; Zänker 07], the time dependence of the signals S_{ox} and S_{deox} of HP ^{129}Xe O_2Hb and RHb are only expressed in terms of the oxygen gas exchange:

$$S_{\text{ox}} \propto p\, L_{\text{Xe}}^{\text{O}_2\text{Hb}}(T) \cdot c_{\text{O}_2\text{Hb}}^{\text{Blood}}(t), \tag{14.4}$$

$$S_{\text{deox}} \propto p\, L_{\text{Xe}}^{\text{RHb}}(T) \cdot c_{\text{RHb}}^{\text{Blood}}(t), \tag{14.5}$$

where $L_{\text{Xe}}^{\text{O}_2\text{Hb/RHb}}(T)$ is the xenon solubility in de-/oxyhemoglobin that has been temperature-corrected according to Eq. (11.29). In [Kwan 69], it was shown that the solubility of xenon in water is directly proportional to the xenon gas pressure p. Therefore, L_{Xe} as defined for standard conditions at atmospheric pressure has been used here, adapted to the experimental conditions of 2 bar in the gas mixture by multiplication with p. For oxygen, independence of the gas pressure is assumed because of the dominance of the chemical binding of O_2 to hemoglobin. This translates into the assumption of a pressure-independent oxygen-binding capacity. Equivalently, the oxygen affinity $n = 2.7$ originally measured at $T = 37°C$ and pH= 7.4 [Tweeddale 73; Mockros 85; Willford 86; Cattaneo 06] is regarded constant during the experiment. The concentration of de-/oxyhemoglobin in the total blood sample $c_{\text{RHb/O}_2\text{Hb}}^{\text{Blood}}$,

$$c_{\text{O}_2\text{Hb}}^{\text{Blood}} = c_{\text{Hb}}^{\text{Blood}} \cdot sO_2, \tag{14.6}$$

$$c_{\text{RHb}}^{\text{Blood}} = c_{\text{Hb}}^{\text{Blood}} \cdot (1 - sO_2), \tag{14.7}$$

can be calculated based on Eq. (11.19), Eq. (11.25), the hematocrit measured before the experiment, and the mean corpuscular hemoglobin (MCH), $c_{\text{Hb}}^{\text{RBC}} = 2.15 \cdot 10^{-11}\,\text{g/RBC}$ [Altman 71]. While the partial oxygen pressure pO_2 changes with pH and temperature (cf. section 11.3.1), according to Eq. (11.20) sO_2 does not need to be corrected if only Hb-bound O_2 is considered and plasma-dissolved oxygen is again neglected. Otherwise, the pH change due to an uptake of nitrogen with an exchange rate k_{N_2} from the gas

mixture would have to be taken into account as well,

$$pH(t) \propto \exp\left\{-k_{\mathrm{N}_2}\, t\right\}. \tag{14.8}$$

The final model for the RBC signals of interest are then derived as:

$$S_{\mathrm{ox}} \propto p\, L_{\mathrm{Xe}}^{\mathrm{O_2Hb}}(T) \cdot \frac{c_{\mathrm{O_2,\,initial}}^{\mathrm{Blood}}}{1.34\,\frac{ml\,O_2}{g\,Hb}} \cdot \exp\left\{-\frac{A_{\mathrm{m}}}{V_{\mathrm{Blood}}}\, k_{\mathrm{O_2}}\, t\right\}, \tag{14.9}$$

$$S_{\mathrm{deox}} \propto p\, L_{\mathrm{Xe}}^{\mathrm{RHb}}(T) \cdot \left(c_{\mathrm{Hb}}^{\mathrm{Blood}} - \frac{c_{\mathrm{O_2,\,initial}}^{\mathrm{Blood}}}{1.34\,\frac{ml\,O_2}{g\,Hb}} \cdot \exp\left\{-\frac{A_{\mathrm{m}}}{V_{\mathrm{Blood}}}\, k_{\mathrm{O_2}}\, t\right\}\right), \tag{14.10}$$

where A_{m} is the active fiber area and V_{Blood} the participating fluid volume. The oxygen exchange rate $k_{\mathrm{O_2}}$ has been introduced in section 11.3.1 as the *mass transport coefficient*. Usually, it is defined in terms of rheological parameters yielding a proportionality to the fluid flow velocity as described in Eq. (11.26). Since the experiments in this study are performed under stopped blood flow, the mass transport coefficient would be zero according to this definition. Furthermore, an oxygen-saturation dependency of the effective O_2 diffusion coefficient and consequently of the mass transport coefficient has been described. In contrast, the change of oxygen saturation is the basis of the observations made here. Therefore, the constant $k_{\mathrm{O_2}}$ describing only the diffusive O_2 exchange without any convective or turbulent contributions is called *diffusive mass transport coefficient* in the following.

With RBC concentrates with hematocrit values measured as 92.4%, 98.5%, and 96.7% for OXYPHAN®, CELGARD®, and OXYPLUS®, respectively, and parameters found in Tab. 12.1, results presented in Fig. 14.7 were acquired. Fitting the data points with the above discussed model, the diffusive mass transport coefficients $k_{\mathrm{O_2}}$ for the three fiber types are derived. They are summarized in Tab. 14.1. Since both curves, S_{ox} and S_{deox}, describe the oxygen exchange *from* the blood, they should yield the same values for $k_{\mathrm{O_2}}$. The very good agreement found in the experimental results within experimental error support the validity of the employed model. In [Catapano 04], coefficients reflecting oxygen exchange into purified water were determined: As discussed in Chapter 11, the fluid flow rate influences the diffusive membrane layer. To avoid dependencies on the test module fluid dynamics, experimental data had to be extrapolated to *infinitely high* fluid velocities in [Catapano 04] yielding a value of $5.25 \cdot 10^{-4}\,\mathrm{m/s}$ for OXYPHAN® fibers and of $1.1 \cdot 10^{-5}\,\mathrm{m/s}$ for a fiber resembling OXYPLUS®. The asymmetric fiber again experienced lower oxygen exchange than the homogeneous membrane. Since in the present

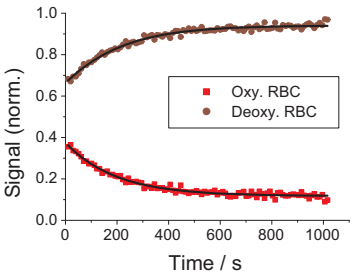

(a) OXYPHAN®

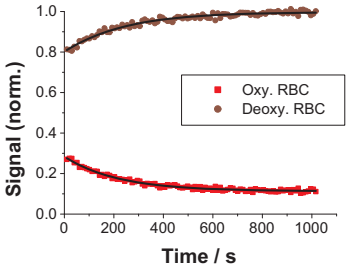

(b) CELGARD®

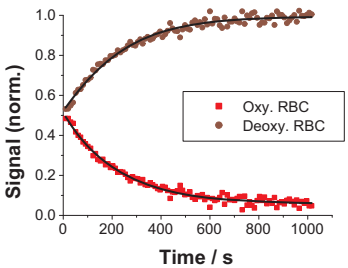

(c) OXYPLUS®

Figure 14.7.: Integrals of HP ^{129}Xe signals in oxy- and deoxy-hemoglobin normalized to the sum of both signals over the entire xenonization time. Black lines are fits with the models described by S_{ox} and S_{deox} (Eqs. (eq:Sox,eq:Sdeox)).

Table 14.1.: Diffusive mass transport coefficients $k_{\mathrm{O_2}}$ of oxygen in RBC concentrates at 2 bar gas pressure derived from HP ^{129}Xe signals in oxy- and deoxyhemoglobin. $\Delta k_{\mathrm{O_2}}$ are fitting errors.

Fiber	O_2Hb		RHb	
	$k_{\mathrm{O_2}}$ / 10^{-7} m/s	$\Delta k_{\mathrm{O_2}}$ / 10^{-7} m/s	$k_{\mathrm{O_2}}$ / 10^{-7} m/s	$\Delta k_{\mathrm{O_2}}$ / 10^{-7} m/s
OXYPHAN®	4.6	0.2	4.7	0.2
CELGARD®	7.2	0.3	7.0	0.3
OXYPLUS®	3.9	0.1	4.4	0.2

work, experiments can yield online information directly on blood without the necessity of model fluids, valuable additional information is provided for membrane design.

Additionally, the ratio $L_{Xe}^{O_2Hb}/L_{Xe}^{RHb}$ of xenon solubilities in oxy- and deoxyhemoglobin can be derived from the ratio of the proportionality factors of both signals. It was found to be 1.09±0.03, 1.12±0.03, and 1.01±0.03 in experiments with OXYPHAN®, CELGARD®, and OXYPLUS®, respectively. The errors only report fitting errors and have to be assumed higher due to the simplifications made before. However, they show good agreement for all measured fiber types. As a result, no significant difference in xenon solubility for the two Hb types could be confirmed at 20°C in contrast to the results found by [Ladefoged 67] at 37°C, which did not agree with [Chen 80] either.

14.1.2. Xenon Gas Exchange Dynamics in the Xenonizer

For further direct analysis of the exchange effects discussed above, HP ^{129}Xe 2D EXchange SpectroscopY (EXSY) experiments were performed on the same setup using an OXYPHAN® xenonizer. When the xenon gas was flowing during acquisition, signal distortions arose due to outflow of excited spins from the resonant volume and inflow of new, unexcited spins. Hence, the gas flow was trigger-stopped during acquisition using a magnetic valve. In [Cheng 08], this step has successfully led to significant increase of exchange signals. ^{129}Xe T_1 relaxation times in the gaseous and dissolved phases are of the order of seconds and thus significantly longer than the exchange time scales. As a result, spin-lattice relaxation could be neglected.

In order to derive information on the exchange dynamics, the mixing time τ_{mix} was varied between 0.5 ms and 30 ms. Results from $\tau_{mix} = 1$ ms and $\tau_{mix} = 30$ ms are illustrated in Fig. 14.8. More results with other mixing times can be found in Appendix B.4. A comparison of Fig. 14.8(a) and (b) shows that for small enough mixing times, only diagonal peaks are observable, but that increasing mixing times yield various exchange peaks. The most dominant exchange of ^{129}Xe at RBCs was observable with ^{129}Xe inside the fiber pores and the blood plasma (Fig. 14.9). The detectable direct exchange between RBCs and pores also causes the good resolution between O_2Hb and RHb discussed above, because it prevents the decrease of chemical shift difference due to fast exchange between the two Hb species.

As every EXSY experiment lasted for approximately one hour, every 2D spectrum had to be measured with a new portion of blood. Because fresh blood was available only every other day and was stored refrigerated in large syringes in the meantime, relevant variations in blood characteristics occurred due to cell sedimentation, hemolysis, microthrombosis,

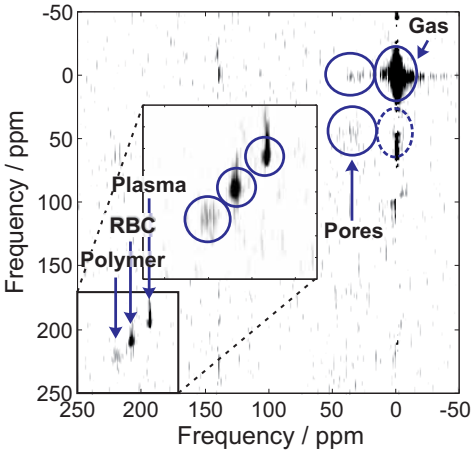

(a) $\tau_{\mathrm{mix}} = 1\,\mathrm{ms}$

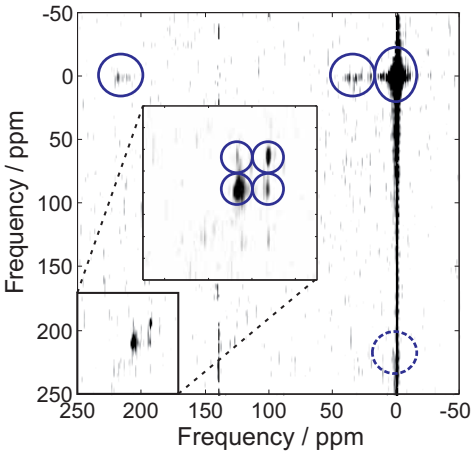

(b) $\tau_{\mathrm{mix}} = 30\,\mathrm{ms}$

Figure 14.8.: 2D EXSY spectra for two different mixing times τ_{mix}. TPPI mode with $NS = 16$, i.e., 2 averages, $TR = 2\,\mathrm{s}$, $DW = 15\,\mu\mathrm{s}$, orig. matrix size= $(1024 \times 64)\,\mathrm{Px}^2$.

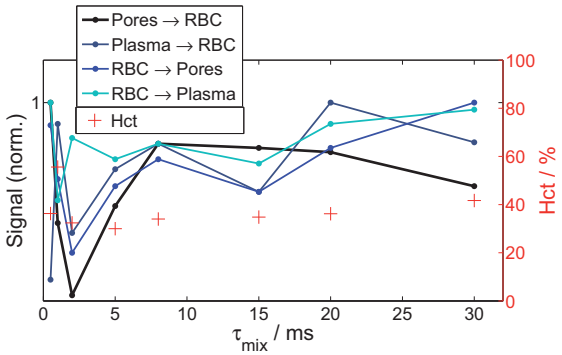

Figure 14.9.: Normalized intensities of selected RBC exchange peaks vs. EXSY mixing time. Red marks show hematocrit as example for variations in blood constitution between different experiments.

etc. An example of the measured parameters is the hematocrit shown in Fig. 14.9. Besides the rather low SNR, which could not be increased significantly by the interrupted gas flow either, these blood fluctuations led to an experimental error that hindered further quantitative analysis. Moreover, a normalization of the peak amplitudes to account for fluctuations of ^{129}Xe hyperpolarization was unfeasible. Usually, the free gas signal is used as a reference but as Fig. 1.12 demonstrates, this peak is expected to vary in this case as well. Fits with the two-site exchange model provided by Eq. (1.45) and (1.46) consequently yielded rather unreliable results with errors that were of the same order as the fit parameters themselves in some cases. In order to model the complex multi-site exchange, a matrix approach has been developed in [Dimitrov 95]. This explicitly requires good SNR, though, and therefore was not feasible for this work. Alternatively, simulations could be developed as demonstrated before for relaxation exchange in [Landeghem 10].

14.2. Analysis of Blood Flow Behavior

Dissolved hyperpolarized ^{129}Xe was used as a tool to gain further information on blood rheology. In the following two sections, experimental results of tube flow as well as of the more complex setup of a Couette system are presented.

14.2.1. Capillary Blood Flow

Model Fluid

^{129}Xe spectroscopy and imaging were performed on a capillary of 750 µm ID with the water-glycerin mixture. Figure 14.10a shows the image acquired with the CSI sequence to test the procedure on the model fluid at $Re = 100$. The velocity profile (Fig. 14.10b)

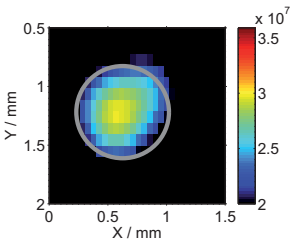

(a) ^{129}Xe CSI

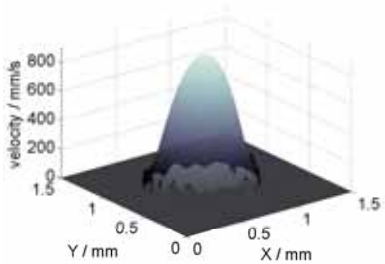

(b) ^{1}H velocity MRI [Utiu 12]

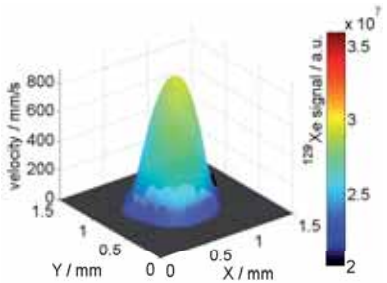

(c) Combined ^{1}H, ^{129}Xe

Figure 14.10.: (a) 2D CSI of water/glycerin-dissolved HP ^{129}Xe, echo time TE = 3 ms. Section of orig. FOV = (3×3) mm^2, res. = (47×94) µm^2 (after zero-filling by a factor of eight), $NS = 512$, SNR = 66, $TR = 130$ ms, total exp. time: 37 min. (b) ^{1}H velocity map ($Re = 100$). FOV = (1.5×1.5) mm^2, slice thickness = 4 mm, res. = (23×47) µm^2 (after two-fold zero-filling); $\Delta = 1.2$ ms, $\delta = 0.22$ ms, FOF = 1360 mm/s; $TR = 1$ s, $TE = 6.17$ ms , $NS = 32$, total exp. time: 34 min [Utiu 12]. (c) Graph combining (a) and (b).

was obtained using a conventional flow imaging spin-echo sequence as described above. Even though the ^{129}Xe image of H_2O/glycerin shows some distortions, which were caused

by imperfect sample centering and a possible demixing of the two constituents, the homogeneous distribution of the dissolved xenon can principally be reproduced. The signal depletion at the capillary walls is caused by the convolution of the real image data with the point spread function of the acquisition leading to a Gaussian-shaped signal suppression. The ^{1}H velocity map (Fig. 14.10b) shows perfectly parabolic velocity profiles across the capillary, which reflect the expected pattern of laminar tube flow at this Reynolds number with a maximum velocity of $v_{\max} = 2\,\bar{v}$.

Additional ^{129}Xe experiments in capillaries of ID = 500 µm were performed. However due to the reduction of the sample volume by a factor of two, the number of scans (NS) had to be increased to 2048 in order to achieve sufficiently high SNR. Since blood-dissolved HP ^{129}Xe generally yields even lower signal, further studies were restricted to the capillary size of 750 µm.

Blood Experiments

After successfully finished tests on model fluids, experiments on capillaries with blood and its constituents were performed. As an example, GE images of the flowing blood plasma extract ($Re = 100$) could be measured with high resolution (Fig. 14.11). The signal depletion in the lower right corner can be attributed to microbubbles passing the system the x- or y-axes of which are not aligned to the earth's gravitational field. The remaining inhomogeneities must be caused by minor fluctuations of initial degrees of hyperpolarization as well as of gas dissolution causing considerable effects at the rather low SNR level. Since in whole blood two signals are measured, CSI sequences were used here in order to acquire spatial as well as spectroscopic information within one single imaging experiment. An example of the results acquired in the spectroscopic domain is shown in Fig. 14.12a. Despite the very small chemical shift between plasma and erythrocytes of only about 10 ppm, both signals could be resolved. Integration of each peak for all spatial matrix points yielded the spectroscopic images in Fig. 14.12b, e.

For comparison, Fig. 14.12d, f show velocimetry results from ^{1}H experiments on plasma and on whole blood. While the plasma profile reflects similar behavior as the model fluid, the whole blood velocity profile only is of roughly parabolic shape and is flattened in the central region. As derived in [Whitmore 68; Han 01], this behavior of non-ideal Bingham plastics, which are viscous only with a minimum shear stress applied, are best described by Casson's model [Berger 96]:

$$v(r) = \frac{\Delta p}{4l\eta^2}(r_0^2 - r^2) - \frac{4}{3\eta^2}\left(\frac{\tau_y\,\Delta p}{2l}\right)^{1/2}(r_0^{3/2} - r^{3/2}) + \frac{\tau_y}{\eta^2}(r_0 - r), \tag{14.11}$$

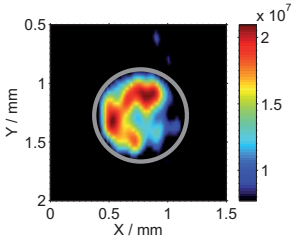

Figure 14.11.: 2D GE image of HP ^{129}Xe dissolved in plasma concentrate for comparison with later CSI. Since plasma gave rise to only one dissolved signal, it could be imaged with a spectroscopically non-selective sequence. Echo time $TE = 3\,\text{ms}$, $TR = 90\,\text{ms}$, section of original FOV $= (3 \times 3)\text{mm}^2$, res. $= (16 \times 31)\mu\text{m}^2$ (after four-fold zero-filling), $NS = 4\text{k}$, SNR $= 60$, total exp. time: 70:15 min.

where the yield stress $\tau_y = 0.109$ and the viscosity $\eta = 0.166$ are empirical constants [Whitmore 68] and Δp denotes the pressure difference along the capillary of length l and radius r_0. As in [Han 01], the blood velocity profile was fitted with both a parabolic function for Newtonian fluids and with Whitmore's Casson model (Fig. 14.13).

The spectral domain of one of the central voxels of the CSI data matrix (Fig. 14.12a) shows, that RBCs and plasma are still very well distinguishable despite the decreased spectral resolution to shorten acquisition time and despite enhanced exchange in the flowing system. The imaging results reflect the expected uniform spatial distribution as well as the respective intensities of plasma and erythrocytes within the capillary very well. It is important to note that even though at the Reynolds number used and with the achieved resolution, a Fåhraeus (-Lindqvist) effect is not observable, additional contrast between cells and plasma can be gained by variation of the repetition time for selective saturation of the plasma signal, because the plasma passes the capillary with lower velocities at the walls than the RBCs in the center.

In the ^{1}H velocity maps, a flattening of the velocity profile (Fig. 14.12f) can be observed that could be modeled with very good agreement by Whitmore's Casson model (Fig. 14.13) proving the non-Newtonian reaction of blood to shear stress. By decreasing the Reynolds number, which was performed for ^{1}H velocimetry at $Re = 100, 50, 10, 1$ (Fig. 14.14) but could not be obtained for ^{129}Xe due to the limitations of the flow rate discussed above, the flattening becomes more pronounced. This non-Newtonian behavior is mainly attributed to the deformability of the erythrocytes. Additionally, it can be explained by the so-called "rouleaux effect", found in very narrow blood vessels and

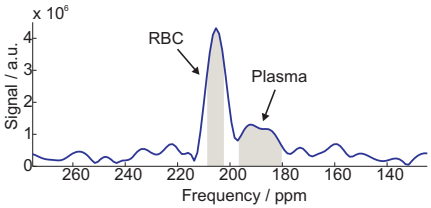

(a) ^{129}Xe, whole blood

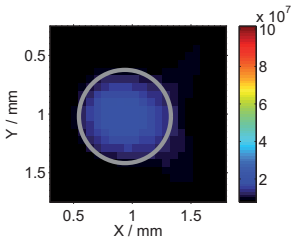

(b) ^{129}Xe, plasma

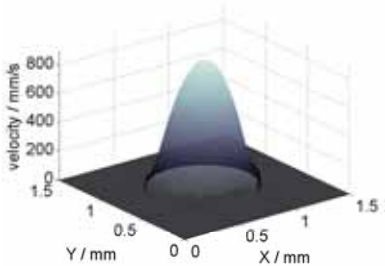

(c) ^{1}H, plasma [Utiu 12]

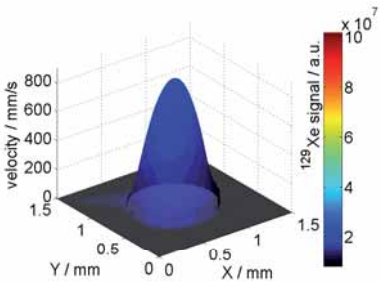

(d) Combined ^{1}H, ^{129}Xe, plasma

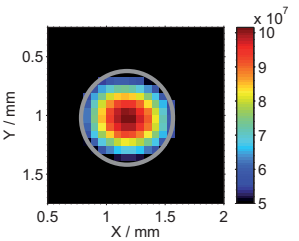

(e) ^{129}Xe, RBC

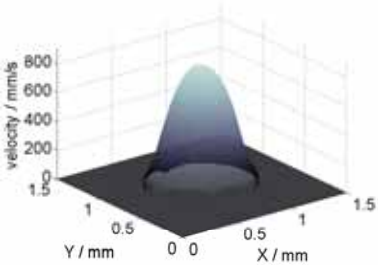

(f) ^{1}H, whole blood [Utiu 12]

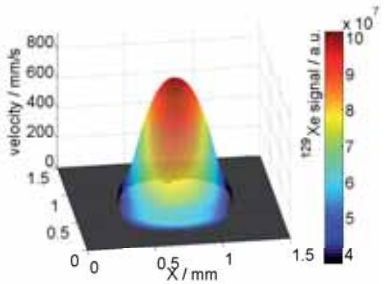

(g) Combined ^{1}H, ^{129}Xe, blood/RBC

Figure 14.12.: Blood flow investigation. (a) Magnitude spectrum (third dimension of CSI) of whole blood. Since no gas reference was available, the frequency scale was adapted from preceding spectra. Gray areas mark integration regions. (b, e) 2D CSI of blood-dissolved HP ^{129}Xe, echo time $TE = 3\,\text{ms}$. FOV $= (2 \times 2)\,\text{mm}^2$, res. $= (62 \times 62)\,\mu\text{m}^2$ (after eight-fold zero-filling), $NS = 4096$, $TR = 90\,\text{ms}$, total exp. time: 103 min (b) SNR = 42, (e) SNR = 222. (c, f) ^{1}H velocity maps ($Re = 100$). FOV $= (1.5 \times 1.5)\,\text{mm}^2$, slice thickness $= 4\,\text{mm}$, res. $= (23 \times 47)\,\mu\text{m}^2$ (after two-fold zero-filling); $\Delta = 1.2\,\text{ms}$, $\delta = 0.22\,\text{ms}$, FOF $= 1360\,\text{mm/s}$; $TR = 1\,\text{s}$, $TE = 6.17\,\text{ms}$, $NS = 32$, total exp. time: 34 min [Utiu 12]. (d, g) Graphs combining (b) and (c) as well as (e) and (f), respectively.

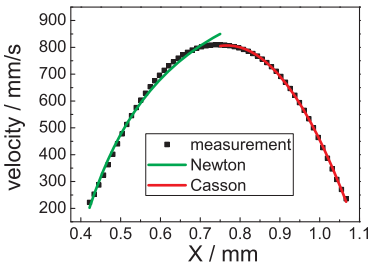

Figure 14.13.: Fit of parabolic function (green line) and of Casson's model (red line) to the velocity profile of whole blood (in analogy to [Han 01]) [Utiu 12].

under patho-physiological conditions [Goldsmith 71]: At low shear rates, the RBCs form extended aggregates and move as a coherent structure.

14.2.2. Blood Flow in the Couette System

In principal, the same experimental protocol was to be pursued for the Couette flow as for the capillaries, i.e., first images were to be acquired on model fluids before extension to spectroscopic MRI on porcine blood. However, test measurements on water-dissolved HP ^{129}Xe in the Couette system revealed significant difficulties: similar to experiments on capillaries with diameters of 500 µm, the very small sample volume in the 700 µm shear gap only yielded very low sensitivity. Furthermore, the Couette gap only filled a very small volume fraction of the resonator (cf. Fig. 12.11), which required slice selection of the respective area resulting in even lower SNR.

In order to enhance the NMR signal, another xenon carrier fluid was chosen for first tests. Lipid emulsions have been shown to render good results due to the lipophilic character of xenon gas [Amor 09]. Hence, Lipovenös® 20% (Fresenius Kabi GmbH, Germany) was used consisting of water with soy oil (20%), glycerin (2,5%), and egg phospholipids (1,2%). Besides instabilities of the xenonizer fibers over longer periods of time caused by the hydrophobic solvent, the gained signal was still very low, even though transverse flow was deactivated by stopping the rotation of the Couette cylinder. Even standard calibrations such as the setup of optimal rf pulses and of slice selection parameters turned out to be very difficult or even impossible. For demonstration purposes, Fig. 14.15c shows a longitudinal HP ^{129}Xe image acquired with a non-selective GE sequence, overlaid on a ^{1}H

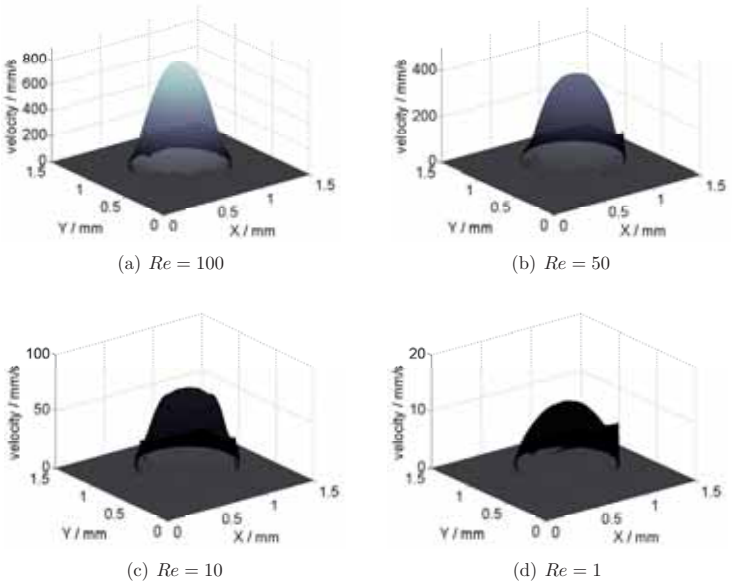

(a) $Re = 100$ (b) $Re = 50$

(c) $Re = 10$ (d) $Re = 1$

Figure 14.14.: ^{1}H velocity maps of whole porcine at $Re = 100, 50, 10, 1$ [Utiu 12]. Note that the scale of the z-axis varies while color coding of velocity is the same for all plots. FOV $= (1.5 \times 1.5)\,\text{mm}^2$, slice thickness $= 4\,\text{mm}$, res. $= (23 \times 47)\,\mu\text{m}^2$ (after two-fold zero-filling); (a) $\Delta = 1.2\,\text{ms}$, $\delta = 0.22\,\text{ms}$, FOF $= 1360\,\text{mm/s}$; TR $= 1\,\text{s}$, TE $= 6.17\,\text{ms}$, NS $= 32$, total exp. time: 34 min; (b) $\Delta = 3\,\text{ms}$, $\delta = 0.3\,\text{ms}$, FOF $= 680\,\text{mm/s}$; TR $= 1\,\text{s}$, TE $= 9.93\,\text{ms}$, NS $= 32$, total exp. time: 34 min; (c) $\Delta = 7\,\text{ms}$, $\delta = 0.5\,\text{ms}$, FOF $= 136\,\text{mm/s}$; TR $= 1\,\text{s}$, TE $= 18.33\,\text{ms}$, NS $= 32$, total exp. time: 34 min; (d) $\Delta = 7\,\text{ms}$, $\delta = 0.5\,\text{ms}$, FOF $= 13.6\,\text{mm/s}$; TR $= 1\,\text{s}$, TE $= 18.33\,\text{ms}$, NS $= 32$, total exp. time: 34 min.

GE image (b) for comparison. It reflects not only the low SNR but also that the relevant region of the Couette gap even in the projection image is hardly recognizable. Additional variations of sequence parameters which could not systematically be calibrated due to the lack of signal and which could have led to undesirable effects like signal weighting, e.g. repetition and echo times (TR, TE), did not yield any improvement. Consequently, experiments employing slice selection of the shear gap merely gave rise to small signals in ^{129}Xe spectra. One-dimensional profile images did not show a signal distinguishable from the noise level anymore.

On the basis of these results, successful spectroscopic MRI on model fluids and especially on blood for which plasma and cell signals need to be distinguished were unfeasible. Fundamental improvements needed to overcome these obstacles are suggested and discussed in the summary (Chapter 15).

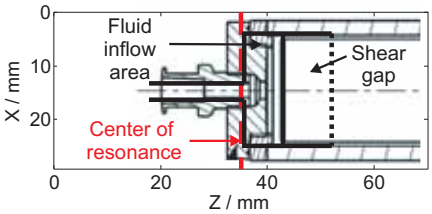

(a) Sketch

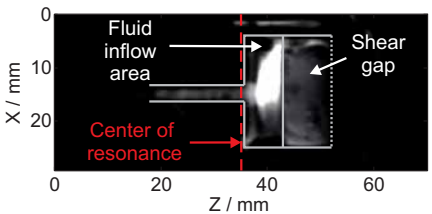

(b) ^{1}H image

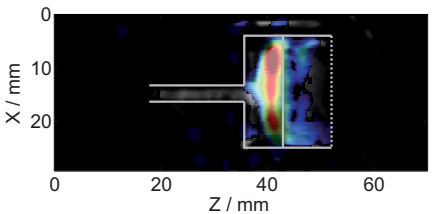

(c) HP ^{129}Xe image

Figure 14.15.: Longitudinal 2D GE images of the Couette system filled with Lipovenös®, FOV= (30×70) mm^2. (a) Sketch of Couette image. (b) ^{1}H image for comparison. Original matrix size = $(128 \times 16)\,\mathrm{Px}^2$, $NS = 2$, $TE = 5\,\mathrm{ms}$, $TR = 1\,\mathrm{s}$, SNR= 17400 (c) Dissolved HP ^{129}Xe image. Original matrix size = $(64 \times 16)\,\mathrm{Px}^2$, $NS = 16$, $TE = 5.5\,\mathrm{ms}$, $TR = 2\,\mathrm{s}$, SNR= 178, exp. time= 8 : 36 min.

Chapter 15.

Conclusions and Outlook

A recently introduced setup for continuous dissolution of hyperpolarized gases was systematically analyzed and optimized. A detailed perception of important features of this so-called xenonizer was given. By employing different hyperpolarized ^{129}Xe MRI schemes, spatially varying effectiveness of the system was ascertained. These kinds of experiments can further be employed for industrial optimization and standardization of xenonizer setups and for improvements of gas dissolution systems, e.g. clinical oxygenators, in general.

Moreover, a comprehensive experimental comparison of different hollow fibers was performed. Due to the fact that hyperpolarized NMR systems often suffer from fairly low reproducibility, which besides instabilities in the hyperpolarization process is mostly caused by the many variable parameters in complex, yet non-automated and non-standardized experimental setups, the study presented is based on multiple repetitions of each measurement and thus gives more reliable statistical evidence. It revealed that CELGARD® is favorable if the fluid under investigation is exposed to the xenonizer for a longer period and if a pre-defined oxygenation level and pH value need to be maintained essentially constant, since CELGARD® was found to offer longest oxygen and nitrogen exchange times in xenonization experiments. In contrast, OXYPLUS® fibers seem least feasible for HP ^{129}Xe dissolution due to the low dissolved ^{129}Xe signals observable. This is mainly attributed to depolarization effects in the skin layer of the material. OXYPHAN® fibers are best-suited for applications requiring continuously dissolved HP ^{129}Xe because highest signals were gained with this material.

In the future, a semi-permeable membrane with higher pressure resistance could bring about even further improvement by facilitating continuous dissolution of hyperpolarized gases under pressures up to several bars without the necessity to apply the same pressure onto the fluid side. The design of such a membrane that also meets the requirements of bio-compatibility and the conservation of the hyperpolarization of the passing gas is a

complex task and will be part of future investigations.

The results of the xenonizer studies formed the basis for different biomedical applications of dissolved HP ^{129}Xe. In section 14.1, the complex blood-gas exchange dynamics through oxygenation hollow-fiber membranes were studied by one- and two-dimensional NMR spectroscopy. For the first time, signals from HP ^{129}Xe in oxygenated and deoxygenated porcine hemoglobin could be spectroscopically resolved. This permitted online-monitoring of the deoxygenation process of oxygenated blood in the membrane module under stopped-flow conditions by evaluating the time evolution of the HP ^{129}Xe spectra by means of the derived model. An according gas-exchange model was derived for this purpose. A diffusive mass transport coefficient in analogy to the coefficient calculated for active blood flow in oxygenator engineering could be determined which quantifies the diffusive oxygen exchange rate.

The presented findings could be succeeded by many other experiments based on the same concept to achieve further knowledge on blood-gas dynamics. For example, the dependence of the mass transport coefficient on the gas diffusion as established in Chapter 11 could be used to determine diffusion behavior of gases like oxygen and xenon in whole blood in general, as well as between the cells and plasma via an effective diffusion coefficient in particular.

Since the HP ^{129}Xe spectra of the blood-filled hollow-fiber module had already revealed the multitude of exchange sites, two-dimensional exchange spectroscopy (EXSY) was performed to get deeper insight into the exact exchange mechanisms. A series of experiments with varying mixing times was successfully carried out showing various exchange signals at different exchange time scales. Regarding ^{129}Xe exchange with the fiber membrane, similar conclusions could be drawn as discussed before in the literature for fluid-free setups [Simonutti 06; Melian-Flaman 09]. For red blood cells, the detected signals revealed that ^{129}Xe exchange is most dominant with ^{129}Xe in plasma and in the pores of the fiber material. However, an exact, quantitative analysis of the exchange rates was impeded by fluctuations of blood parameters between individual experiments. In a first approximation, data were modeled employing a two-site exchange model for each exchange peak. Better correlation can be expected from multi-site exchange models as introduced by [Dimitrov 95], which require very good signal-to-noise ratios, though. Alternatively, quantitatively reliable exchange parameters could be gained by iterative approximation with simulations as shown for relaxation exchange in [Landeghem 10].

For future studies, better reproducibility of blood conditions by improving the experimental protocol forms a crucial basis for any quantitative analysis of gas exchange

dynamics in hollow-fiber membranes. Hyperpolarized ^{129}Xe signal enhancement could be achieved in several ways: first, the hyperpolarizing setup could be refined to reach higher initial degrees of polarization. Experimental and theoretical investigations, as presented for example in [Fink 07] for the flow of the Rb vapor, could offer valuable information. In addition, the fraction of ^{129}Xe in the gas mixture could be increased by either using isotopically enriched xenon gas or by collecting the HP ^{129}Xe in a freeze-out unit to separate Xe from the admixed He and N_2 gases. Finally, above discussed further optimization of the gas dissolution process would provide higher signal in the carrier fluid. These advancements will not only enable better quantitative assessments. The potential of faster measurements and better spectral resolution could, for example, also permit resolution of oxygenated and deoxygenated hemoglobin in two-dimensional EXSY experiments, as already achieved in the one-dimensional case. Similarly, enhanced exchange signals with the fiber pores and material will form a new and essential basis for gas-exchange membrane engineering.

In the last section of this work, the application of dissolved HP ^{129}Xe to blood rheology investigations has been demonstrated. The results give detailed insight into internal flow behavior of porcine blood in capillaries. Additionally, first results in a complex Couette geometry are presented. The combination of HP ^{129}Xe and ^{1}H MRI as demonstrated reveals flow patterns and spatial distributions of fluid constituents at the same time. HP ^{129}Xe spectroscopic imaging provides selective images of xenon continuously dissolved into erythrocytes and blood plasma. The images are acquired simultaneously within one experiment, thus yielding information under exactly the same conditions. Further improvements and higher temporal stability of the setup will allow for more signal averages and thus higher SNR, resolution. As a consequence, a wider range of Reynolds numbers will be accessible in the future. Hyperpolarized ^{129}Xe MRI results were combined with dynamic ^{1}H MRI to simultaneously map and measure flow giving deeper insight into the complex rheological behavior of blood.

In forthcoming experiments either with higher spatial resolution or in geometries of larger diameter, the procedure described will allow for actual measurement of effects like the Fåhraeus effect. This would even offer the possibility for enhanced molecular ^{129}Xe MRI contrast by selective saturation of slower flowing constituents. The combined illustration of ^{1}H maps and ^{129}Xe in particular facilitates better understanding of blood rheology in complex geometries, which is essential for physiology on the one hand and for optimization of blood-containing systems, e.g. blood pumps, dialyzers, and many more, with regard to internal flow conduction on the other hand. It may serve to test

predictions of theoretical models for flow in various systems. The microscopic NMR data can be correlated with the macroscopic rheological fluid parameters and compared with simulation results. This will lead to considerable improvements of medical devices and to further insights into multi-phase fluidic systems.

Conclusions

In this thesis, novel methods for nuclear magnetic resonance spectroscopy (NMR) and imaging (MRI) were investigated. In the first part, a new low-power rf excitation scheme termed Frank-sequence excitation was analyzed in detail, compared to conventional excitation, and was shown to be feasible for MRI. The second part focused on applications of hyperpolarized (HP) ^{129}Xe for advanced studies of gas dissolution via hollow-fiber membranes, blood-gas exchange dynamics, and blood rheology.

Frank-Sequence Excitation

Frank sequences, which have recently been introduced as an excitation scheme for NMR, employ a series of phase-modulated low-amplitude rf pulses with interleaved signal acquisition. Simulations and experiments were performed in order to find and quantify advantages as well as drawbacks of this new technique. These studies revealed that the distribution of total rf energy over a longer period of time allows for significant reduction of peak rf power. The phase modulation according to Frank sequences was shown to result in a consecutive excitation of narrow spectral windows with destructive interference of signals for surrounding frequencies. Mainly due to this effect, more rf energy than in conventional NMR excitation is required for equal sensitivity. Another consequence of the time-spread excitation and acquisition and the concomitant interference were undesirable variations in the excitation profile. Solutions such as limitations of pulse lengths and amplitudes were determined. These findings yield essential information for a deeper understanding of the new pulse scheme and will enhance future developments.

Furthermore, the concept of Frank-sequence excitation was employed for NMR imaging for the first time. With purpose-built phantoms, the feasibility of the method in combination with a two-dimensional radial imaging scheme was demonstrated. Together with a low-power slice selection sequence, three-dimensional MRI was successfully performed as well. A comparison with images that were acquired with conventional excitation and space encoding methods showed that the new technique provides a competitive alternative for future MRI applications. Besides offering the advantage of reduced rf power, Frank sequence MRI also provides a new modality to image hard materials and tissues like bones and teeth with short relaxation times in future applications.

Hyperpolarized ^{129}Xe NMR and MRI

Hyperpolarized ^{129}Xe that provides signal enhancements of several orders of magnitude compared to thermally polarized spin systems was employed to study gas dissolution by means of hollow-fiber membranes. These so-called xenonizers, which resemble clinical oxygenators and which have been shown to be feasible for dissolution of HP gases before, were investigated in detail including a systematical comparison of fibers with different structures and compositions. The study especially focused on the applicability of the setup for solving xenon in porcine blood, which is of great importance for future HP ^{129}Xe studies as well as for medical applications of the investigated fibers.

On the basis of these results, blood-dissolved HP ^{129}Xe was used as a tool to monitor gas exchange in the fiber module online. The signals of HP ^{129}Xe in oxygenated and deoxygenated hemoglobin could be spectroscopically resolved for the first time. Thereby, the oxygen exchange that takes place even under stopped blood-flow conditions could be followed and quantified by the specifically derived model. Additionally, two-dimensional NMR spectroscopy was used to further analyze the exchange of HP ^{129}Xe between the various sites in the xenonizer. Results for the exchange with the hollow-fibers showed good agreement with literature. Exchange of xenon with red blood cells was found to not only be significant with the surrounding plasma, but also in a more direct way with the fiber pores. These results form the basis for better understanding of physiological gas-exchange phenomena as well as for xenon anesthesia. Possibilities for further quantitative assessments were presented and discussed together with future experiments to gain more knowledge of fundamental blood-gas dynamics as well as for gas-exchange membrane design.

Dissolved HP ^{129}Xe was also applied as a sensor for rheological studies of blood flow in capillaries as well as for first tests in a Couette system. The chemical shift information achieved by HP ^{129}Xe was used as a means of molecular MRI. In combination with ^{1}H velocity MRI, a new method was presented for blood rheology investigations. While dissolved ^{129}Xe signals require further enhancement for applications in complex geometries, results in micro-capillaries already showed very good agreement with expected values. On the basis of the results presented, further studies of blood flow MRI in technical devices will be feasible.

In conclusion, two novel methods that focus on enhancing NMR and MRI without compromising advantages like non-invasiveness were analyzed to lead to better fundamental understanding on the one hand and were successfully employed in relevant applications

on the other hand. Together with suggestions for potential improvements, this work will hopefully stimulate future developments of new methods to further improve NMR and MRI and open paths for novel applications in science, engineering and biomedicine.

Appendices

Appendix A.

Frank-Sequence NMR - Calculation of the Effect of Finite Frank Pulse Length

The calculation of the excitation profile of Frank sequences considering finite pulse lengths in a continuous time domain was performed by Dr. Marcus Greferath and is presented here for completeness.

Frank sequences - the discrete case

Let m be a positive integer. Consider the sequence $(x_t)_{t=0,\ldots,m^2-1}$ where $x_t = \exp(\frac{2\pi i}{m} t_1 t_0)$, where $t_0, t_1 \in \mathbb{Z}_m$ are the unique elements in the m-adic representation of the number t. In other words, $t = mt_1 + t_0$, where t_1 is the quotient and t_0 the remainder when dividing t by m. Apparently x is of constant absolute value 1 and takes m distinct phases.

The Fourier transform X of x can easily be computed as

$$\begin{aligned} X_f &= \sum_{t=0}^{m^2-1} x(t)\, \exp(-\frac{2\pi i}{m^2} ft) \\ &= \sum_{t_0,t_1=0}^{m-1} \exp(\frac{2\pi i}{m^2}(mt_1 t_0 - ft)) \\ &= \sum_{t_0,t_1=0}^{m-1} \exp(\frac{2\pi i}{m^2}(mt_1 t_0 - mt_1 f_0 - t_0 f)) \\ &= \sum_{t_0=0}^{m-1} \exp(-\frac{2\pi i}{m^2} t_0 f) \sum_{t_1=0}^{m-1} \exp(\frac{2\pi i}{m} t_1 (t_0 - f_0)) \end{aligned}$$

A well-known argument from character theory reveals that

$$\sum_{t_1=0}^{m-1} \exp(\frac{2\pi i}{m} t_1(t_0 - f_0)) \;=\; \begin{cases} 0 & : \text{ if } t_0 \neq f_0, \\ m & : \text{ otherwise,} \end{cases}$$

such that the final expression for X is given by

$$X_f \;=\; m \, \exp(-\frac{2\pi i}{m^2} f_0 f).$$

This expression is of constant absolute value m, and hence x is a polyphase perfect sequence.

We mentioned above that the sequence x assumes exactly m distinct phases where it is of length m^2. It is not difficult to find examples of polyphase perfect sequences of length m^2 which assume more, i.e. typically m^2 phases. The literature does not seem to know any polyphase *perfect* sequences of length m^2 that assume less than m phases except by relaxing the definition of perfectness.

The discrete spectrum of the continuous case

We will now exchange the Frank sequence by a Frank function

$$x : [0, m^2) \longrightarrow \mathbb{C}, \; t \mapsto x(t) = \exp(\frac{2\pi i}{m} t_1 t_0).$$

Here, $t_1 \in \mathbb{Z}_m$ and $t_0 \in [0, m)$ are the unique elements in the m-adic representation of the real number t. Note that t_1 is discrete whereas t_0 is real-valued.

Computing the Fourier transform of this function, we will obtain a further continuous function $X : [0, m^2) \longrightarrow \mathbb{C}$, but for our purposes we will restrict our attention to its values on the discrete subset $\mathbb{Z}_{m^2}$ of $[0, m^2)$.

The Fourier transform X of x is computed as

$$\begin{aligned} X(f) &= \int_0^{m^2} x(t)\, \exp(-\frac{2\pi i}{m^2} ft)\, dt \\ &= \sum_{t_1=0}^{m-1} \int_0^m \exp(\frac{2\pi i}{m^2}(mt_1t_0 - f(mt_1 + t_0)))\, dt_0 \\ &= \int_0^m \sum_{t_1=0}^{m-1} \exp(\frac{2\pi i}{m^2}(mt_1t_0 - mt_1f_0 - t_0f))\, dt_0 \\ &= \int_0^m \exp(-\frac{2\pi i}{m^2} t_0 f) \sum_{t_1=0}^{m-1} \exp(\frac{2\pi i}{m} t_1(t_0 - f_0))\, dt_0 \end{aligned}$$

Our previously employed argument will not work as nicely here, as the expression

$$\sum_{t_1=0}^{m-1} \exp(\frac{2\pi i}{m} t_1(t_0 - f_0))$$

may take many complex values, given that t_0 and f_0 freely range over $[0, m)$. However, if we are only interested in integer values of f, then $f_0 \in \mathbb{Z}_m$ shows that only t_0 is the trouble-causing ingredient.

Our first attempt to rescue the approach will be to exchange the expression t_0 in the definition of x by $\lfloor t_0 \rfloor$, which is the value of the largest integer that does not exceed t_0. Then $x(t) = \exp(\frac{2\pi i}{m} t_1 \lfloor t_0 \rfloor)$, and the above derivation will take the form:

$$X(f) = \int_0^m \exp(-\frac{2\pi i}{m^2} t_0 f) \sum_{t_1=0}^{m-1} \exp(\frac{2\pi i}{m} t_1(\lfloor t_0 \rfloor - f_0))\, dt_0.$$

Now the above expression is given by

$$\sum_{t_1=0}^{m-1} \exp(\frac{2\pi i}{m} t_1(\lfloor t_0 \rfloor - f_0)) = \begin{cases} 0 & : \text{ if } \lfloor t_0 \rfloor \neq f_0, \\ m & : \text{ otherwise,} \end{cases}$$

so that the resulting value of X will be

$$\begin{aligned} X(f) &= \int_0^m \exp(-\frac{2\pi i}{m^2} t_0 f) \sum_{t_1=0}^{m-1} \exp(\frac{2\pi i}{m} t_1 (\lfloor t_0 \rfloor - f_0))\, dt_0 \\ &= m \int_{f_0}^{f_0+1} \exp(-\frac{2\pi i}{m^2} t_0 f)\, dt_0 \\ &= m \exp(-\frac{2\pi i}{m^2} f_0 f) \int_0^1 \exp(-\frac{2\pi i}{m^2} f s)\, ds \end{aligned}$$

When it comes to the absolute value $|X(f)|$ the above integral causes trouble. Before we evaluate this precisely, we will generalize further, namely to the case where our function $x(t)$ provides a series of pulses of arbitrary finite length $0 < \delta < 1$. In this case we have

$$x(t) = \begin{cases} \exp(\frac{2\pi i}{m} t_1 \lfloor t_0 \rfloor) & : \quad t_0 - \lfloor t_0 \rfloor \leq \delta, \\ 0 & : \quad \text{otherwise}, \end{cases}$$

and it can easily be checked that the final result of the above analysis will be

$$X(f) \;=\; m \exp(-\frac{2\pi i}{m^2} f_0 f) \int_0^\delta \exp(-\frac{2\pi i}{m^2} f s)\, ds.$$

In this expression the integral can be evaluated as

$$\int_0^\delta \exp(-\frac{2\pi i}{m^2} f s)\, ds \;=\; \begin{cases} -\frac{m^2}{2\pi i f} \left[\exp(-\frac{2\pi i}{m^2} f \delta) - 1\right] & : \quad \text{if } f \neq 0, \\ \delta & : \quad \text{otherwise}. \end{cases}$$

The latter can be simplified considering the following formula:

$$\begin{aligned} \frac{1}{2i}[\exp(-\frac{2\pi i}{m^2} f\delta) - 1] &= \exp(-\frac{\pi i}{m^2} f\delta)\, \frac{1}{2i}[\exp(-\frac{\pi i}{m^2} f\delta) - \exp(\frac{\pi i}{m^2} f\delta)] \\ &= \exp(-\frac{\pi i}{m^2} f\delta)\, \sin(-\frac{\pi}{m^2} f\delta). \end{aligned}$$

And now the formula for the absolute value of $X(f)$ becomes obvious:

$$\begin{aligned} |X(f)| &= \begin{cases} m\delta & : \quad \text{if } f = 0, \\ \frac{m^3}{\pi f} \left|\sin(\frac{\pi f}{m^2}\delta)\right| & : \quad \text{otherwise}, \end{cases} \\ &= m\delta \begin{cases} 1 & : \quad \text{if } f = 0, \\ \frac{|\sin(\frac{\pi f}{m^2}\delta)|}{\frac{\pi f}{m^2}\delta} & : \quad \text{otherwise}. \end{cases} \end{aligned}$$

Appendix B.

Hyperpolarized Xenon-129 NMR

B.1. Temperature Dependence of Blood-Dissolved HP Xenon-129 Signal

With the capillary setup described in Chapter 12 and shown in Fig. 12.8, the temperature dependence of the xenon solubility in porcine plasma and erythrocytes was measured. In Fig. B.1, the integrals of the acquired peaks are plotted. Even though the experimental error makes quantitative fit analysis unfeasible, the trend of decreasing solubility with increasing temperature described by Eq. (11.28) and (11.29) is principally observable. Significant changes in chemical shifts were not found. Also [Miller 81] only reported a

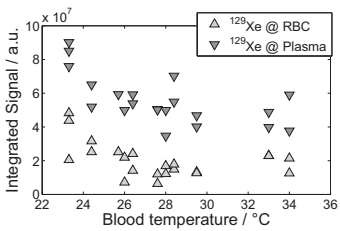

Figure B.1.: Analysis of dissolved HP ^{129}Xe signal with varying blood temperatures (with constant $sO_2 = 92\%$ measured at $T = 37°C$).

shift of a few tenths of ppm per °C temperature change and .

B.2. Effect of Gradient Switching on Hyperpolarization

In many MRI experiments using hyperpolarized ^{129}Xe, the acquired SNR and consequently achievable resolution are below theoretical expectations. Since this issue generally is not observed in NMR spectroscopy, the imaging gradients are assumed to cause a depolarization of the ^{129}Xe spin system.

In order to verify this hypothesis, a simple experiment was set up (Fig. B.2): a gradient of varying duration and strength was turned on and off before a 90° pulse with subsequent signal acquisition. If the gradient pulse had an effect on the longitudinal magnetization, a change of ^{129}Xe signal should be noted. The measurements were performed in the xen-

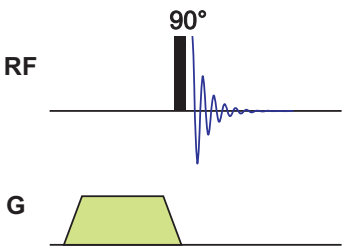

Figure B.2.: Pulse sequence to measure effect of gradients on hyperpolarization of ^{129}Xe spin system.

onizer setup with porcine plasma and whole blood (Fig. 12.7). The integrated signals from HP ^{129}Xe in the free gas space, dissolved in plasma, as well as in the red blood cells (RBCs) are shown in Fig. B.3. It is remarkable that while the gradient duration at constant strength does not influence the signal in any medium, the state of hyperpolarization appears to be increasingly destroyed with higher gradient strengths at constant duration. A rough estimation using Eq. (11.10) illustrates, that even at the maximum gradient strength of 1.5 T/m the relaxation time would not be affected enough to cause the observed signal decrease.

Thus, the depolarization could be caused by the *switching* of the gradients. Even though they are ramped up and down in 10 steps within 100 µs, imperfections, typical switching behavior, and eddy currents could lead to resonant spin flips. Since the switching time was kept constant in all experiments, the polarization reached equilibrium in tests with varying gradient duration, whereas the increasing gradient strengths came along with increasing steepness of the switching ramps and thus to stronger depolarizing effects.

In order to assure and proof this model, different experiments could be performed in the future. The characteristics of the gradient switching could be measured directly inside the NMR spectrometer with a pick-up coil that is connected to an oscilloscope. Frequencies in the range of the ^{129}Xe resonance frequency would be a further indication then. Additionally, experiments with varying ramp times should also yield valuable information. For easier understanding, these tests should first be performed in simpler systems than the xenonizer to avoid additional complexity by exchange processes.

B.3. Analysis of RBC Peak Shape

In order to verify that the signal from RBC-dissolved HP ^{129}Xe gained in a blood-filled xenonizer consists of two overlapping peaks from oxygenated and deoxygenated hemoglobin and does not reflect one asymmetric peak, e.g. due to CSA, one of the peaks was to be selectively saturated by a selective rf pulse. Ideally, the other signal should be unaffected if both signals are independent. However, due to the very small chemical shift difference between the peaks of interest of only a few ppm, the excitation bandwidth was not narrow enough to ensure selective saturation of only one signal (Fig. B.4). Furthermore, fast exchange between both sites during acquisition also causes a depletion of the unsaturated signal. This effect becomes even more evident in experiments with active blood flow, in which exchange is even more effective and further reduces the chemical shift difference between the two peaks. As a result, only one mean symmetric peak is observed again as described before in literature [Wolber 00a].

B.4. EXSY Spectra for Various Mixing Times

Here, additional EXSY results with mixing times $0.5\,\mathrm{ms} \leq \tau_{mix} \leq 30\,\mathrm{ms}$ are shown, from which for example data in Fig. 14.9 were gained.

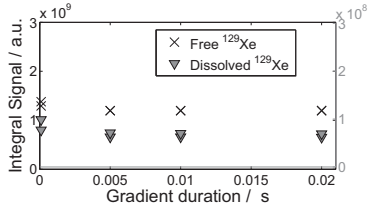

(a) Plasma, gradient strength = 50%

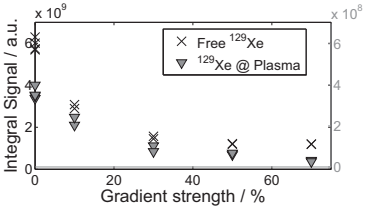

(b) Plasma, gradient duration = 10 ms

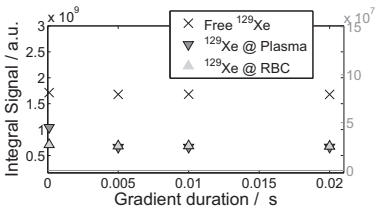

(c) Whole blood, gradient strength = 50%

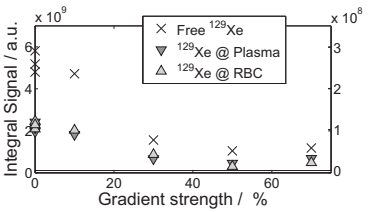

(d) Whole blood, gradient duration = 10 ms

Figure B.3.: Effect of imaging gradients on hyperpolarization. Integrated signals of dissolved HP ^{129}Xe plotted versus gradient time and duration acquired in a plasma- and whole blood-filled xenonizer.

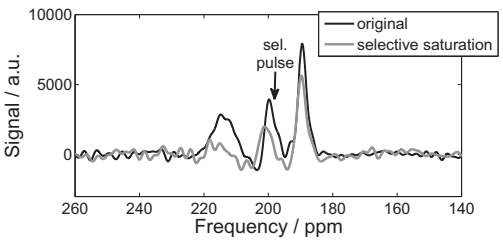

Figure B.4.: Spectra of HP ^{129}Xe dissolved in plasma, RBCs, and fiber polymer of 58% oxygenated porcine whole blood before (black line) and after selective saturation (gray line) of the right part of the RBC peak.

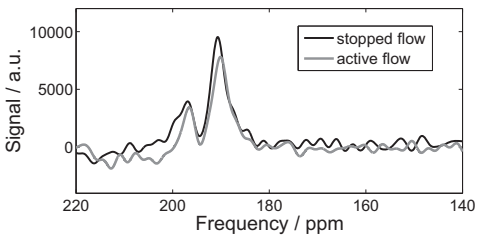

Figure B.5.: Spectra of HP ^{129}Xe dissolved in plasma and RBCs of 58% oxygenated porcine whole blood under stopped-flow (black line) and active-flow conditions (gray line).

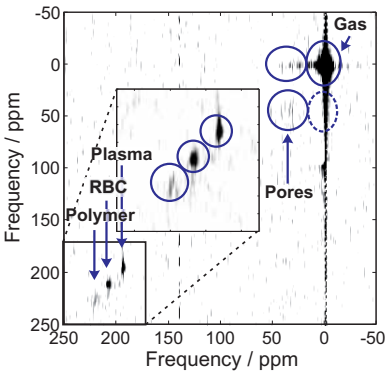

(a) $\tau_{mix} = 0.5\,\mathrm{ms}$

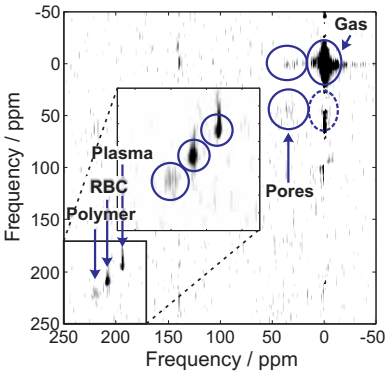

(b) $\tau_{mix} = 1\,\mathrm{ms}$

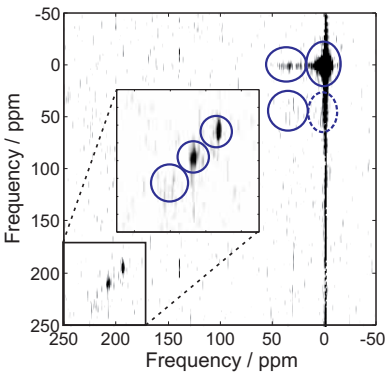

(c) $\tau_{mix} = 2\,\mathrm{ms}$

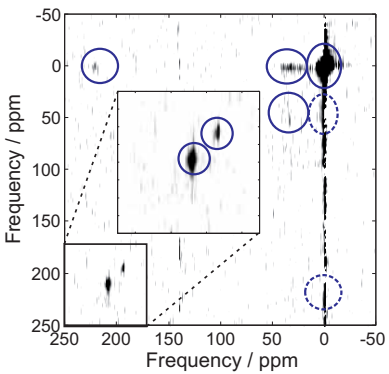

(d) $\tau_{mix} = 5\,\mathrm{ms}$

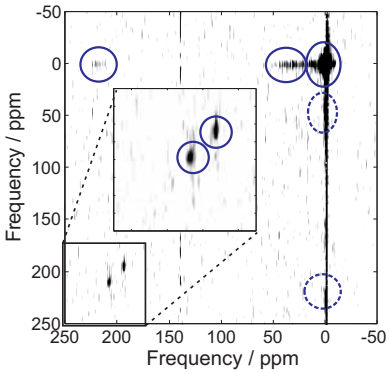

(e) $\tau_{mix} = 8\,\text{ms}$

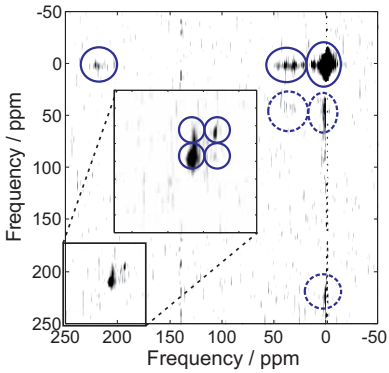

(f) $\tau_{mix} = 10\,\text{ms}$

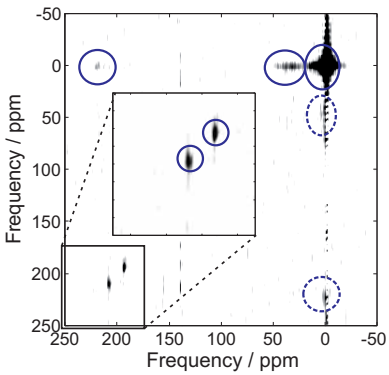

(g) $\tau_{mix} = 15\,\text{ms}$

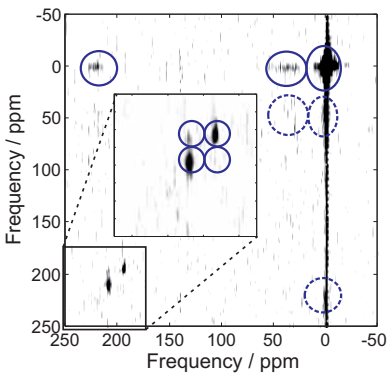

(h) $\tau_{mix} = 20\,\text{ms}$

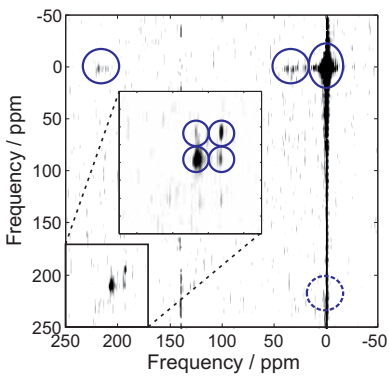

(i) $\tau_{mix} = 30\,\text{ms}$

Figure B.6.: 2D EXSY spectra for various mixing times τ_{mix}. TPPI mode with 16 scans, i.e. 2 averages, $TR = 2\,\text{s}$, $DW = 15\,\mu\text{s}$, orig. matrix size= $(1024 \times 64)\,\text{Px}^2$.

Bibliography

[Abragam 61] A. Abragam. Principles of Nuclear Magnetism. Oxford University Press (1961). Reprinted 1983.

[Abragam 78] A. Abragam, M. Goldman. Principles of Dynamic Nuclear Polarisation. *Rep. Prog. Phys.* **41**, 395–467 (1978).

[Albert 94] M. S. Albert, G. D. Cates, B. Driehuys, W. Happer, B. Saam, C. S. Springer Jr., A. Wishnia. Biological magnetic resonance imaging using laser-polarized ^{129}Xe. *Nature* **370**, 199–201 (1994).

[Albert 95] M.S. Albert, V.D. Schepkin, T.F. Budinger. Measurement of ^{129}Xe T_1 in Blood to Explore the Feasibility of Hyperpolarized ^{129}Xe NMR. *J. Comp. Assist. Tomogr.* **19**, 975–978 (1995).

[Albert 00] M. S. Albert, D. Balamore, D. F. Kacher, A. K. Venkatesh, F. A. Jolesz. Hyperpolarized ^{129}Xe T_1 in oxygenated and deoxygenated blood. *NMR Biomed.* **13**, 407–414 (2000).

[Altman 71] P. L. Altman, D.S. Dittmer. Blood and other body fluids. Biological Handbooks series. Fed. Am. Soc. Exp. Biol., Bethesda, Maryland, U.S.A. (1971).

[Amor 07] N. Amor. NMR und MRI von hyperpolarisiertem Xenon-129 in biorelevanten Flüssigkeiten. Diploma thesis, University Mainz (2007).

[Amor 09] N. Amor, P.P. Zänker, P. Blümler, F.M. Meise, L.M. Schreiber, A. Scholz, J. Schmiedeskamp, H.W. Spiess, K. Münnemann. Magnetic resonance imaging of dissolved hyperpolarized ^{129}Xe using a membrane-based continuous flow system. *J. Magn. Reson.* **201**, 93–99 (2009).

[Amor 11] Nadia Amor, Bernhard Blümich. Low-Power MRI by Frank-Sequence Excitation. *J. Magn. Reson.* **211**, 143–148 (2011).

[Appelt 98] S. Appelt, A. Ben-Amar Baranga, C. J. Erickson, M. V. Romalis, A. R. Young, W. Happer. Theory of spin-exchange optical pumping of ^{3}He and ^{129}Xe . *Phys. Rev. A* **58**, 1412–1439 (1998).

[Appelt 01] S. Appelt, F. W. Haesing, S. Baer-Lang, B. Blümich N. J. Shah. Proton magnetization enhancement of solvents with hyperpolarized Xenon in very low magnetic fields. *Chem. Phys. Lett.* **348**, 263 (2001).

[Appelt 04] Stephan Appelt. From Photon Spin to Magnetic Resonance Imaging. Habilitation, RWTH Aachen University (2004).

[Arnold 51] J. T. Arnold, S. S. Dharmatti, M. E. Packard. Chemical Effects on Nuclear Induction Signals from Organic Compounds. *J. Chem. Phys.* **19**, 507–507 (1951).

[Barnes 95] H.A. Barnes. A review of the slip (wall depletion) of polymere solutions, emulsions and particle suspension in viscometers: its cause, character, and cure. *J. Non-Newtonian Fluid Mech.* **56**, 221–251 (1995).

[Bartlett 62] N. Bartlett. Xenon Hexafluoroplatinate(V) Xe+[PtF6]-. *Proc. Chem. Soc.*p. 218 (1962).

[Baumer 03] D. Baumer, A. Fink, E. Brunner. Measurement of the ^{129}Xe NMR chemical shift of supercritical xenon. *Z. Phys. Chemie* **217**, 289–293 (2003).

[Baumer 06a] D. Baumer. *Herstellung von hyperpolarisiertem Xenon-129 und Anwendungen in der Flüssigkeits-NMR-Spektroskopie.* Dissertation, University Regensburg (2006).

[Baumer 06b] D. Baumer, E. Brunner, P. Blümler, P.P. Zänker, H.W. Spiess. NMR spectroscopy of laser-polarised ^{129}Xe under continuous flow. A method to study aqueous solutions of biomolecules. *Angew. Chem.* **45**, 7282–7284 (2006).

[Berger 96] S. A. Berger, W. Goldsmith, E. R. Levis. Introduction to Bioengineering. Oxford University Press, Oxford (1996).

[Bifone 96] A. Bifone, Y.-Q. Song, R. Seydoux, R. E. Taylor, B. M. Goodson, T. Pietrass, T. F. Budinger, G. Navon, A. Pines. NMR of laser-polarized xenon in human blood. *Proc. Natl. Acad. Sci. U.S.A.* **93**, 12932–12936 (1996).

[Blackshear 87] P.L. Blackshear, G.L. Blackshear. Mechanical Hemolysis. In Handbook of Bioengineering, pp. 15.1–151.19, Graw-Hill, New York (1987). R. Skalak and S. Chien.

[Blümich 82] B. Blümich, D. Ziessow. Saturation in hadamard NMR spectroscopy and its description by a correlation expansion. *J. Magn. Reson.* **46**, 385 – 405 (1982).

[Blümich 87] B. Blümich. White noise nonlinear system analysis in nuclear magnetic resonance spectroscopy. *Prog. Nucl. Magn. Reson. Spectr.* **19**, 331–417 (1987).

[Blümich 92] B. Blümich, W. Kuhn. Magnetic resonance microscopy. Wiley-VCH Verlag, Weinheim, 1. edition (1992).

[Blümich 00] B. Blümich. NMR Imaging of Materials. Clarendon Press, Oxford (2000).

[Blümich 09] B. Blümich, Q. Gong, E. Byrne, M. Greferath. NMR with excitation modulated by Frank sequences. *J. Magn. Reson.* **199**, 18–24 (2009).

[Blümler 08] P. Blümler, H.-D. Lemke, D. Krieter, H.-W. Spiess, F. Wiese, P. P. Zänker. Method for dissolution of gases with short-lived physical properties in a liquid (2008). Patent EP000001901782A2.

[Bloch 46a] F. Bloch. Nuclear Induction. *Phys. Rev.* **70**, 460–474 (1946).

[Bloch 46b] F. Bloch, W. W. Hansen, M. Packard. The Nuclear Induction Experiment. *Phys. Rev.* **70**, 474–485 (1946).

[Bloembergen 48] N. Bloembergen, E. M. Purcell, R. V. Pound. Relaxation Effects in Nuclear Magnetic Resonance Absorption. *Phys. Rev.* **73**, 679–712 (1948).

[Bludszuweit 94] C. Bludszuweit. *A Theoretical Approach To The Prediction Of Haemolysis In Centrifugal Blood Pumps.* Dissertation, University of Strathclyde, Glasgow (1994).

[Bohr 04] C. Bohr, A. Hasselbalch, A. Krogh. Über einen in biologischer Beziehung wichtigen Einfluss, den die Kohlensäurespannung des Blutes auf dessen Sauerstoffbindung übt. *Skand. Arch. Physiol.* **16**, 402–419 (1904).

[Bottomley 78] P. A. Bottomley, E. R. Andrew. RF magnetic-field penetration, phase-shift and power dissipation in biological tissue implications for NMR imaging. *Phys. Med. Biol.* **23**, 630–643 (1978).

[Bouchiat 60] M. A. Bouchiat, T. R. Carver, C. M. Varnum. Nuclear Polarization in ^{3}He Gas Induced by Optical Pumping and Dipolar Exchange. *Phys. Rev. Lett.* **5**, 373–375 (1960).

[Bowers 86] C. Russell Bowers, Daniel P. Weitekamp. Transformation of Symmetrization Order to Nuclear-Spin Magnetization by Chemical Reaction and Nuclear Magnetic Resonance. *Phys. Rev. Lett.* **57**, 2645–2648 (1986).

[Bracewell 95] R. N. Bracewell. Two-Dimensional Imaging. Englewood Cliffs. NJ. Prentice Hall (1995).

[Breeze 99] S. R. Breeze, S. Lang, I. Moudrakovski, C. I. Ratcliffe, J. A. Ripmeester, B. Simard. Coatings for optical pumping cells and extending the lifetime of hyperpolarized xenon. *J. Appl. Phys.* **86**, 4040–4042 (1999).

[Breit 31] G. Breit, I. I. Rabi. Measurement of Nuclear Spin. *Phys. Rev.* **38**, 2082–2083 (1931).

[Brunner 98] E. Brunner, R. Seydoux, M. Haake, A. Pines, J. A. Reimer. Surface NMR Using Laser-Polarized ^{129}Xe under Magic Angle Spinning Conditions. *J. Magn. Reson.* **130**, 145–148 (1998).

[Budinger 91] T. F. Budinger, H. Fischer, D. Hentshel, H. E. Reinfelder, F. Schmitt. Physiological effects of fast oscillating magnetic field gradients. *J. Comp. Assist. Tomogr.* **15**, 609–614 (1991).

[Callaghan 93] P.T. Callaghan. Principles of NMR Microscopy. Clarendon Press, Oxford (1993).

[Casson 59] N. Casson. A flow equation for pigment-oil suspension of the printing ink type. In Rheology of Disperse Systems, pp. 84–104, Pergamon Press, New York (1959). C.C. Mills.

[Catapano 04] G. Catapano, R. Hornscheidt, A. Wodetzki, U. Baurmeister. Turbulent flow technique for the estimation of oxygen diffusive permeability of membranes for the oxygenation of blood and other cell suspensions. *J. Membr. Sci.* **230**, 131–139 (2004).

[Cates 88] G. D. Cates, S. R. Schaefer, W. Happer. Relaxation of spins due to field inhomogeneities in gaseous samples at low magnetic fields and low pressures. *Phys. Rev. A* **37**, 2877–2885 (1988).

[Cates 92] G. D. Cates, R. J. Fitzgerald, A. S. Barton, P. Bogorad, M. Gatzke, N. R. Newbury, B. Saam. Rb−^{129}Xe spin-exchange rates due to binary and three-body collisions at high Xe pressures. *Phys. Rev. A* **45**, 4631–4639 (1992).

[Cattaneo 06] G. F. M. Cattaneo. *Entwicklung eines hochintegrierten intravaskulären Membranoxygenators für die Behandlung des akuten Lungenversagens.* Dissertation, RWTH Aachen University (2006).

[Chann 02] B. Chann, I. A. Nelson, L. W. Anderson, B. Driehuys, T. G. Walker. ^{129}Xe-Xe Molecular Spin Relaxation. *Phys. Rev. Lett.* **88**, 113–201 (2002).

[Chen 80] R. Y. Z. Chen, F.-C. Fan, S. Kim, K.-M. Jan, S. Usami, S. Chien. Tissue-blood partition coefficient for xenon: temperature and hematocrit dependence. *J. Appl. Physiol.* **49**, 178–183 (1980).

[Cheng 08] C.-Y. Cheng, J. Pfeilsticker, C. R. Bowers. Dramatic Enhancement of Hyperpolarized Xenon-129 2D-NMR Exchange Cross-Peak Signals in Nanotubes by Interruption of the Gas Flow. *J. Am. Chem. Soc.* **130**, 2390–2391 (2008).

[Cherubini 03] A. Cherubini, A. Bifone. Hyperpolarized xenon in biology. *Prog. Nucl. Magn. Reson. Spectrosc.* **42**, 1–30 (2003).

[Chien 70] S. Chien, S. Usami, R. J. Dellenback, M. I. Gregersen. Shear-dependent deformation of erythrocytes in rheology of human blood. *Am. J. Physiol.* **219**, 136–142 (1970).

[Chmiel 73] H. Chmiel. Zur Blutrheologie in Medizin und Technik. Habilitation, RWTH Aachen University (1973).

[Chupp 87] T. E. Chupp, M. E. Wagshul, K. P. Coulter, A. B. McDonald, W. Happer. Polarized, high-density, gaseous ^{3}He targets **36**, 2244–2251 (1987).

[Cleveland 09] Z. I. Cleveland, H. E. Möller, L. W. Hedlund, B. Driehuys. Continuously Infusing Hyperpolarized ^{129}Xe into Flowing Aqueous Solutions Using Hydrophobic Gas Exchange Membranes. *J. Phys. Chem. B* **113**, 12489–12499 (2009).

[Clever 79] H. L. Clever. Bd. 2: Krypton, Xenon and Radon. Pergamon Press (1979).

[Colegrove 63] F.D. Colegrove, L.D. Schearer, K. Walters. Polarization of ^{3}He Gas by Optical Pumping. *Phys. Rev.* **132**, 2561–2572 (1963).

[Cummings 59] J.N. Cummings, I.H. Kaiser. The blood gases, pH, and plasma elecrolytes of the sow and fetal pig and 106 days of pregnancy. *Am. J. Obstet. Gynec.* **77**, 10–17 (1959).

[Dadok 74] J. Dadok, R. F. Sprecher. Correlation NMR spectroscopy. *J. Magn. Reson.* **13**, 243–248 (1974).

[Deetjen 99] P. Deetjen, E.-J. Speckmann (eds.). Physiologie. Urban & Fischer Verlag, München, 3. edition (1999).

[Demarquay 87] J. Demarquay, J. Fraissard. ^{129}Xe NMR of xenon adsorbed on zeolites: Relationship between the chemical shift and the void space **136**, 314–318 (1987).

[Dimitrov 95] V. S. Dimitrov, N. G. Vassilev. Dynamic NMR: a New Procedure for the Estimation of Mixing Times in the 2D EXSY Experiments. A Four-Site Exchange System Studied by 1D and 2D EXSY Spectroscopy. *Magn. Res. Chem.* **33**, 739–744 (1995).

[DIN 08] IEC 60601-2-33: Medical electrical equipment - Particular requirements for the safety of magnetic resonance equipment for medical diagnosis (July 2008).

[Doddrell 86] David M. Doddrell, J. Mark Bulsing, Graham J. Galloway, William M. Brooks, James Field, Michael Irving, Hiram Baddeley. Discrete isolation from gradient-governed elimination of resonances. DIGGER, a new technique for in vivo volume-selected NMR spectroscopy. *J. Magn. Reson.* **70**, 319–326 (1986).

[Driehuys 95] B. Driehuys, G. D. Cates, W. Happer. Surface Relaxation Mechanisms of Laser-Polarized ^{129}Xe. *Phys. Rev. Lett.* **74**, 4943–4946 (1995).

[Driehuys 96] B. Driehuys, G. D. Cates, E. Miron, K. Sauer, D. K. Walter, W. Happer. High-volume production of laser-polarized ^{129}Xe. *Appl. Phys. Lett.* **69**, 1668–1670 (1996).

[Driehuys 06] B. Driehuys. Toward Molecular Imaging with Xenon MRI. *Science* **314**, 432–433 (2006).

[Driehuys 09] B. Driehuys, H. E. Möller, Z. I. Cleveland, J. Pollaro, L. W. Hedlund. Pulmonary Perfusion and Xenon Gas Exchange in Rats: MR Imaging with Intravenous Injection of Hyperpolarized ^{129}Xe. *Radiology* **252**, 386–393 (2009).

[Eash 04] H. J. Eash, H. M. Jones, B. G. Hattler, W. J. Federspiel. Evaluation of plasma resistant hollow fiber membranes for artificial lungs. *ASAIO J.* **50**, 491–497 (2004).

[Ernst 66] R.R. Ernst, W.A. Anderson. Application of Fourier transform spectroscopy to nuclear magnetic resonance. *Rev. Sci. Instrum.* **37**, 93–102 (1966).

[Ernst 70] Richard R. Ernst. Magnetic resonance with stochastic excitation. *J. Magn. Reson.* **3**, 10–27 (1970).

[Ernst 87] R. R. Ernst, G. Bodenhausen, A. Wokaun. Principles of Nuclear Magnetic Resonance in One and Two Dimensions. Oxford University Press, 1. edition (1987).

[Ernst 92] R. R. Ernst. Nuclear Magnetic Resonance Fourier Transform Spectroscopy (Nobel Lecture). *Angew. Chem.* **31**, 805–930 (1992).

[Fan 96] P. Fan, M. Darnell. Sequence Design for Communications Applications. John Wiley & Sons Inc., New York, New York (1996).

[Ferretti 76] J.A. Ferretti, R.R. Ernst. Interference effects in NMR correlation spectroscopy of coupled spin systems. *J. Chem. Phys.* **65**, 4283–4293 (1976).

[Fink 07] A. Fink, E. Brunner. Optimization of continuous flow pump cells used for the production of hyperpolarized ^{129}Xe: A theoretical study. *Appl. Phys. B* **89**, 65–71 (2007).

[Flieger 98] R. Flieger. *Entwicklung einer laserdiffraktometrischen Meßmethode zur Bestimmung der Elastizität der Erythrozytenmembran mittels zentrifugaler Belastung.* Dissertation, RWTH Aachen University (1998).

[Frisch 33] R. Frisch, O. Stern. Über die magnetische Ablenkung von Wasserstoffmolekülen und das magnetische Moment des Protons. I. *Z. Physik A Hadrons and Nuclei* **85**, 4–16 (1933).

[Fujiwara 01] H. Fujiwara, A. Kimura, Y. Yanagawa, T. Kamiya, M. Hattori, T. Hiraga. Relaxation behavior of laser-polarized ^{129}Xe gas: Size dependency and wall effect of the t1 relaxation time in glass and gelatin bulbs. *J. Magn. Reson.* **150**, 150–160 (2001).

[Fung 81] Y. C. Fung. Biomechanics. Mechanical Properties of Living Tissues. Springer Verlag, Berlin, Heidelberg, New York (1981).

[Fung 96] Y.C. Fung. Biomechanics Circulation. Springer Verlag, Berlin, Heidelberg, New York (1996).

[Garroway 01] A.N. Garroway, M.L. Buess, J.B. Miller, B.H. Suits, A.D. Hibbs, G.A. Barrall, R. Mathews, L.J. Burnett. Remote sensing by nuclear quadrupole resonance. *IEEE Trans. Geosci. Remote Sens.* **39**, 1108 – 1118 (2001).

[Giersiepen 90] M. Giersiepen, L. Wurzinger, R. Opitz, H. Reul. Estimation of shear stress-related blood damage in heart valve prostheses - in vitro comparison of 25 aortic valves. *Int. J. Artif. Organs* **113**, 300–306 (1990).

[Goldsmith 71] H. L. Goldsmith. Red cell motion and wall interaction in tube flow. *Fed. Proc.* **30**, 1588–1588 (1971).

[Golemme 03] G. Golemme, J.B. Nagy, A. Fonseca, C. Algieri, Yu. Yampolskii. ^{129}Xe-NMR study of free volume in amorphous perfluorinated polymers: comparsion with other methods. *Polymer* **44**, 5039–5045 (2003).

[Goodson 02] B. M. Goodson. ADVANCES IN MAGNETIC RESONANCE, Nuclear Magnetic Resonance of Laser-Polarized Noble Gases in Molecules, Materials, and Organisms. *J. Magn. Reson.* **155**, 157–216 (2002).

[Grover 78] B. C. Grover. Noble-Gas NMR detection through noble-gas rubidium hyperfine contact interaction. *Phys. Rev. Lett.* **40**, 391–392 (1978).

[Gupta 74] R. K. Gupta, J. A. Ferretti, E. D. Becker. Rapid Scan Fourier Transform NMR Spectroscopy. *J. Magn. Reson.* **13**, 275–290 (1974).

[Haake 97] M. Haake, A. Pines, J. A. Reimer, R. Seydoux. Surface-Enhanced NMR Using Continuous-Flow Laser-Polarized Xenon. *J. Am. Chem. Soc.* **119**, 11711–11712 (1997).

[Haase 86] A. Haase, J. Frahm, D. Matthaei, W. Haenicke, K.-D. Merboldt. FLASH imaging, rapid NMR imaging using low flip-angle pulses. *J. Magn. Reson.* **67**, 258–266 (1986).

[Hahn 50] E. L. Hahn. Spin Echoes. *Phys. Rev.* **80**, 580–594 (1950).

[Haken 03] H. Haken, H. Wolf. Atom- und Quantenphysik. Springer Verlag, 8. edition (2003).

[Hamilton 12] K. Hamilton. *Modellsystem zur Analyse der Erythrozytenströmung im NMR-Hochfeld mittels hyperpolarisiertem ^{129}Xenon.* Dissertation, RWTH Aachen University (2012).

[Han 01] S.-I. Han, O. Marseille, C. Gehlen, B. Blümich. Rheology of Blood by NMR. *J. Magn. Reson.* **152**, 87–94 (2001).

[Han 04] S. Han, H. Kühn, F.W. Häsing, K. Münnemann, B. Blümich, S. Appelt. Time resolved spectroscopic NMR imaging using hyperpolarized 129Xenon. *J. Magn. Reson.* **167**, 298 (2004).

[Han 05] S.-I Han, S. Garcia, T. J. Lowery, E. J. Ruiz, J. A. Seeley, L. Chavez, D. S. King, D. E. Wemmer, A. Pines. NMR-Based Biosensing with Optimized Delivery of Polarized ^{129}Xe to Solutions. *Anal. Chem.* **77**, 4008–4012 (2005).

[Happer 84] W. Happer, E. Miron, S. Schaefer, D. Schreiber, W. A. van Wijngaarden, X. Zeng. Polarization of the nuclear spins of noble-gas atoms by spin exchange with optically pumped alkali-metal atoms. *Phys. Rev. A* **29**, 3092–3110 (1984).

[Heimiller 61] R.C. Heimiller. Phase shift pulse codes with good periodic correlation properties. *IRE Trans. Inf. Theory* **IT-7**, 254–257 (1961).

[Heimiller 62] R.C. Heimiller. Author's comment. *IRE Trans. Inf. Theory* **IT-8**, 382 (1962).

[Hoffmann 09] N. Hoffmann. *Zur Frage der Stofftransporteigenschaften von Oxygenatorhohlfasermembranen bezüglich der Durchlässigkeit für Fluide und Narkosegase.* Dissertation, RWTH Aachen University (2009).

[Hoppe 62] R. Hoppe, W. Dähne, H. Mattauch, K. M. Rödder. Fluorierung von Xenon **74**, 903 (1962).

[Idiyatullin 06] Djaudat Idiyatullin, Curt Corum, Jang-Yeon Park, Michael Garwood. Fast and quiet MRI using a swept radiofrequency. *J. Magn. Reson.* **181**, 342–349 (2006).

[Idiyatullin 08] Djaudat Idiyatullin, Curt Corum, Steen Moeller, Michael Garwood. Gapped pulses for frequency-swept MRI. *J. Magn. Reson.* **193**, 267–273 (2008).

[Imai 08] H. Imai, J. Fukutomi, A. Kimura, H. Fujiwara. Effect of reduced pressure on the polarization of ^{129}Xe in the production of hyperpolarized ^{129}Xe gas: Development of a simple continuous flow mode hyperpolarizing system working at pressures as low as 0.15 atm. *Concepts Magn. Reson., Part B* **33B**, 192–200 (2008).

[Imai 10] H. Imai, A. Kimura, S. Iguchi, Y. Hori, S. Masuda, H. Fujiwara. Noninvasive Detection of Pulmonary Tissue Destruction in a Mouse Model of Emphysema Using Hyperpolarized ^{129}Xe MRS Under Spontaneous Respiration. *Magn. Reson. Med.* **64**, 929–938 (2010).

[J. Wolber 99] A. S. K. Dzik-Jurasz M. O. Leach J. Wolber A. Cherubini, A. Bifone. Spin-lattice relaxation of laser-polarized xenon in human blood. *Proc. Natl. Acad. Sci. U.S.A.* **96**, 3664Ű3669 (1999).

[Jackson 91] J.I. Jackson, C.H. Meyer, D.G. Nishimura, A. Macovski. Selection of a convolution function for Fourier inversion using gridding. *IEEE Trans. Med. Imaging* **10**, 473–478 (1991).

[Jameson 73] C. J. Jameson, A. K. Jameson, S. M. Cohen. Temperature and density dependence of ^{129}Xe chemical shift in xenon gas. *J. Chem. Phys.* **59**, 4540–4546 (1973).

[Jameson 88] C. J. Jameson, A. K. Jameson, J. K. Hwang. Nuclear spin relaxation by intermolecular magnetic dipole coupling in the gas phase. ^{129}Xe in oxygen. *J. Chem. Phys.* **89**(7), 4074–4081 (1988).

[Jameson 02] C. J. Jameson, A. C. de Dios. Xe nuclear magnetic resonance line shapes in nanochannels. *J. Chem. Phys.* **116**, 3805–3821 (2002).

[Jeener 79] J. Jeener, B.H. Meier, P. Bachmann, R.R. Ernst. Investigation of exchange processes by two-dimensional NMR spectroscopy. *J. Chem. Phys.* **71**, 4546–4553 (1979).

[Jeffrey 94] K.R. Jeffrey, P.T. Callaghan, Y. Xia. The measurement of velocity profiles: An application of NMR microscopy. *Food Res. Int.* **27**, 199–201 (1994).

[Jezzard 96] P. Jezzard, S. Duewell, R. S. Balaban. MR relaxation times in human brain: measurement at 4T. *Radiology* **199**, 773–779 (1996).

[Kaiser 70] R. Kaiser. Coherent spectrometry with noise signals. *J. Magn. Reson.* **3**, 28–43 (1970).

[Kak 88] A.C. Kak, M. Slaney. Principles of Computerized Tomographic Imaging. New York, NY, IEEE Press (1988).

[Karichev 99] Z. R. Karichev, A. L. Muler, M.E. Vishnevsky. Spontaneous gas bubbling in microporous oxygenators. *Artif. Organs* **23**, 904–909 (1999).

[Kastler 50] A. Kastler. Quelques suggestions concernant la production optique et la détection optique d'une inégalité de population des niveaux de quantification spatiale des atomes. *J. Phys. Radium* **11**, 255–265 (1950).

[Klaus 04] S. Klaus. *Bluttraumatisierung bei der Passage zeitkonstanter und zeitvarianter Scherfelder*. Dissertation, RWTH Aachen University (2004).

[Knagge 04] K. Knagge, J. Prange, D. Raftery. A continuously recirculating optical pumping apparatus for high xenon polarization and surface NMR studies **397**, 11–16 (2004).

[Krug 09] Roland Krug, Christoph Stehling, Douglas A. C. Kelley, Sharmila Majumdar, Thomas M. Link. Imaging of the Musculoskeletal System In Vivo Using Ultra-high Field Magnetic Resonance at 7 T. *Invest. Radiol.* **44**, 613–618 (2009).

[Kwan 69] E. Kwan, A. Trevor. The Association of Xenon with Subcellular Components of Rat Cerebral Cortex. *Mol. Pharmacol.* **5**, 236–243 (1969).

[Ladefoged 67] J. Ladefoged, A. Andersen. Solubility of Xenon-133 at 37řC in Water, Saline, Olive Oil, Liquid Paraffin, Solutions of Albumin, and Blood. *Phys. Med. Biol.* **12**, 353–358 (1967).

[Landeghem 10] M. van Landeghem, A. Haber, J.-B. D'espinose De Lacaillerie, B. Blümich. Analysis of multisite 2D relaxation exchange NMR. *Concepts Magn. Reson., Part A* **36A** (2010).

[Lauterbur 73] P. C. Lauterbur. Image Formation by Induced Local Interactions: Examples Employing Nuclear Magnetic Resonance. *Nature* **242**, 190–191 (1973).

[Lee 08] H. Lee, Eric Sun, D. Ham, R. Weissleder. Chip-NMR biosensor for detection and molecular analysis of cells. *Nat. Med.* **14**, 869–874 (2008).

[Levitt 05] M. H. Levitt. Spin Dynamics: Basics of Nuclear Magnetic Resonance. John Wiley & Sons, Ltd, 3. edition (2005).

[Li 94] T. Q. Li, J. D. Seymour, R. L. Powell, K. L. McCarthy, L. Ödberg, M. J. McCarthy. Turbulent pipe flow studied by time-averaged NMR imaging: Measurements of velocity profile and turbulent intensity. *Magn. Reson. Imaging* **12**, 923 (1994).

[Ljunggren 83] S. Ljunggren. A simple graphical representation of fourier-based imaging methods. *J. Magn. Reson.* **54**, 338–343 (1983).

[Lynch 00] C. Lynch, J. Baum, R. Tenbrinck. Xenon Anesthesia. *Anesthesiology* **92**, 865–870 (2000).

[Mansfield 73] P. Mansfield, P. K. Grannell. NMR 'diffraction' in solids? *J. Phys. C* **6**, L422–L426 (1973).

[Marion 83] D. Marion, K. Wüthrich. Application of phase sensitive two-dimensional correlated spectroscopy (COSY) for measurements of ^{1}H-^{1}H spin-spin coupling constants in proteins. *Biochem. Biophys. Res. Commun.* **113**, 967–974 (1983).

[Marques 10] J. Marques, R. Gruetter, W. van der Zwaag. *In vivo* Structural Imaging of the Cerebellum, the Contribution of Ultra-High Fields. *Cerebellum*pp. 1–8 (2010).

[Martin 97] C. C. Martin, R. F. Williams, J.-H. Gao, L. D. H. Nickerson, J. Xiong, P. T. Fox. The pharmacokinetics of hyperpolarized xenon: Implications for cerebral MRI. *J. Magn. Reson. Imaging* **7**, 848–854 (1997).

[Matsuda 85] H. Matsuda, F. Nomura, S. Ohtake, M. Ohtani, M. Kaneko, Nishigaki, Y. Miyamoto, S. Nakano, H. Hirose, Y. Kawashima. Evaluation of a new siliconized polypropylene hollow fiber membrane lung for ECMO. *Trans. Am. Soc. Artif. Intern. Organs* **31**, 599–603 (1985).

[McDowell 08] A. McDowell, E. Fukushima. Ultracompact NMR: ^{1}H spectroscopy in a subkilogram magnet. *Appl. Magn. Reson.* **35**, 185–195 (2008).

[Melian-Flaman 09] Claudiu Melian-Flamand. *Advanced NMR Analysis of Polymers and Biomolecules*. Dissertation, RWTH Aachen University (2009).

[Meyns 05] B. Meyns, L. Vercaemst, E. Vandezande, H. Bollen, D. Vlasselaers. Plasma leakage of oxygenators in ECMO depends on the type of oxygenator and on patient variables. *Int. J. Artif. Organs* **28**, 30–34 (2005).

[Mühlbauer 07] F. Mühlbauer. *Polarimetrie an hyperpolarisiertem ^{129}Xenon*. Dissertation, University Mainz (2007).

[Miller 81] K. W. Miller, N. V. Reo, A. J. M. Schoot Uiterkamp, D. P. Stengle, T. R. Stengle, K. L. Williamson. Xenon NMR: Chemical Shifts of a General

Anesthetic in Common Solvents, Proteins, and Membranes. *Proc. Natl. Acad. Sci. U.S.A.* **78**, 4946–4949 (1981).

[Mockros 85] L. F. Mockros, R. Leonard. Compact cross-flow tubular oxygenators. *Trans. Am. Soc. Artif. Intern. Organs* **31**, 628–633 (1985).

[Moudrakovski 00] I. L. Moudrakovski, A. Nossov, S. Lang, S. R. Breeze, C. I. Ratcliffe, B. Simard, G. Santyr, J. A. Ripmeester. Continuous Flow NMR with Hyperpolarized Xenon for the Characterization of Materials and Processes. *Chem. Mater.* **12**, 1181–1183 (2000).

[Moudrakovski 01] I. L. Moudrakovski, S. R. Breeze, B. Simard, C. I. Ratcliffe, J. A. Ripmeester, T. Seideman, J. S. Tse, G. Santyr, I. Zuger. Coatings for optical pumping cells and short-term storage of hyperpolarized xenon. *J. Chem. Phys.* **114**, 4040–4042 (2001).

[Mueller 00] X. M. Mueller, B. Marty, H. T. Tevaearai, P. Tozzi, D. Jegger, L.K. von Segesser. A siliconized hollow fiber membrane oxygenator. *ASAIO J.* **46**, 38–41 (2000).

[Natterer 97] J. Natterer, J. Bargon. Parahydrogen Induced Polarization. *Prog. Nucl. Magn. Reson. Spectrosc.* **31**, 293–315 (1997).

[Navon 96] G. Navon, Y.-Q. Song, T. Room, S. Appelt, R. E. Taylor, A. Pines. Enhancement of Solution NMR and MRI with Laser-Polarized Xenon. *Science* **271**, 1848–1851 (1996).

[Nilgens 96] H. Nilgens, M. Thelen, J. Paff, P. Blümler, B. Blümich. Hadamard NMR imaging with slice selection. *Magn. Reson. Imaging* **14**, 857–861 (1996).

[NIST 07] NIST, National Institute of Standards and Technology (2007). `http://physics.nist.gov/cuu/Constants/index.html`.

[Niwa 04] M. Niwa, H. Kawakami, S. Nagaoka, T. Kanamori, K. Morisaku, T. Shinbo, T. Matsuda, K. Sakai, S. Kubota. Development of a novel polyimide hollow-fiber oxygenator. *Artif. Organs* **28**, 487–495 (2004).

[Nossov 03] A. Nossov, F. Guenneau, M.-A. Springuel-Huet, E. Haddad, V. Montouillout, B. Knott, F. Engelke, C. Fernandez, A. Gédéon. Continuous flow hyperpolarized ^{129}Xe-MAS NMR studies of microporous materials. *Phys. Chem. Chem. Phys.* **5**, 4479–4483 (2003).

[Nyquist 28] H. Nyquist. Certain topics in telegraph transmission theory. *Am. Inst. Electr. Eng. Trans.* **47**, 617–644 (1928).

[Oros 04] A. Oros, N. J. Shah. Hyperpolarized xenon in NMR and MRI **49**, R105–R153 (2004).

[Paff 91] J. Paff, B. Blümich. Observation of a Spin Echo with Continuous White Noise Excitation. *Phys. Rev. A* **43**, 3640–3644 (1991).

[Paff 92] J. Paff, B. Blümich, R. Kaiser. Nonlinear incoherent spectroscopy: NOISY. *Adv. Magn. Opt. Reson.* **17**, 1–46 (1992).

[Paul 00] R. Paul. *Untersuchungen zur Blutschädigung durch laminare Strömung im Couette-System*. Dissertation, RWTH Aachen University (2000).

[Paul 03] R. Paul, J. Apel, S. Klaus, F. Schugner, P. Schwindke, H. Reul. Shear stress related blood damage in laminar couette flow. *Artif. Organs* **27**, 517–529 (2003).

[Pauling 36] L. Pauling, C. D. Coryell. The magnetic properties and structure of hemoglobin, oxyhemoglobin and carbonmonoxyhemoglobin. *Proc. Natl. Acad. Sci. U.S.A.* **22**, 159–163 (1936).

[Peled 96] S. Peled, F. A. Jolesz, C. H. Tseng, L. Nascimben, M. S. Albert, R. L. Walsworth. Determinants of tissue delivery for ^{129}Xe magnetic resonance in humans. *Magn. Reson. Med.* **36**, 340–344 (1996).

[Pelster 88] B. Pelster, H. Kobayashi, P. Scheid. Solubility of nitrogen and argon in eel whole blood and its relationship to pH. *J. Exp. Biol.* **135**, 243–252 (1988).

[Perrin 90] C.L. Perrin, T.J. Dwyer. Application of two-dimensional NMR to kinetics of chemical exchange. *Chem. Rev.* **90**, 935–967 (1990).

[Perutz 70] M. F. Perutz. Stereochemistry of cooperative effects in haemoglobin. *Nature* **228**, 726–739 (1970).

[Pfeffer 95] M. Pfeffer, O. Lutz. Observation of Diffusion in Xenon Gas by NMR **113**, 108–113 (1995).

[Philipp 02] A. Philipp. Narkosegastransfer via Membranoxygenator. *Kardiotechnik* **1**, 3–6 (2002).

[Pietraß 95] T. Pietraß, H. C. Gaede. Optically Polarized ^{129}Xe in NMR Spectroscopy. *Adv. Mater.* **7**, 826–838 (1995).

[Playavin 83] Y. A. Playavin, E. Y. Blum. Magnetic parameters of blood cells and high-gradient paramagnetic and diamagnetic phoresis. *Magnetohydrodynamics* **14**, 349–359 (1983).

[Pries 92] A. R. Pries, D. Neuhaus, P. Gaehtgens. Blood viscosity in tube flow: dependence on diameter and hematocrit. *Am. J. Physiol. - Heart* **263**, H1770–H1778 (1992).

[Proctor 50] W. G. Proctor, F. C. Yu. The Dependence of a Nuclear Magnetic Resonance Frequency upon Chemical Compound. *Phys. Rev.* **77**, 717–717 (1950).

[Purcell 46] E. M. Purcell, H. C. Torrey, R. V. Pound. Resonance Absorption by Nuclear Magnetic Moments in a Solid. *Phys. Rev.* **69**, 37–38 (1946).

[Quemada 78] D. Quemada. Rheology of concentarted disperse systems: II. A model for non-Newtonian shear viscosity in steady flow & III. Genearl features of the proposed non-Neatonian model: Comparison with experimental data. *Rheol. Acta* **17**, 632–653 (1978).

[Radon 17] J. Radon. Über die Bestimmung von Funktionen durch ihre Integralwerte längs gewisser Mannigfaltigkeiten. *Berichte Sächsischer Akademie der Wissenschaften zu Leipzig, Math.-Phys. Klasse* **69**, 262–267 (1917).

[Raftery 91] D. Raftery, H. Long, T. Meersmann, P. J. Grandinetti, L. Reven, A. Pines. High-field NMR of adsorbed xenon polarized by laser pumping. *Phys. Rev. Lett.* **66**, 584–587 (1991).

[Rich 02] J. R. Rich, T. R. Gentile, T. B. Smith, A. K. Thompson, G. L. Jones. Spin exchange optical pumping at pressures near 1 bar for neutron spin filters. *Appl. Phys. Lett.* **80**, 2210–2212 (2002).

[Römpp 99] H. Römpp, J. Falbe, M. Regitz von Thieme. Lexikon Chemie. Georg Thieme Verlag, 10. edition (1999).

[Robitaille 98] P. M. Robitaille, A. M. Abduljalil, A. Kangarlu, X. Zhang X, Y. Yu, R. Burgess, S. Bair, P. Noa, L. Yang, H. Zhu, B. Palmer, Z., Jiang, D. M. Chakeres, D. Spigos. Human magnetic resonance imaging at 8 T. *NMR Biomed.* **11**, 263–265 (1998).

[Romalis 97] M. V. Romalis, E. Miron, G. D. Cates. Pressure broadening of Rb D1 and D2 lines by ^{3}He, ^{4}He, N_2, and Xe: Line cores and near wings. *Phys. Rev. A* **56**, 4569–4578 (1997).

[Ruppert 00] K. Ruppert, J. R. Brookeman, K. D. Hagspiel, J. P. Mugler III. Probing Lung Physiology With Xenon Polarization Transfer Contrast (XTC). *Magn. Reson. Med.* **44**, 349–357 (2000).

[Ruppert 07] K. Ruppert, J. F. Mata, H.-T. J. Wang, W. A. Tobias, G. D. Cates, J. R. Brookeman, K. D. Hagspiel, J. P. Mugler III. XTC MRI: Sensitivity Improvement Through Parameter Optimization. *Magn. Reson. Med.* **57**, 1099–1109 (2007).

[Ruset 06] I. C. Ruset, S. Ketel, F. W. Hersman. Optical Pumping System Design for Large Production of Hyperpolarized ^{129}Xe. *Phys. Rev. Lett.* **96**, 0530021–0530024 (2006).

[Schearer 65] L. D. Schearer, G. K. Walters. Nuclear Spin-Lattice Relaxation in the Presence of Magnetic-Field Gradients. *Phys. Rev.* **139**, 1398–1402 (1965).

[Schmidt 95] R. Schmidt, G. Thews. Physiologie des Menschen. Springer Verlag, Berlin, Heidelberg, New York, London, Paris, Tokyo, 26. edition (1995).

[Schmiedeskamp 06a] J. Schmiedeskamp, H.-J. Elmers, W. Heil, E. W. Otten, Yu. Sobolev, W. Kilian, H. Rinneberg, T. Sander-Thömmes, F. Seifert, J. Zimmer. Relaxation of spin polarized ^{3}He by ferromagnetic contaminants. *Eur. Phys. J. D* **38**, 445–454 (2006).

[Schmiedeskamp 06b] J. Schmiedeskamp, W. Heil, E. W. Otten, R. K. Kremer, A. Simon, J. Zimmer. Paramagnetic relaxation of spin polarized ^{3}He at bare glass surfaces. *Eur. Phys. J. D* **38**, 427–438 (2006).

[Schoenborn 65] B. P. Schoenborn. Binding of xenon to horse haemoglobin. *Nature* **208**, 760–762 (1965).

[Schröder 06] L. Schröder, T. J. Lowery, C. Hilty, D. E. Wemmer, A. Pines. Molecular Imaging Using a Targeted Magnetic Resonance Hyperpolarized Biosensor. *Science* **314**, 446–449 (2006).

[Schrobilgen 78] G. J. Schrobilgen. NMR and the Periodic Table. Academic Press, 1. edition (1978).

[Shah 00] N. J. Shah, T. Ünlü, H.-P. Wegener, H. Halling, K. Zilles, S. Appelt. Measurement of rubidium and xenon absolute polarization at high temperatures as a means of improved production of hyperpolarized ^{129}Xe. *NMR Biomed.* **13**, 214–219 (2000).

[Sharan 01] M. Sharan, A.S. Popel. A two-phase model for blood in narrow tubes with increased effective viscosity near the wall. *Biorheology* **38**, 415–428 (2001).

[Siggaard-Ande 88] O. Siggaard-Andersen, P. D. Wimberley, I. H Gøthgen, N. Fogh-Andersen, J. P. Rasmussen. Variability of the temperature coefficients for pH, pCO_2, and pO_2 in blood. *Scand. J. Clin. Lab. Invest.* **48**, 85–88 (1988).

[Sillerud 06] Laurel O. Sillerud, Andrew F. McDowell, Natalie L. Adolphi, Rita E. Serda, David P. Adams, Michael J. Vasile, Todd M. Alam. ^{1}H NMR Detection of superparamagnetic nanoparticles at 1 T using a microcoil and novel tuning circuit. *J. Magn. Reson.* **181**, 181–190 (2006).

[Simonutti 06] R. Simonutti, S. Bracco, A. Comotti, M. Mauri, P. Sozzani. Continuous Flow Hyperpolarized ^{129}Xe NMR for Studying Porous Polymers and Blends. *Chem. Mater.* **18**, 4651–4657 (2006).

[Skalak 87] R. Skalak, S. Chien. Handbook of Bioengineering. Graw-Hill, New York (1987).

[Spiess 71] H. W. Spiess, D. Schweitzer, U. Haeberlen, K. H. Hausser. Spin-rotation interaction and anisotropic chemical shift in $^{13}CS_2$. *J. Magn. Reson.* **5**, 101–108 (1971).

[Stanisz 98] G. J. Stanisz, J. G. Li, G. A. Wright, R. M. Henkelman. Water dynamics in human blood via combined measurements of T_2 relaxation and diffusion in the presence of gadolinium. *Magn. Reson. Med.* **39**, 223–233 (1998).

[Stengle 81] T. R. Stengle, N. V. Reo, K. L. Williamson. Nuclear Magnetic Resonance Solvent Shifts of Xenon. A Test of the Reaction Field Model. *J. Phys. C* **85**, 3772–3775 (1981).

[Swanson 97] S. D. Swanson, M. S. Rosen, B. W. Agranoff, K. P. Coulter, R. C. Welsh, T. E. Chupp. Brain MRI with Laser-Polarized ^{129}Xe. *Magn. Reson. Med.* **38**, 695–698 (1997).

[Tilton 82] R. F. Tilton, I. D. Kuntz. Nuclear magnetic resonance studies of Xe-129 with myoglobin and hemoglobin. *Biochemistry* **21**, 6850–6857 (1982).

[Tilton 86] R.F. Tilton, U. C. Singh, S. J. Weiner, M. L. Connolly, I. D. Kuntz, P. A. Kollman, N. Max, D. A. Case. Computational studies of the interaction of myoglobin and xenon. *J. Mol. Biol.* **192**, 443–456 (1986).

[Tseng 97] C.H. Tseng, S. Peled, L. Nascimben, E. Oteiza, R.L. Walsworth, F.A. Jolesz. NMR of Laser-Polarized ^{129}Xe in Blood Foam. *J. Magn. Reson.* **126**, 79 – 86 (1997).

[Tweeddale 73] P. M. Tweeddale. Blood oxygen affinities of the adult and foetal large white pig. *Respir. Physiol.* **19**, 145–152 (1973).

[Twieg 83] D. B. Twieg. The k-trajectory formulation of the NMR imaging process with applications in analysis and synthesis of imaging methods. *Med. Phys.* **10**, 610–621 (1983).

[Utiu 12] L. Utiu. *Functional NMR and MRI for Analysis of Materials (preliminary titel).* Dissertation, RWTH Aachen University (2012).

[Vaughan 01] J. T. Vaughan, M. Garwood, C. M. Collins, W. Liu, L. DelaBarre, G. Adriany, P. Andersen, H. Merkle, R. Goebel, M. B. Smith, K. Ugurbil. 7 T vs. 4 T: RF power, homogeneity, and signal-to-noise comparison in head images. *Magn. Reson. Med.* **46**, 24–30 (2001).

[Wagshul 89] M. E. Wagshul, T. E. Chupp. Optical pumping of high-density Rb with a broadband dye laser and GaALAs diode laser arrays: Application to ^{3}He polarization. *Phys. Rev. A* **40**, 4447–4454 (1989).

[Wagshul 94] M. E. Wagshul, T. E. Chupp. Laser optical pumping of high-density Rb in polarized ^{3}He targets. *Phys. Rev. A* **49**, 3854–3869 (1994).

[Wakayama 08] T. Wakayama, M. Kitamoto, T. Ueyama, H. Imai, M. Narazaki, A. Kimura, H. Fujiwara. Hyperpolarized ^{129}Xe MRI of the Mouse Lung at a Low Xenon Concentration Using a Continuous Flow-Type Hyperpolarizing System. *J. Magn. Reson. Imaging* **27**, 777–784 (2008).

[Walker 97] T. G. Walker, W. Happer. Spin Exchange optical pumping of noble-gas nuclei. *Rev. Mod. Phys.* **69**, 629–642 (1997).

[Wansapura 99] J. P. Wansapura, S. K. Holland, R. S. Dunn, W. S Ball. NMR relaxation times in the human brain at 3.0 Tesla. *J. Magn. Reson. Imaging* **9**, 531–538 (1999).

[Whitmore 68] R.L. Whitmore. Rheology of the circulation. Oxford: Pergamon Press (1968).

[Wickramasingh 02] S. R. Wickramasinghe, B. Han. Mass and momentum transfer in commercial blood oxygenators. *Desalination* **148**, 227–233 (2002).

[Wiesenack 02] C. Wiesenack, G. Wiesner, C. Keyl, Gruber M, A. Philipp, M. Ritzka, C. Prasser, K. Taeger. In Vivo Uptake and Elimination of Isoflurane by Different Membrane Oxygenators during Cardiopulmonary Bypass. *Anesthesiology* **97**, 133–138 (2002).

[Willford 86] D. C. Willford, E. P. Hill. Modest Effect of Temperatur on the Porcine Oxygen Dissociation Curve. *Respir. Physiol.* **64**, 113–123 (1986).

[Wolber 00a] J. Wolber, A. Cherubini, M. O. Leach, A. Bifone. Hyperpolarized ^{129}Xe NMR as a probe for blood oxygenation. *Magn. Reson. Med.* **43**, 491–496 (2000).

[Wolber 00b] J. Wolber, A. Cherubini, M. O. Leach, A. Bifone. On the oxygenation-dependent ^{129}Xe T_1 in blood. *NMR Biomed.* **13**, 234–237 (2000).

[Wüthrich 03] K. Wüthrich. NMR Studies of Structure and Function of Biological Macromolecules (Nobel Lecture). *Angew. Chem.* **42**, 3340–3363 (2003).

[Yamaguchi 87] K. Yamaguchi, J. Glahn, P. Scheid, J. Piiper. Oxygen transfer conductance of human red blood cells at varied pH and temperature. *Respir. Physiol.* **67**, 209–223 (1987).

[Yamaguchi 93] K. Yamaguchi, M. Mori, A. Kawai, K. Asano, T. Takasugi, A. Umeda, T. Kawashiro, T. Yokoyama. Effects of pH and SO2 on solubility coefficients of inert gases in human whole blood. *J. Appl. Physiol.* **74**, 643–649 (1993).

[Ye 95] F. Q. Ye, P. S. Allen. Relaxation enhancement of the transverse magnetization of water protons in paramagnetic suspensions of red-blood-cells. *Magn. Reson. Med.* **34**, 713–720 (1995).

[Yeleswarapu 98] K. K. Yeleswarapu, M. V. Kameneva, K. R. Rajagopal, J. F. Antaki. The flow of blood in tubes: theory and experiment. *Mech. Res. Commun.* **25**, 257–262 (1998).

[Yesinowski 95] J.P. Yesinowski, M.L. Buess, A.N. Garroway, M. Ziegenweid, A. Pines. Detection of ^{14}N and ^{35}Cl in cocaine base and hydrochloride using NQR, NMR, and SQUID techniques. *Anal. Chem.* **67**, 2256–2263 (1995).

[Ziessow 74] D. Ziessow, B. Blümich. Hadamard-NMR-Spektroskopie. *Ber. Bunsenges. Phys. Chem.* **78**, 1168–1179 (1974).

[Zänker 07] P. P. Zänker. *NMR Spectroscopy and Imaging of Hyperpolarized Gases: Fundamental Aspects and Applications.* Dissertation, University Mainz (2007).

[Zook 02] A. L. Zook, B. B. Adhyaru, C. R. Bowers. High capacity production of >65% spin polarized xenon-129 for NMR spectroscopy and imaging. *J. Magn. Reson.* **159**, 175–182 (2002).

Acknowledgments

This work would not have been possible without the great help by many of my co-workers, friends, and my family. Therefore, I would like to thank ...

... Prof. Bernhard Blümich for the opportunity to work in his group and to profit from the great expertise and scientific environment. In particular, I want to thank him for many helpful discussions as well as for the great freedom he gave me to independently choose the focus of my research and the always optimistic support of my work.

... Prof. Thomas Schmitz-Rode, who as our partner in the xenon project and referee of my thesis took a lot of time to plan and conduct our project and to correct and improve my work. Especially, I would like to thank him for the close cooperation and the possibility of working together in a very uncomplicated and straightforward way.

... Prof. Stephan Appelt, who as the expert in xenon hyperpolarization was always available for detailed and substantial discussions and thus helped me a lot in conducting my experiments and interpreting my results.

... Dr. Federico Casanova and Dr. Marcus Greferath for so many discussions on the Frank project, their patience, and their enthusiam, which helped a lot and motivated me many times.

... Kathrin Hamilton for the good cooperation and her great commitment for the xenon project. I also want to thank Prof. Ulrich Steinseifer and everyone else from the Helmholtz Institute, who worked on and supported this project.

... Dr. Markus Küppers for his support ranging from solving problems with the NMR spectrometers to fighting bureaucracy.

... the entire MC workgroup for their cooperation and the many cheerful hours espe-

cially on conferences. Good luck to everyone!

... my friends for sharing many wonderful moments outside the world of science, which helped to bring back power and to free my mind.

The greatest thanks go to my family. Without the support of my parents none of this would have been possible. And my husband Georg - there simply are no words to express everything here I would like to thank him for.

Thanks!